WILEY-VCH

Phase Transformations in Materials

Edited by Gernot Kostorz (2001)

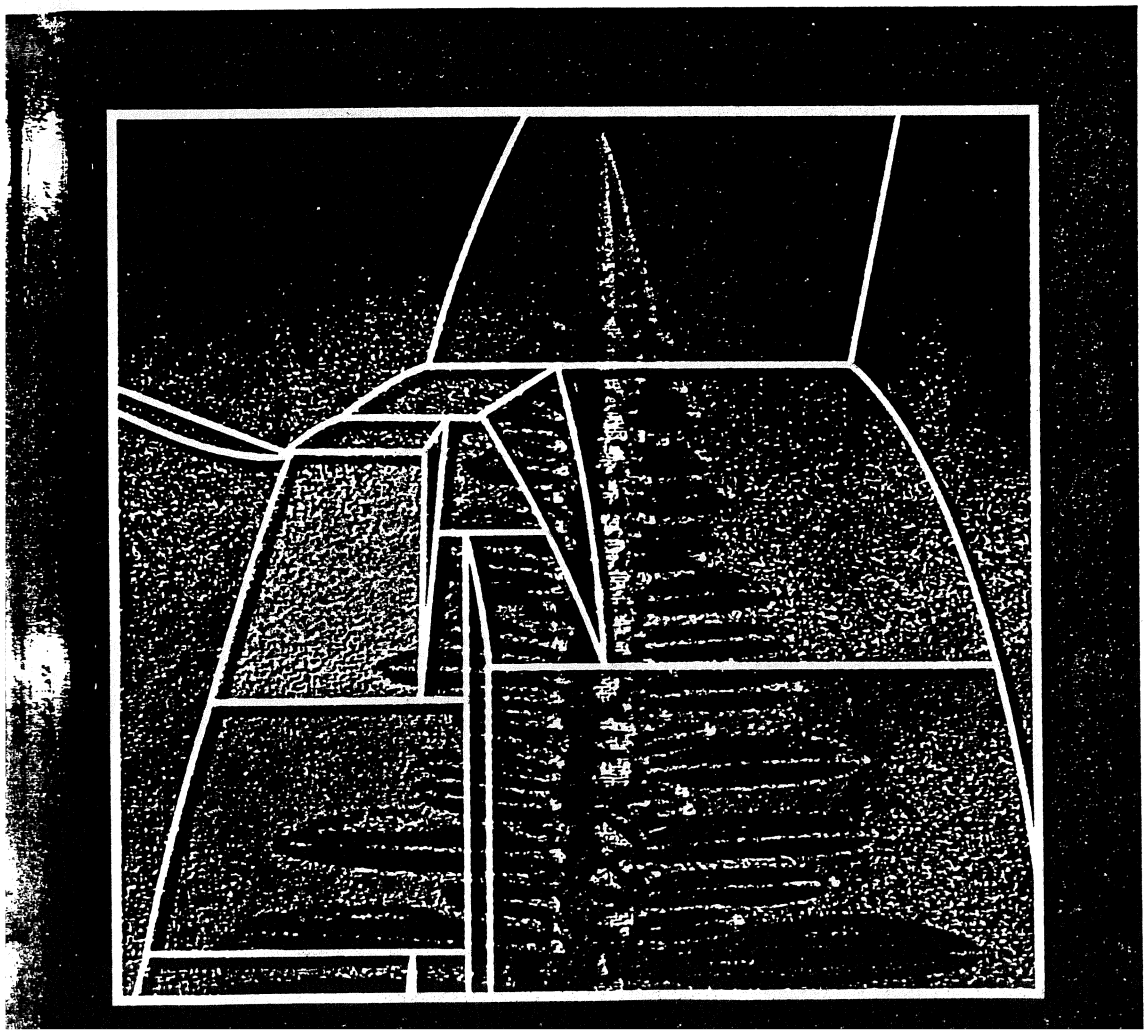

Related titles from WILEY-VCH

Eric Lifshin (Ed.)
X-ray Characterization of Materials
ISBN 3-527-29657-3

Dierk Raabe
Computational Materials Science
ISBN 3-527-29541-0

1 Thermodynamics and Phase Diagrams of Materials

Arthur D. Pelton

Centre de Recherche en Calcul Thermochimique, École Polytechnique,
Montréal, Québec, Canada

List of Symbols and Abbreviations

Symbol	Designation
a_i	activity of component i
C	number of components
c_p	molar heat capacity
E	electrical potential of a galvanic cell
F	degrees of freedom/variance
G	Gibbs energy in J
g	molar Gibbs energy in J/mol
g_i	partial molar Gibbs energy of i
G_i^0	standard Gibbs energy of i
g_i^0	standard molar Gibbs energy of i
Δg_i	relative partial Gibbs energy i
g^E	excess molar Gibbs energy
g_i^E	excess partial Gibbs energy of i
ΔG	Gibbs energy change
ΔG^0	standard Gibbs energy change
Δg_m	molar Gibbs energy of mixing
Δg_f^0	standard molar Gibbs energy of fusion
Δg_v^0	standard molar Gibbs energy of vaporization
H	enthalpy in J
h	molar enthalpy in J/mol
h_i	partial enthalpy of i
H_i^0	standard enthalpy of i
h_i^0	standard molar enthalpy of i
Δh_i	relative partial enthalpy of i
h^E	excess molar enthalpy
h_i^E	excess partial enthalpy of i
ΔH	enthalpy change
ΔH^0	standard enthalpy change
Δh_m	molar enthalpy of mixing
Δh_f^0	standard molar enthalpy of fusion
Δh_v^0	standard molar enthalpy of vaporization
K	equilibrium constant
k_B	Boltzmann constant
n	number of moles
n_i	number of moles of constituent i
N_i	number of particles of i
N^0	Avogadro's number
p_i	partial pressure of i
P	total pressure
P	number of phases
q_i	general extensive variable

R	gas constant
S	entropy in J/K
s	molar entropy in J/mol K
s_i	partial entropy of i
S_i^0	standard entropy of i
s_i^0	standard molar entropy of i
Δs_i^0	relative partial entropy of i
s^E	excess molar entropy
s_i^E	excess partial entropy of i
ΔS	entropy change
ΔS^0	standard entropy change
Δs_m	molar entropy of mixing
Δs_f^0	standard molar entropy of fusion
Δs_v^0	standard molar entropy of vaporization
T	temperature
T_f	temperature of fusion
T_c	critical temperature
T_E	eutectic temperature
U	internal energy
v_i	molar volume of i
v_i^0	standard molar volume of i
X_i	mole fraction of i
Z	coordination number
γ_i	activity coefficient of i
ε	bond energy
η	empirical entropy parameter
μ_i	chemical potential of i
ν	number of moles of "foreign" particles contributed by a mole of solute
ξ	molar metal ratio
σ	vibrational bond entropy
ϕ_i	generalized thermodynamic potential
ω	empirical enthalpy parameter
b.c.c.	body-centered cubic
f.c.c.	face-centered cubic
h.c.p.	hexagonal close-packed

1.1 Introduction

An understanding of thermodynamics and phase diagrams is fundamental and essential to the study of materials science. A knowledge of the equilibrium state under a given set of conditions is the starting point in the description of any phenomenon or process.

The theme of this chapter is the relationship between phase diagrams and thermodynamics. A phase diagram is a graphical representation of the values of thermodynamic variables when equilibrium is established among the phases of a system. Materials scientists are used to thinking of phase diagrams as plots of temperature versus composition. However, many other variables such as total pressure and partial pressures may be plotted on phase diagrams. In Sec. 1.3, for example, predominance diagrams will be discussed, and in Sec. 1.8 chemical potential–composition phase diagrams will be presented. General rules regarding phase diagram geometry are given in Sec. 1.9.

In recent years, a quantitative coupling of thermodynamics and phase diagrams has become possible. With the use of computers, simultaneous optimizations of thermodynamic and phase equilibrium data can be applied to the critical evaluation of binary and ternary systems as shown in Sec. 1.6. This approach often enables good estimations to be made of the thermodynamic properties and phase diagrams of multicomponent systems as discussed in Sec. 1.11. These estimates are based on structural models of solutions. Various models such as the regular solution model, the sublattice model, and models for interstitial solutions, polymeric solutions, solutions of defects, ordered solutions, etc. are discussed in Secs. 1.5 and 1.10.

The equilibrium diagram is always calculated by minimization of the Gibbs energy. General computer programs are available for the minimization of the Gibbs energy in systems of any number of phases, components and species as outlined in Sec. 1.12. When coupled to extensive databases of the thermodynamic properties of compounds and multicomponent solutions, these provide a powerful tool in the study of materials science.

1.1.1 Notation

Extensive thermodynamic properties are represented by upper case symbols. For example, G = Gibbs energy in J. Molar properties are represented by lower case symbols. For example, $g = G/n$ = molar Gibbs energy in J/mol where n is the total number of moles in the system.

1.2 Gibbs Energy and Equilibrium

1.2.1 Gibbs Energy

The Gibbs energy of a system is defined in terms of its enthalpy, H, entropy, S, and temperature, T:

$$G = H - TS \tag{1-1}$$

A system at constant temperature and pressure will approach an equilibrium state that minimizes G.

As an example, consider the question of whether silica fibers in an aluminum matrix at 500 °C will react to form mullite, $Al_6Si_2O_{13}$

$$\frac{13}{2}SiO_2 + 6Al = \frac{9}{2}Si + Al_6Si_2O_{13} \tag{1-2}$$

If the reaction proceeds with the formation of dn moles of mullite then, from the stoichiometry of the reaction, $dn_{Si} = (9/2)\,dn$, $dn_{Al} = -6\,dn$, and $dn_{SiO_2} = -13/2\,dn$. Since the four substances are essentially immiscible at 500 °C, we need consider only the

standard molar Gibbs energies, G_i^0. The Gibbs energy of the system then varies as:

$$dG/dn = g^0_{Al_6Si_2O_{13}} + \frac{9}{2} g^0_{Si} - \frac{13}{2} g^0_{SiO_2} - 6\, g^0_{Al} = \Delta G^0 = -830\ \text{kJ} \qquad (1\text{-}3)$$

where ΔG^0 is the standard Gibbs energy change of reaction, Eq. (1-2), at 500 °C.

Since $\Delta G^0 < 0$, the formation of mullite entails a decrease in G. Hence, the reaction will proceed spontaneously so as to minimize G.

1.2.2 Chemical Equilibrium

The partial molar Gibbs energy of an ideal gas is given by:

$$g_i = g_i^0 + RT \ln p_i \qquad (1\text{-}4)$$

where g_i^0 is the standard molar Gibbs energy (at 1 bar), p_i is the partial pressure in bar, and R is the gas constant. The second term in Eq. (1-4) is entropic. As a gas expands at constant T, its entropy increases.

Consider a gaseous mixture of H_2, S_2 and H_2S with partial pressures p_{H_2}, p_{S_2} and p_{H_2S}. The gases can react according to

$$2\,H_2 + S_2 = 2\,H_2S \qquad (1\text{-}5)$$

If the reaction, Eq. (1-5), proceeds to the right with the formation of $2\,dn$ moles of H_2S, then the Gibbs energy of the system varies as:

$$\begin{aligned} dG/dn &= 2\,g_{H_2S} - 2\,g_{H_2} - g_{S_2} \\ &= (2\,g^0_{H_2S} - 2\,g^0_{H_2} - g^0_{S_2}) \\ &\quad + RT\,(2 \ln p_{H_2S} - 2 \ln p_{H_2} - \ln p_{S_2}) \\ &= \Delta G^0 + RT \ln (p^2_{H_2S}\, p^{-2}_{H_2}\, p^{-1}_{S_2}) \\ &= \Delta G \end{aligned} \qquad (1\text{-}6)$$

ΔG, which is the Gibbs energy change of the reaction, Eq. (1-5), is thus a function of the partial pressures. If $\Delta G < 0$, then the reaction will proceed to the right so as to minimize G. In a closed system, as the reaction continues with the production of H_2S, p_{H_2S} will increase while p_{H_2} and p_{S_2} will decrease. As a result, ΔG will become progressively less negative. Eventually an equilibrium state will be reached when $dG/dn = \Delta G = 0$.

For the equilibrium state, therefore:

$$\begin{aligned} \Delta G^0 &= -RT \ln K \\ &= -RT \ln (p^2_{H_2S}\, p^{-2}_{H_2}\, p^{-1}_{S_2})_{\text{equilibrium}} \end{aligned} \qquad (1\text{-}7)$$

where K, the "equilibrium constant" of the reaction, is the one unique value of the ratio $(p^2_{H_2S}\, p^{-2}_{H_2}\, p^{-1}_{S_2})$ for which the system will be in equilibrium at the temperature T.

If the initial partial pressures are such that $\Delta G > 0$, then the reaction, Eq. (1-5), will proceed to the left in order to minimize G until the equilibrium condition of Eq. (1-7) is attained.

As a further example, we consider the possible precipitation of graphite from a gaseous mixture of CO and CO_2. The reaction is:

$$2\,CO = C + CO_2 \qquad (1\text{-}8)$$

Proceeding as above, we can write:

$$\begin{aligned} dG/dn &= g_C + g_{CO_2} - 2\,g_{CO} \\ &= (g^0_C + g^0_{CO_2} - 2\,g^0_{CO}) + RT \ln (p_{CO_2}/p^2_{CO}) \\ &= \Delta G^0 + RT \ln (p_{CO_2}/p^2_{CO}) \\ &= \Delta G = -RT \ln K + RT \ln (p_{CO_2}/p^2_{CO}) \end{aligned} \qquad (1\text{-}9)$$

If (p_{CO_2}/p^2_{CO}) is less than the equilibrium constant K, then precipitation of graphite will occur in order to decrease G.

Real situations are, of course, generally more complex. To treat the deposition of solid Si from a vapour of SiI_4, for example, we must consider the formation of gaseous I_2, I and SiI_2 so that three reaction equations must be written:

$$SiI_4(g) = Si(sol) + 2\,I_2(g) \qquad (1\text{-}10)$$

$$SiI_4(g) = SiI_2(g) + I_2(g) \qquad (1\text{-}11)$$

$$I_2(g) = 2\,I(g) \qquad (1\text{-}12)$$

The equilibrium state, however, is still that which minimizes the total Gibbs energy of the system. This is equivalent to satisfying simultaneously the equilibrium constants of the reactions, Eqs. (1-10) to (1-12), as will be shown in Section 1.12 where this example is discussed further.

1.3 Predominance Diagrams

1.3.1 Calculation of Predominance Diagrams

Predominance diagrams are a particularly simple type of phase diagram which have many applications in the fields of hot corrosion, chemical vapor deposition, etc. Furthermore, their construction clearly illustrates the principles of Gibbs energy minimization and the Gibbs Phase Rule.

A predominance diagram for the Cu–S–O system at 1000 K is shown in Fig. 1-1. The axes are the logarithms of the partial pressures of SO_2 and O_2 in the gas phase. The diagram is divided into areas or domains of stability of the various solid compounds of Cu, S and O. For example, at point Z, where $p_{SO_2} = 10^{-2}$ and $p_{O_2} = 10^{-7}$ bar, the stable phase is Cu_2O. The conditions for coexistence of two and three solid phases are indicated respectively by the lines and triple points on the diagram.

For example, along the univariant line (phase boundary) separating the Cu_2O and $CuSO_4$ domains the equilibrium constant $K = p_{SO_2}^{-2}\, p_{O_2}^{-3/2}$ of the following reaction is satisfied:

$$Cu_2O + 2\,SO_2 + \tfrac{3}{2}O_2 = 2\,CuSO_4 \qquad (1\text{-}13)$$

Hence, along this line:

$$\log K = -2 \log p_{SO_2} - \tfrac{3}{2} \log p_{O_2} = \text{constant} \qquad (1\text{-}14)$$

This boundary is thus a straight line with a slope of $(-3/2)/2 = -3/4$.

In constructing predominance diagrams, we define a "base element", in this case Cu, which must be present in all the condensed phases. Let us further assume that there is no mutual solubility among the condensed phases.

Following the procedure of Bale et al. (1986), we formulate a reaction for the for-

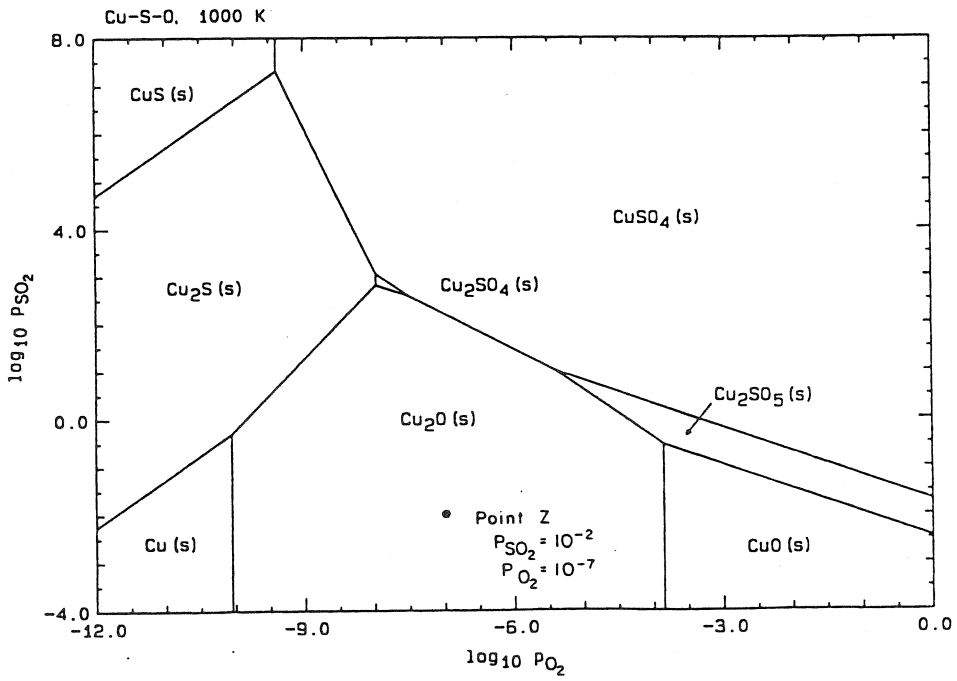

Figure 1-1. Predominance diagram. log p_{SO_2} versus log p_{O_2} (bar) at 1000 K for the Cu–S–O system (Bale et al., 1986).

mation of each solid phase, always from one mole of the base element Cu, and involving the gaseous species whose pressures are used as the axes (SO_2 and O_2 in this example):

$$Cu + \tfrac{1}{2}O_2 = CuO$$
$$\Delta G = \Delta G^0 + RT \ln p_{O_2}^{-1/2} \quad (1\text{-}15)$$

$$Cu + \tfrac{1}{4}O_2 = \tfrac{1}{2}Cu_2O$$
$$\Delta G = \Delta G^0 + RT \ln p_{O_2}^{-1/4} \quad (1\text{-}16)$$

$$Cu + SO_2 = CuS + O_2$$
$$\Delta G = \Delta G^0 + RT \ln (p_{O_2}\, p_{SO_2}^{-1}) \quad (1\text{-}17)$$

$$Cu + SO_2 + O_2 = CuSO_4$$
$$\Delta G = \Delta G^0 + RT \ln (p_{SO_2}^{-1}\, p_{O_2}^{-1}) \quad (1\text{-}18)$$

and similarly for the formation of Cu_2S, Cu_2SO_4 and Cu_2SO_5.

The values of ΔG^0 are obtained from tables of thermodynamic properties. For any given values of p_{SO_2} and p_{O_2}, ΔG for each formation reaction can then be calculated. The stable compound is simply the one with the most negative ΔG. If all the ΔG values are positive, then pure Cu is the stable compound.

By reformulating Eqs. (1-15) to (1-18) in terms of, for example, S_2 and O_2 rather than SO_2 and O_2, a predominance diagram with $\ln p_{S_2}$ and $\ln p_{O_2}$ as axes can be constructed. Logarithms of ratios or products of partial pressures can also be used as axes.

1.3.2 Ellingham Diagrams as Predominance Diagrams

Rather than keeping the temperature constant, we can use it as an axis. Figure 1-2 shows a diagram for the Fe–S–O system in which $RT \ln p_{O_2}$ is plotted versus T at constant $p_{SO_2} = 1$ bar. The diagram is of the same topological type as Fig. 1-1.

A similar phase diagram of $RT \ln p_{O_2}$ versus T for the Cu–O system is shown in Fig. 1-3. For the formation reaction:

$$4\,Cu + O_2 = 2\,Cu_2O \quad (1\text{-}19)$$

we can write:

$$\Delta G^0 = -RT \ln K = RT \ln (p_{O_2})_{\text{equilibrium}} = \Delta H^0 - T\Delta S^0 \quad (1\text{-}20)$$

The diagonal line in Fig. 1-3 is thus a plot of the standard Gibbs energy of formation of Cu_2O versus T. The temperatures indicated by the symbol M and [M] are the melting points of Cu and Cu_2O respectively. This line is thus simply a line taken from the well-known *Ellingham Diagram* or ΔG^0 vs. T diagram for the formation of oxides. However, by drawing vertical lines at the melting points of Cu and Cu_2O as shown in Fig. 1-3, we convert the plot to a true phase diagram. Stability domains for Cu(sol), Cu(l), Cu_2O(sol), and Cu_2O(l) are shown as functions of T and of imposed p_{O_2}. The lines and triple points indicate

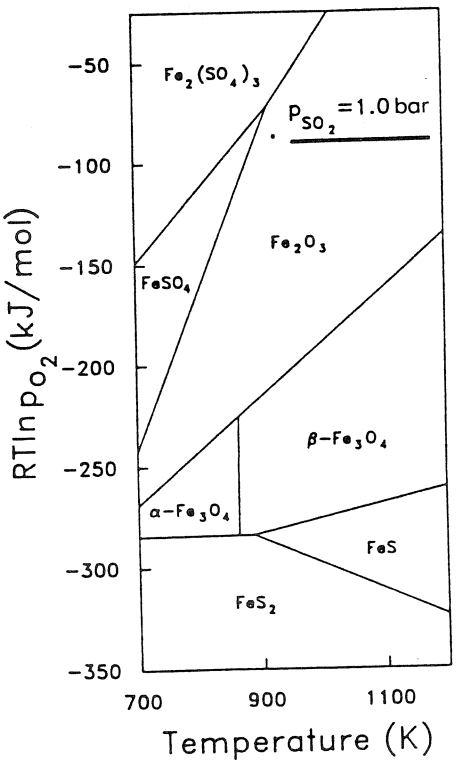

Figure 1-2. Predominance diagram. $RT \ln p_{O_2}$ versus T at $p_{SO_2} = 1.0$ bar for the Fe–S–O system.

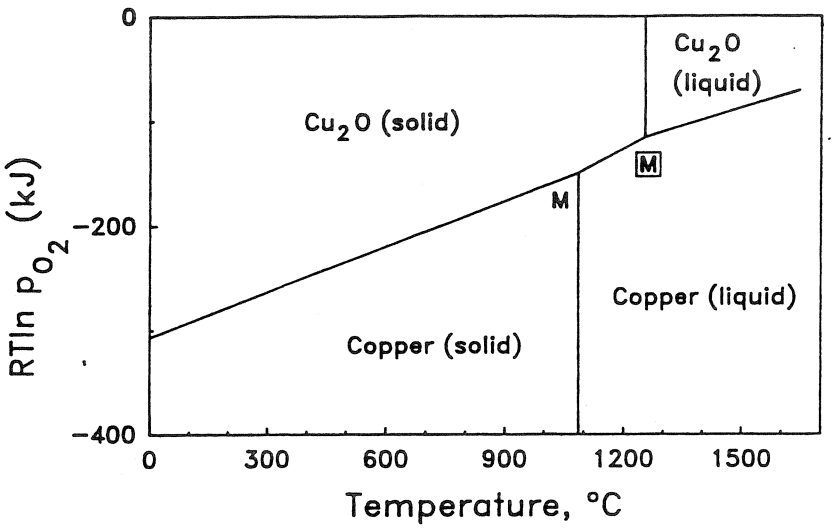

Figure 1-3. Predominance diagram (also known as a Gibbs energy-temperature diagram or Ellingham diagram) for the Cu–O system. Points M and M represent the melting points of the metal and oxide respectively.

conditions of two- and three-phase equilibrium.

1.3.3 Discussion of Predominance Diagrams

In this section discussion is limited to the assumption that there is no mutual solubility among the condensed phases. The calculation of predominance phase diagrams in which mutual solubility is taken into account is treated in Sec. 1.9, where the general geometrical rules governing predominance diagrams and their relationship to other types of phase diagrams are discussed.

We frequently encounter predominance diagrams with domains for solid, liquid, and even gaseous compounds which have been calculated *as if* the compounds were immiscible, even though they may actually be partially or even totally miscible. The boundary lines are then no longer phase boundaries, but are lines separating regions in which one species "predominates". The well known $E-pH$ or Pourbaix diagrams of aqueous chemistry are examples of such predominance diagrams.

Predominance diagrams may also be constructed when there are two or more base elements, as discussed by Bale (1990).

Predominance diagrams have found many applications in the fields of hot corrosion, roasting of ores, chemical vapor deposition, etc. A partial bibliography on their construction and applications includes Yokokowa (1999), Bale (1990), Bale et al. (1986), Kellogg and Basu (1960), Ingraham and Kellogg (1963), Pehlke (1973), Garrels and Christ (1965), Ingraham and Kerby (1967), Pilgrim and Ingraham (1967), Gulbransen and Jansson (1970), Pelton and Thompson (1975), Shatynski (1977), Stringer and Whittle (1975), Spencer and Barin (1979), Chu and Rahmel (1979), and Harshe and Venkatachalam (1984).

1.4 Thermodynamics of Solutions

1.4.1 Gibbs Energy of Mixing

Liquid gold and copper are completely miscible at all compositions. The Gibbs energy of one mole of liquid solution, g^l, at 1400 K is drawn in Fig. 1-4 as a function of composition expressed as *mole fraction*, X_{Cu}, of copper. Note that $X_{Au} = 1 - X_{Cu}$. The curve of g^l varies between the standard molar Gibbs energies of pure liquid Au and Cu, g^0_{Au} and g^0_{Cu}.

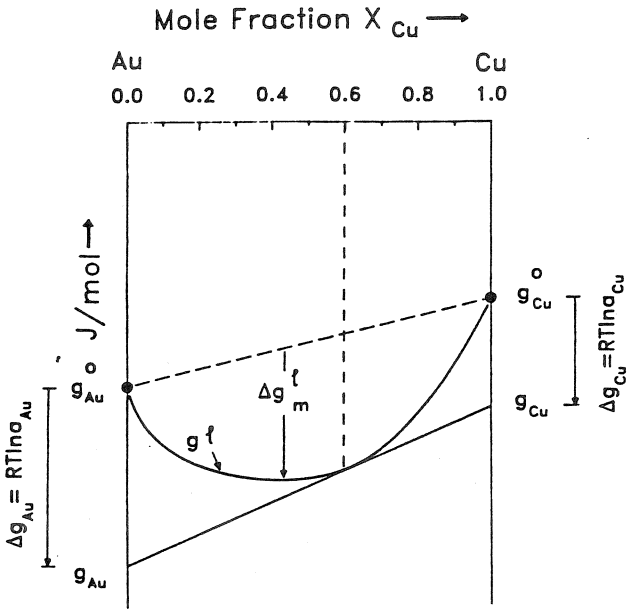

Figure 1-4. Molar Gibbs energy, g^l, of liquid Au–Cu alloys at constant temperature (1400 K) illustrating the tangent construction.

The function Δg^l_m shown on Fig. 1-4 is called the molar *Gibbs energy of mixing* of the liquid solution. It is defined as:

$$\Delta g^l_m = g^l - (X_{Au}\, g^0_{Au} + X_{Cu}\, g^0_{Cu}) \qquad (1\text{-}21)$$

It can be seen that Δg^l_m is the Gibbs energy change associated with the isothermal mixing of X_{Au} moles of pure liquid Au and X_{Cu} moles of pure liquid Cu to form one mole of solution:

$$X_{Au}\,\mathrm{Au(l)} + X_{Cu}\,\mathrm{Cu(l)} = 1 \text{ mole liquid solution} \qquad (1\text{-}22)$$

Note that for the solution to be stable it is necessary that Δg^l_m be negative.

1.4.2 Chemical Potential

The *partial molar Gibbs energy* of component i, g_i, also known as the *chemical potential*, μ_i, is defined as:

$$g_i = \mu_i = (\partial G/\partial n_i)_{T,P,n_j} \qquad (1\text{-}23)$$

where G is the Gibbs energy of the solution, n_i is the number of moles of component i, and the derivative is taken with all $n_j (j \neq i)$ constant.

In the example of the Au–Cu binary liquid solution, $g_{Cu} = (\partial G^l/\partial n_{Cu})_{T,P,n_{Au}}$, where $G^l = (n_{Cu} + n_{Au})\, g^l$. That is, g_{Cu}, which has units of J/mol, is the rate of change of the Gibbs energy of a solution as Cu is added. It can be seen that g_{Cu} is an intensive property of the solution which depends upon the composition and temperature but not upon the total amount of solution. That is, adding δn_{Cu} moles of copper to a solution of given composition will (in the limit as $\delta n_{Cu} \to 0$) result in a change in Gibbs energy, δG, which is independent of the total mass of the solution.

The reason that this property is called a *chemical potential* is illustrated by the following thought experiment. Imagine two systems, I and II, at the same temperature and separated by a membrane that permits only the passage of copper. The chemical potentials of copper in systems I and II are $g^I_{Cu} = \partial G^I/\partial n^I_{Cu}$ and $g^{II}_{Cu} = \partial G^{II}/\partial n^{II}_{Cu}$. Copper is transferred across the membrane, with $dn^I = -dn^{II}$. The change in the total Gibbs energy accompanying this transfer is then:

$$dG = d(G^I + G^{II}) = -(g^I_{Cu} - g^{II}_{Cu})\, dn^{II}_{Cu} \qquad (1\text{-}24)$$

If $g^I_{Cu} > g^{II}_{Cu}$, then $d(G^I + G^{II})$ is negative when dn^{II}_{Cu} is positive. That is, the total Gibbs energy will be decreased by a transfer of Cu from system I to system II. Hence, Cu will be transferred spontaneously from a system of higher g_{Cu} to a system of lower g_{Cu}. Therefore g_{Cu} is called the chemical potential of copper.

An important principle of phase equilibrium can now be stated. *When two or more phases are in equilibrium, the chemical potential of any component is the same in all phases.*

1.4.3 Tangent Construction

An important construction is illustrated in Fig. 1-4. If a tangent is drawn to the curve of g^l at a certain composition ($X_{Cu}=0.6$ in Fig. 1-4), then the intercepts of this tangent on the axes at $X_{Au}=1$ and $X_{Cu}=1$ are equal to g_{Au} and g_{Cu} respectively at this composition.

To prove this, we first consider that the Gibbs energy of the solution at constant T and P is a function of n_{Au} and n_{Cu}. Hence:

$$dG^l_{T,P} = \left(\frac{\partial G^l}{\partial n_{Au}}\right) dn_{Au} + \left(\frac{\partial G^l}{\partial n_{Cu}}\right) dn_{Cu} = g_{Au}\, dn_{Au} + g_{Cu}\, dn_{Cu} \qquad (1\text{-}25)$$

Eq. (1-25) can be integrated as follows:

$$\int_0^{G^l} dG^l = \int_0^{n_{Au}} g_{Au}\, dn_{Au} + \int_0^{n_{Cu}} g_{Cu}\, dn_{Cu}$$

$$G^l = g_{Au}\, n_{Au} + g_{Cu}\, n_{Cu} \qquad (1\text{-}26)$$

where the integration is performed at constant composition so that the intensive properties g_{Au} and g_{Cu} are constant. This integration can be thought of as describing a process in which a pre-mixed solution of constant composition is added to the system, which initially contains no material.

Dividing Eqs. (1-26) and (1-25) by $(n_{Au}+n_{Cu})$ we obtain expressions for the molar Gibbs energy and its derivative:

$$g^l = X_{Au}\, g_{Au} + X_{Cu}\, g_{Cu} \qquad (1\text{-}27)$$

and

$$dg^l = g_{Au}\, dX_{Au} + g_{Cu}\, dX_{Cu} \qquad (1\text{-}28)$$

Since $dX_{Au}=-dX_{Cu}$, it can be seen that Eqs. (1-27) and (1-28) are equivalent to the tangent construction shown in Fig. 1-4.

These equations may also be rearranged to give the following useful expression for a binary system:

$$g_i = g + (1-X_i)\, dg/dX_i \qquad (1\text{-}29)$$

1.4.4 Gibbs–Duhem Equation

Differentiation of Eq. (1-27) yields:

$$dg^l = (X_{Au}\, dg_{Au} + X_{Cu}\, dg_{Cu}) + (g_{Au}\, dX_{Au} + g_{Cu}\, dX_{Cu}) \qquad (1\text{-}30)$$

Comparison with Eq. (1-28) then gives the *Gibbs–Duhem equation* at constant T and P:

$$X_{Au}\, dg_{Au} + X_{Cu}\, dg_{Cu} = 0 \qquad (1\text{-}31)$$

1.4.5 Relative Partial Properties

The difference between the partial Gibbs energy g_i of a component in solution and the partial Gibbs energy g_i^0 of the same component in a *standard state* is called the *relative partial Gibbs energy* (or *relative chemical potential*), Δg_i. It is most usual to choose as standard state the pure component in the same phase at the same temperature. *The activity a_i of the component relative to the chosen standard state* is then defined in terms of Δg_i by the following equation, as illustrated in Fig. 1-4.

$$\Delta g_i = g_i - g_i^0 = \mu_i - \mu_i^0 = RT \ln a_i \qquad (1\text{-}32)$$

Note that g_i and μ_i are equivalent symbols, as are g_i^0 and μ_i^0, see Eq. (1-23).

From Fig. 1-4, it can be seen that:

$$\Delta g_m = X_{Au}\, \Delta g_{Au} + X_{Cu}\, \Delta g_{Cu} = RT\,(X_{Au} \ln a_{Au} + X_{Cu} \ln a_{Cu}) \qquad (1\text{-}33)$$

The Gibbs energy of mixing can be divided into enthalpy and entropy terms, as can the relative partial Gibbs energies:

$$\Delta g_m = \Delta h_m - T\, \Delta s_m \qquad (1\text{-}34)$$

$$\Delta g_i = \Delta h_i - T\, \Delta s_i \qquad (1\text{-}35)$$

Hence, the enthalpy and entropy of mixing may be expressed as:

$$\Delta h_m = X_{Au}\, \Delta h_{Au} + X_{Cu}\, \Delta h_{Cu} \qquad (1\text{-}36)$$

$$\Delta s_m = X_{Au}\, \Delta s_{Au} + X_{Cu}\, \Delta s_{Cu} \qquad (1\text{-}37)$$

and tangent constructions similar to that of Fig. 1-4 can be used to relate the relative *partial enthalpies and entropies* Δh_i and Δs_i to the *integral molar enthalpy of mixing* Δh_m and *integral molar entropy of mixing* Δs_m respectively.

1.4.6 Activity

The activity of a component in a solution was defined by Eq. (1-32).

Since a_i varies monotonically with g_i it follows that *when two or more phases are in equilibrium the activity of any component is the same in all phases*, provided that the activity in every phase is expressed with respect to the same standard state.

The use of activities in calculations of chemical equilibrium conditions is illustrated by the following example. A liquid solution of Au and Cu at 1400 K with $X_{Cu}=0.6$ is exposed to an atmosphere in which the oxygen partial pressure is $p_{O_2}=10^{-4}$ bar. Will Cu_2O be formed? The reaction is:

$$2\,Cu(l) + \tfrac{1}{2}O_2(g) = Cu_2O(sol) \qquad (1\text{-}38)$$

where the Cu(l) is in solution. If the reaction proceeds with the formation of dn moles of Cu_2O, then 2 dn moles of Cu are consumed, and the Gibbs energy of the Au–Cu solution changes by

$$-2\,(dG^l/dn_{Cu})\,dn$$

The total Gibbs energy then varies as:

$$\begin{aligned} dG/dn &= g_{Cu_2O} - \tfrac{1}{2}g_{O_2} - 2\,(dG^l/dn_{Cu}) \\ &= g_{Cu_2O} - \tfrac{1}{2}g_{O_2} - 2\,g_{Cu} \\ &= (g^0_{Cu_2O} - \tfrac{1}{2}g^0_{O_2} - 2\,g^0_{Cu}) \\ &\quad - \tfrac{1}{2}RT\ln p_{O_2} - 2RT\ln a_{Cu} \\ &= \Delta G^0 + RT\ln(p_{O_2}^{-1/2}\,a_{Cu}^{-2}) \\ &= \Delta G \end{aligned} \qquad (1\text{-}39)$$

For the reaction, Eq. (1-38), at 1400 K, $\Delta G^0=-68.35$ kJ (Barin et al., 1977). The activity of Cu in the liquid alloy at $X_{Cu}=0.6$ is $a_{Cu}=0.43$ (Hultgren et al., 1973). Substitution into Eq. (1-39) with $p_{O_2}=10^{-4}$ bar gives:

$$dG/dn = \Delta G = -50.84\ \text{kJ}$$

Hence under these conditions the reaction entails a decrease in the total Gibbs energy and so the copper will be oxidized.

1.4.7 Ideal Raoultian Solutions

An *ideal solution* or *Raoultian solution* is usually defined as one in which the activity of a component is equal to its mole fraction:

$$a_i^{ideal} = X_i \qquad (1\text{-}40)$$

(With a judicious choice of standard state, this definition can also encompass ideal Henrian solutions, as discussed in Sec. 1.5.11.)

However, this Raoultian definition of ideality is generally only useful for simple substitutional solutions. There are more useful definitions for other types of solutions such as interstitial solutions, ionic solutions, solutions of defects, polymer solutions, etc. That is, the most convenient definition of ideality depends upon the solution model. This subject will be discussed in Sec. 1.10. In the present section, Eq. (1-40) for an ideal substitutional solution will be developed with the Au–Cu solution as example.

In the ideal substitutional solution model it is assumed that Au and Cu atoms are nearly alike, with nearly identical radii and electronic structures. This being the case, there will be no change in bonding energy or volume upon mixing, so that the enthalpy of mixing is zero:

$$\Delta h_m^{ideal} = 0 \qquad (1\text{-}41)$$

Furthermore, and for the same reason, the Au and Cu atoms will be randomly distributed over the lattice sites. (In the case of a liquid solution we can think of the "lattice sites" as the instantaneous atomic positions.)

For a random distribution of N_{Au} gold atoms and N_{Cu} copper atoms over $(N_{Au}+N_{Cu})$ sites, Boltzmann's equation can be used to calculate the configurational entropy of the solution. This is the entropy associated with the spatial distribution of the particles:

$$S^{config} = k_B \ln (N_{Au}+N_{Cu})!/N_{Au}!\,N_{Cu}! \quad (1\text{-}42)$$

where k_B is Boltzmann's constant. The configurational entropies of pure Au and Cu are zero. Hence the configurational entropy of mixing, ΔS^{config}, will be equal to S^{config}. Furthermore, because of the assumed close similarity of Au and Cu, there will be no non-configurational contribution to the entropy of mixing. Hence, the entropy of mixing will be equal to S^{config}. Applying Stirling's approximation, which states that $\ln N! = [(N \ln N) - N]$ if N is large, yields:

$$\Delta S_m^{ideal} = S^{config} = -k_B (N_{Au}+N_{Cu}) \times \left(N_{Au} \ln \frac{N_{Au}}{N_{Au}+N_{Cu}} + N_{Cu} \ln \frac{N_{Cu}}{N_{Au}+N_{Cu}} \right) \quad (1\text{-}43)$$

For one mole of solution, $(N_{Au}+N_{Cu}) = N^0$, where N^0 = Avogadro's number. We also note that $(k_B N^0)$ is equal to the ideal gas constant R. Hence:

$$\Delta S_m^{ideal} = -R (X_{Au} \ln X_{Au} + X_{Cu} \ln X_{Cu}) \quad (1\text{-}44)$$

Therefore, since the ideal enthalpy of mixing is zero:

$$\Delta g_m^{ideal} = RT (X_{Au} \ln X_{Au} + X_{Cu} \ln X_{Cu}) \quad (1\text{-}45)$$

By comparing Eqs. (1-33) and (1-45) we obtain:

$$\Delta g_i^{ideal} = RT \ln a_i^{ideal} = RT \ln X_i \quad (1\text{-}46)$$

Hence Eq. (1-40) has been demonstrated for an ideal substitutional solution.

1.4.8 Excess Properties

In reality, Au and Cu atoms are not identical, and so Au–Cu solutions are not perfectly ideal. The difference between a solution property and its value in an ideal solution is called an *excess property*. The *excess Gibbs energy*, for example, is defined as:

$$g^E = \Delta g_m - \Delta g_m^{ideal} \quad (1\text{-}47)$$

Since the ideal enthalpy of mixing is zero, the excess enthalpy is equal to the enthalpy of mixing:

$$h^E = \Delta h_m - \Delta h_m^{ideal} = \Delta h_m \quad (1\text{-}48)$$

Hence:

$$g^E = h^E - T s^E = \Delta h_m - T s^E \quad (1\text{-}49)$$

Excess partial properties are defined similarly:

$$g_i^E = \Delta g_i - \Delta g_i^{ideal} = RT \ln a_i - RT \ln X_i \quad (1\text{-}50)$$

$$s_i^E = \Delta s_i - \Delta s_i^{ideal} = \Delta s_i + R \ln X_i \quad (1\text{-}51)$$

Also:

$$g_i^E = h_i^E - T s_i^E = \Delta h_i - T s_i^E \quad (1\text{-}52)$$

Equations analogous to Eqs. (1-33), (1-36) and (1-37) relate the integral and partial excess properties. For example, in Au–Cu solutions:

$$g^E = X_{Au}\, g_{Au}^E + X_{Cu}\, g_{Cu}^E \quad (1\text{-}53)$$

$$s^E = X_{Au}\, s_{Au}^E + X_{Cu}\, s_{Cu}^E \quad (1\text{-}54)$$

Tangent constructions similar to that of Fig. 1-4 can thus also be employed for excess properties, and an equation analogous

to Eq. (1-29) can be written:

$$g_i^E = g^E + (1 - X_i)\, dg^E/dX_i \qquad (1\text{-}55)$$

The Gibbs–Duhem equation, Eq. (1-31), also applies to excess properties:

$$X_{Au}\, dg_{Au}^E + X_{Cu}\, dg_{Cu}^E = 0 \qquad (1\text{-}56)$$

In Au–Cu alloys, g^E is negative. That is, Δg_m is more negative than Δg_m^{ideal} and so the solution is thermodynamically more stable than an ideal solution. We say that Au–Cu solutions exhibit *negative deviations from ideality*. If $g^E > 0$, then the solution is less stable than an ideal solution and is said to exhibit *positive deviations*.

1.4.9 Activity Coefficient

The *activity coefficient* of a component in a solution is defined as:

$$\gamma_i = a_i / X_i \qquad (1\text{-}57)$$

From Eq. (1-50):

$$g_i^E = RT \ln \gamma_i \qquad (1\text{-}58)$$

In an ideal solution $\gamma_i = 1$ and $g_i^E = 0$ for all components. If $\gamma_i < 1$, then $g_i^E < 0$ and by Eq. (1-50), $\Delta g_i < \Delta g_i^{ideal}$. That is, the component i is more stable in the solution than it would be in an ideal solution of the same composition. If $\gamma_i > 1$, then $g_i^E > 0$ and the driving force for the component to enter into solution is less than in the case of an ideal solution.

1.4.10 Multicomponent Solutions

The equations of this section were derived with a binary solution as an example. However, the equations apply equally to systems of any number of components. For instance, in a solution of components A–B–C–D ..., Eq. (1-33) becomes:

$$\Delta g_m = X_A \Delta g_A + X_B \Delta g_B + X_C \Delta g_C + X_D \Delta g_D + \ldots \qquad (1\text{-}59)$$

1.5 Binary Phase Diagrams

1.5.1 Systems with Complete Solid and Liquid Miscibility

The temperature–composition ($T-X$) phase diagram of the CaO–MnO system is shown in Fig. 1-5 (Schenck et al., 1964; Wu, 1990). The abscissa is the composi-

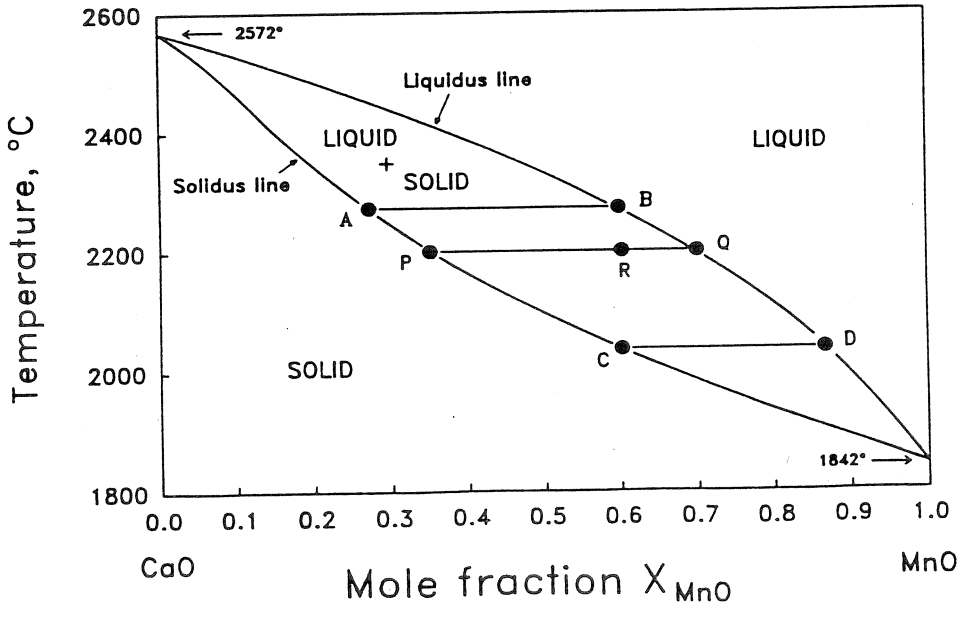

Figure 1-5. Phase diagram of the CaO–MnO system at $P = 1$ bar (after Schenck et al., 1964, and Wu, 1990).

tion, expressed as mole fraction of MnO, X_{MnO}. Note that $X_{MnO} = 1 - X_{CaO}$. Phase diagrams are also often drawn with the composition axis expressed as weight percent.

At all compositions and temperatures in the area above the line labelled liquidus, a single-phase liquid solution will be observed, while at all compositions and temperatures below the line labelled solidus, there will be a single-phase solid solution. A sample at equilibrium at a temperature and overall composition between these two curves will consist of a mixture of solid and liquid phases, the compositions of which are given by the liquidus and solidus compositions at that temperature. For example, a sample of overall composition $X_{MnO} = 0.60$ at $T = 2200\,°C$ (at point R in Fig. 1-5) will consist, at equilibrium, of a mixture of liquid of composition $X_{MnO} = 0.70$ (point Q) and solid of composition $X_{MnO} = 0.35$ (point P).

The line PQ is called a *tie-line* or *conode*. As the overall composition is varied at 2200 °C between points P and Q, the compositions of the solid and liquid phases remain fixed at P and Q, and only the relative proportions of the two phases change. From a simple mass balance, we can derive the *lever rule* for binary systems: (moles of liquid)/(moles of solid) $= PR/RQ$. Hence, at 2200 °C a sample with overall composition $X_{MnO} = 0.60$ consists of liquid and solid phases in the molar ratio $(0.60 - 0.35)/(0.70 - 0.60) = 2.5$. Were the composition axis expressed as weight percent, then the lever rule would give the weight ratio of the two phases.

Suppose that a liquid CaO–MnO solution with composition $X_{MnO} = 0.60$ is cooled very slowly from an initial temperature of about 2500 °C. When the temperature has decreased to the liquidus temperature 2270 °C (point B), the first solid appears, with a composition at point A ($X_{MnO} = 0.28$). As the temperature is decreased further, solid continues to precipitate with the compositions of the two phases at any temperature being given by the liquidus and solidus compositions at that temperature and with their relative proportions being given by the lever rule. Solidification is complete at 2030 °C, the last liquid to solidify having composition $X_{MnO} = 0.60$ (point C).

The process just described is known as equilibrium cooling. At any temperature during equilibrium cooling the solid phase has a uniform (homogeneous) composition. In the preceding example, the composition of the solid phase during cooling varies along the line APC. Hence, in order for the solid grains to have a uniform composition at any temperature, diffusion of CaO from the center to the surface of the growing grains must occur. Since solid-state diffusion is a relatively slow process, equilibrium cooling conditions are only approached if the temperature is decreased very slowly. If a sample of composition $X_{MnO} = 0.60$ is cooled very rapidly from the liquid, concentration gradients will be observed in the solid grains, with the concentration of MnO increasing towards the surface from a minimum of $X_{MnO} = 0.28$ (point A) at the center. Furthermore, in this case solidification will not be complete at 2030 °C since at 2030 °C the average concentration of MnO in the solid particles will be less than $X_{MnO} = 0.60$. These considerations are discussed more fully in Chapter 2 of this volume (Müller-Krumbhaar et al., 2001).

At $X_{MnO} = 0$ and $X_{MnO} = 1$ in Fig. 1-5 the liquidus and solidus curves meet at the equilibrium melting points, or *temperatures of fusion* of CaO and MnO, which are $T^0_{f(CaO)} = 2572\,°C$, $T^0_{f(MnO)} = 1842\,°C$.

The phase diagram is influenced by the total pressure, P. Unless otherwise stated,

$T-X$ diagrams are usually presented for $P=$const. = 1 bar. For equilibria involving only solid and liquid phases, the phase boundaries are typically shifted only by the order of a few hundredths of a degree per bar change in P. Hence, the effect of pressure upon the phase diagram is generally negligible unless the pressure is of the order of hundreds of bars. On the other hand, if gaseous phases are involved then the effect of pressure is very important. The effect of pressure will be discussed in Sec. 1.5.3.

1.5.2 Thermodynamic Origin of Phase Diagrams

In this section we first consider the thermodynamic origin of simple "lens-shaped" phase diagrams in binary systems with complete liquid and solid miscibility.

An example of such a diagram was given in Fig. 1-5. Another example is the Ge–Si phase diagram in the lowest panel of Fig. 1-6 (Hansen, 1958). In the upper three panels of Fig. 1-6, the molar Gibbs energies of the solid and liquid phases, g^s and g^l, at three temperatures are shown to scale. As illustrated in the top panel, g^s varies with composition between the standard molar Gibbs energies of pure solid Ge and of pure solid Si, $g_{Ge}^{0(s)}$ and $g_{Si}^{0(s)}$, while g^l varies between the standard molar Gibbs energies of the pure liquid components $g_{Ge}^{0(l)}$ and $g_{Si}^{0(l)}$.

The difference between $g_{Ge}^{0(l)}$ and $g_{Si}^{0(s)}$ is equal to the standard molar Gibbs energy of fusion (melting) of pure Si, $\Delta g_{f(Si)}^0 = (g_{Si}^{0(l)} - g_{Si}^{0(s)})$. Similarly, for Ge, $\Delta g_{f(Ge)}^0 = (g_{Ge}^{0(l)} - g_{Ge}^{0(s)})$. The Gibbs energy of fusion of a pure component may be written as:

$$\Delta g_f^0 = \Delta h_f^0 - T\,\Delta s_f^0 \qquad (1\text{-}60)$$

where Δh_f^0 and Δs_f^0 are the standard molar enthalpy and entropy of fusion.

Since, to a first approximation, Δh_f^0 and Δs_f^0 are independent of T, Δg_f^0 is approximately a linear function of T. If $T > T_f^0$, then Δg_f^0 is negative. If $T < T_f^0$, then Δg_f^0 is positive. Hence, as seen in Fig. 1-6, as T decreases, the g^s curve descends relative to g^l. At 1500 °C, $g^l < g^s$ at all compositions. Therefore, by the principle that a system always seeks the state of minimum Gibbs energy at constant T and P, the liquid phase is stable at all compositions at 1500 °C.

At 1300 °C, the curves of g^s and g^l cross. The line $P_1 Q_1$, which is the *common tangent* to the two curves, divides the composition range into three sections. For compositions between pure Ge and P_1, a single-phase liquid is the state of minimum Gibbs energy. For compositions between Q_1 and pure Si, a single-phase solid solution is the stable state. Between P_1 and Q_1, a total Gibbs energy lying on the tangent line $P_1 Q_1$ may be realized if the system adopts a state consisting of two phases with compositions at P_1 and Q_1 and with relative proportions given by the lever rule. Since the tangent line $P_1 Q_1$ lies below both g^s and g^l, this two-phase state is more stable than either phase alone. Furthermore, no other line joining any point on g^l to any point on g^s lies below the line $P_1 Q_1$. Hence, this line represents the true equilibrium state of the system, and the compositions P_1 and Q_1 are the liquidus and solidus compositions at 1300 °C.

As T is decreased to 1100 °C, the points of common tangency are displaced to higher concentrations of Ge. For $T < 937$ °C, $g^s < g^l$ at all compositions.

It was shown in Fig. 1-4 that if a tangent is drawn to a Gibbs energy curve, then the intercept of this tangent on the axis at $X_i = 1$ is equal to the partial Gibbs energy or chemical potential g_i of component i. The *common tangent construction* of Fig. 1-6 thus ensures that the chemical potentials of

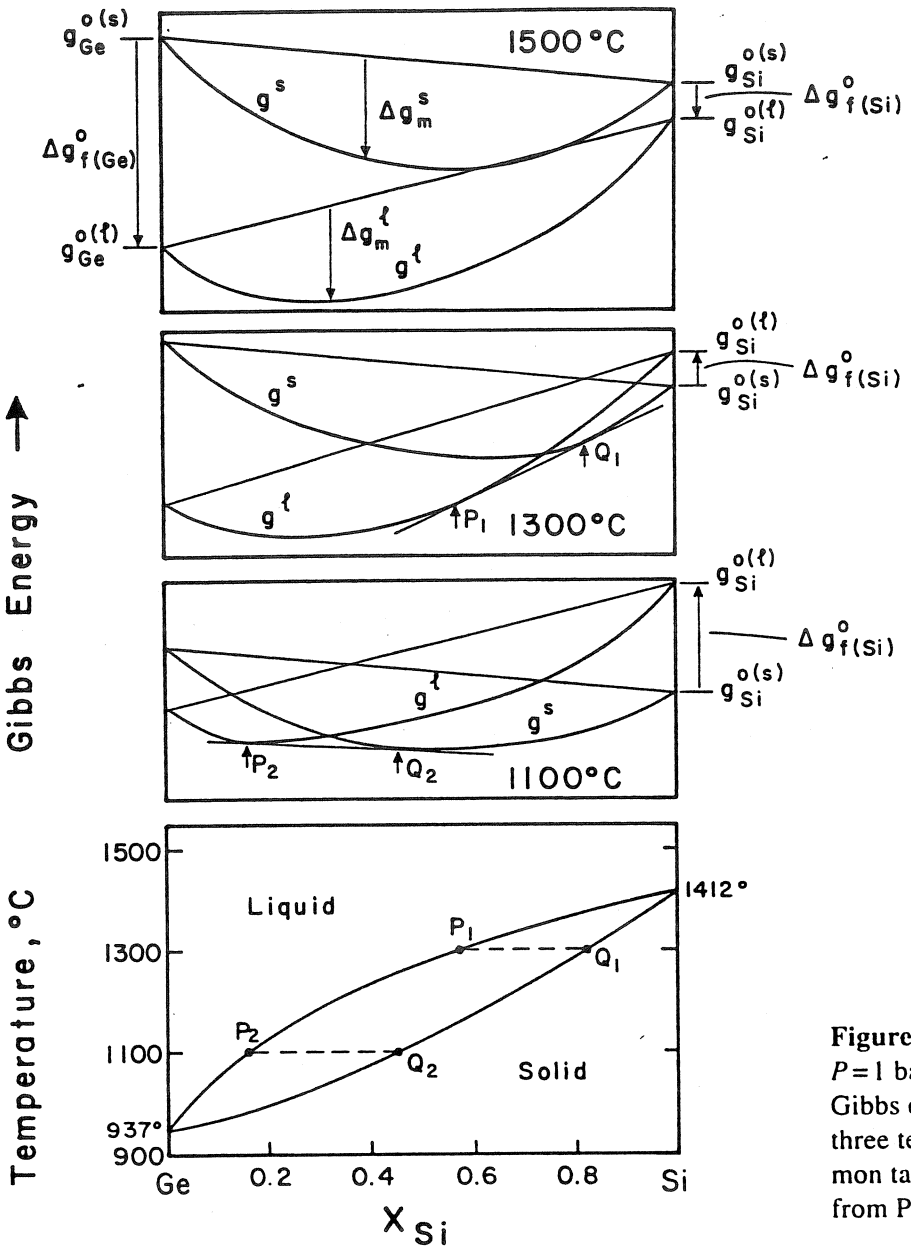

Figure 1-6. Ge–Si phase diagram at $P = 1$ bar (after Hansen, 1958) and Gibbs energy composition curves at three temperatures, illustrating the common tangent construction (reprinted from Pelton, 1983).

Ge and Si are equal in the solid and liquid phases at equilibrium. That is:

$$g^{l}_{Ge} = g^{s}_{Ge} \tag{1-61}$$

$$g^{l}_{Si} = g^{s}_{Si} \tag{1-62}$$

This equality of chemical potentials was shown in Sec. 1.4.2 to be the criterion for phase equilibrium. That is, the common tangent construction simultaneously minimizes the total Gibbs energy and ensures the equality of the chemical potentials, thereby showing that these are equivalent criteria for equilibrium between phases.

If we rearrange Eq. (1-61), subtracting the Gibbs energy of fusion of pure Ge, $\Delta g^0_{f(Ge)} = (g^{0(l)}_{Ge} - g^{0(s)}_{Ge})$, from each side, we get:

$$(g^{l}_{Ge} - g^{0(l)}_{Ge}) - (g^{s}_{Ge} - g^{0(s)}_{Ge}) = -(g^{0(l)}_{Ge} - g^{0(s)}_{Ge}) \tag{1-63}$$

Using Eq. (1-32), we can write Eq. (1-63) as:

$$\Delta g^{l}_{Ge} - \Delta g^{s}_{Ge} = -\Delta g^{0}_{f(Ge)} \tag{1-64}$$

or

$$RT \ln a^{l}_{Ge} - RT \ln a^{s}_{Ge} = -\Delta g^{0}_{f(Ge)} \tag{1-65}$$

where a^{l}_{Ge} is the activity of Ge (with respect to pure liquid Ge as standard state) in the liquid solution on the liquidus, and a^{s}_{Ge} is the activity of Ge (with respect to pure solid Ge as standard state) in the solid solution on the solidus. Starting with Eq. (1-62), we can derive a similar expression for the other component:

$$RT \ln a^{l}_{Si} - RT \ln a^{s}_{Si} = -\Delta g^{0}_{f(Si)} \qquad (1\text{-}66)$$

Eqs. (1-65) and (1-66) are equivalent to the common tangent construction.

It should be noted that absolute values of Gibbs energies cannot be defined. Hence, the relative positions of $g^{0(l)}_{Ge}$ and $g^{0(l)}_{Si}$ in Fig. 1-6 are completely arbitrary. However, this is immaterial for the preceding discussion, since displacing both $g^{0(l)}_{Si}$ and $g^{0(s)}_{Si}$ by the same arbitrary amount relative to $g^{0(l)}_{Ge}$ and $g^{0(s)}_{Ge}$ will not alter the compositions of the points of common tangency.

It should also be noted that in the present discussion of equilibrium phase diagrams we are assuming that the physical dimensions of the single-phase regions in the system are sufficiently large that surface (interfacial) energy contributions to the Gibbs energy can be neglected. For very fine grain sizes in the sub-micron range, however, surface energy effects can noticeably influence the phase boundaries.

The shape of the two-phase (solid + liquid) "lens" on the phase diagram is determined by the Gibbs energies of fusion, Δg^{0}_{f}, of the components and by the mixing terms, Δg^{s} and Δg^{l}. In order to observe how the shape is influenced by varying Δg^{0}_{f}, let us consider a hypothetical system A–B in which Δg^{s} and Δg^{l} are ideal Raoultian (Eq. (1-45)). Let $T^{0}_{f(A)} = 800$ K and $T^{0}_{f(B)} = 1200$ K. Furthermore, assume that the entropies of fusion of A and B are equal and temperature-independent. The enthalpies of fusion are then given from Eq. (1-60) by the expression $\Delta h^{0}_{f} = T^{0}_{f} \Delta s^{0}_{f}$ since $\Delta g^{0}_{f} = 0$ when $T = T^{0}_{f}$. Calculated phase diagrams for $\Delta s^{0}_{f} = 3$, 10 and 30 J/mol K are shown in Fig. 1-7. A value of $\Delta s^{0}_{f} \approx 10$ is typical of most metals. However, when the components are ionic compounds such as ionic oxides, halides, etc., Δs^{0}_{f} can be significantly larger since there are several ions per formula unit. Hence, two-phase "lenses" in binary ionic salt or oxide phase diagrams tend to be "fatter" than those encountered in alloy systems. If we are considering vapor–liquid equilibria rather than solid–liquid equilibria, then the shape is determined by the entropy of vaporization, Δs^{0}_{v}. Since Δs^{0}_{v} is usually an order of magnitude larger than Δs^{0}_{f}, two-phase (liquid + vapor) lenses tend to be

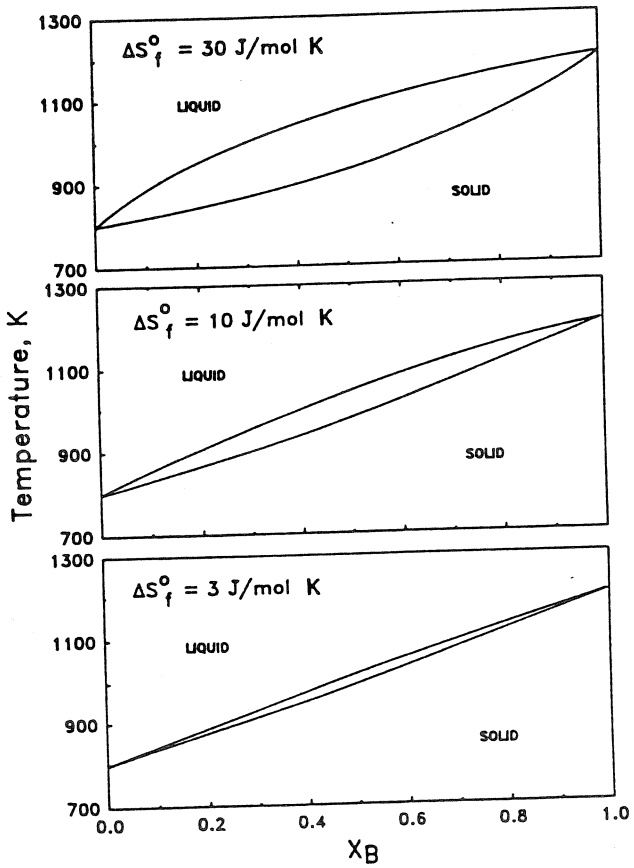

Figure 1-7. Phase diagram of a system A–B with ideal solid and liquid solutions. Melting points of A and B are 800 and 1200 K, respectively. Diagrams are calculated for entropies of fusion $\Delta S^{0}_{f(A)} = \Delta S^{0}_{f(B)} =$ 3, 10 and 30 J/mol K.

very wide. For equilibria between two solid solutions of different crystal structure, the shape is determined by the entropy of solid–solid transformation, which is usually smaller than the entropy of fusion by approximately an order of magnitude. Therefore two-phase (solid + solid) lenses tend to be very narrow.

1.5.3 Pressure–Composition Phase Diagrams

Let us consider liquid–vapor equilibrium with complete miscibility, using as an example the Zn–Mg system. Curves of g^v and g^l can be drawn at any given T and P, as in the upper panel of Fig. 1-8, and the common tangent construction then gives the equilibrium vapor and liquid compositions. The phase diagram depends upon the Gibbs energies of vaporization of the components $\Delta g_{v(Zn)}$ and $\Delta g_{v(Mg)}$ as shown in Fig. 1-8.

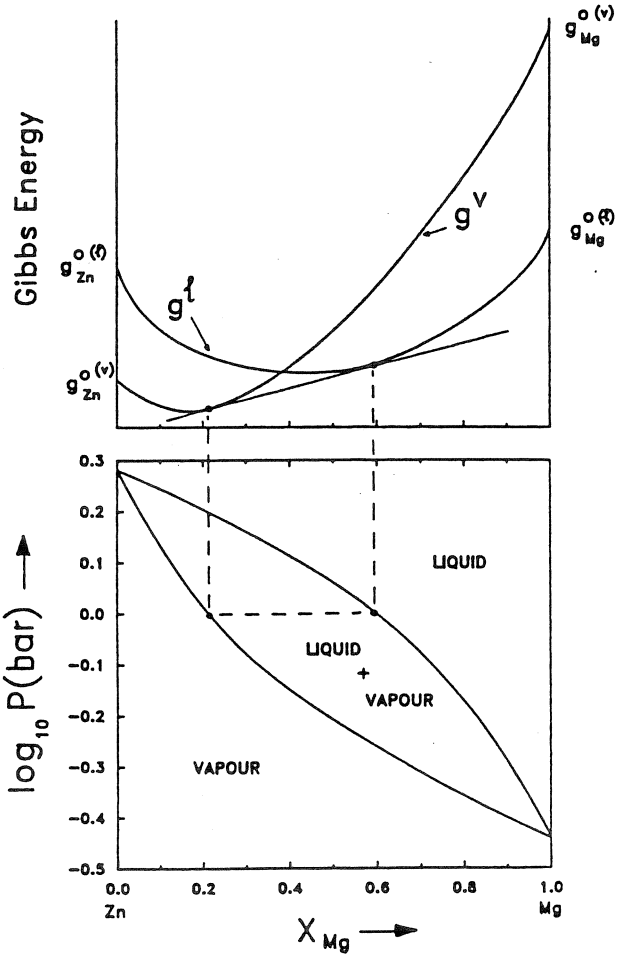

Figure 1-8. Pressure–composition phase diagram of the Zn–Mg system at 1250 K calculated for ideal vapor and liquid solutions. Upper panel illustrates common tangent construction at a constant pressure.

To generate the isothermal pressure–composition (P–X) phase diagram in the lower panel of Fig. 1-8 we require the Gibbs energies of vaporization as functions of P. Assuming monatomic ideal vapors and assuming that pressure has negligible effect upon the Gibbs energy of the liquid, we can write:

$$\Delta g_{v(i)} = \Delta g^0_{v(i)} + RT \ln P \qquad (1\text{-}67)$$

where $\Delta g_{v(i)}$ is the standard Gibbs energy of vaporization (when $P = 1$ bar), which is given by:

$$\Delta g^0_{v(i)} = \Delta h^0_{v(i)} - T\,\Delta s^0_{v(i)} \qquad (1\text{-}68)$$

For example, the enthalpy of vaporization of Zn is $\Delta h^0_{v(Zn)} = 115\,300$ J/mol at its normal boiling point of 1180 K (Barin et al., 1977). Assuming that Δh^0_v is independent of T, we calculate from Eq. (1-68) that $\Delta s^0_{v(Zn)} = 115\,300/1180 = 97.71$ J/mol K. From Eq. (1-67), $\Delta g_{v(Zn)}$ at any T and P is thus given gy:

$$\Delta g_{v(Zn)} = (115\,300 - 97.71\,T) + RT \ln P \qquad (1\text{-}69)$$

A similar expression can be derived for the other component Mg.

At constant temperature, then, the curve of g^v in Fig. 1-8 descends relative to g^l as the pressure is lowered, and the P–X phase diagram is generated by the common tangent construction. The diagram at 1250 K in Fig. 1-8 was calculated under the assumption of ideal liquid and vapor mixing ($g^{E(l)} = 0$, $g^{E(v)} = 0$).

P–X phase diagrams involving liquid–solid or solid–solid equilibria can be calculated in a similar fashion through the fol-

lowing general equation, which gives the effect of pressure upon the Gibbs energy change for the transformation of one mole of pure component i from an α-phase to a β-phase:

$$\Delta g_{\alpha\to\beta} = \Delta g^0_{\alpha\to\beta} + \int_{P=1}^{P} (v_i^\beta - v_i^\alpha)\,dP \qquad (1\text{-}70)$$

where $\Delta g^0_{\alpha\to\beta}$ is the standard ($P=1$ bar) Gibbs energy of transformation, and v_i^β and v_i^α are the molar volumes.

1.5.4 Minima and Maxima in Two-Phase Regions

As discussed in Sec. 1.4.8, the Gibbs energy of mixing Δg_m may be expressed as the sum of an ideal term Δg_m^{ideal} and an excess term g^E. As has just been shown in Sec. 1.5.2, if Δg_m^s and Δg_m^l for the solid and liquid phases are both ideal, then a "lens-shaped" two-phase region always results. However in most systems even approximately ideal behavior is the exception rather than the rule.

Curves of g^s and g^l for a hypothetical system A–B are shown schematically in Fig. 1-9 at a constant temperature (below the melting points of pure A and B) such that the solid state is the stable state for both pure components. However, in this system $g^{E(l)} < g^{E(s)}$, so that g^s presents a flatter curve than does g^l and there exists a central composition region in which $g^l < g^s$. Hence, there are two common tangent lines, P_1Q_1 and P_2Q_2. Such a situation gives rise to a phase diagram with a minimum in the two-phase region, as observed in the Na_2CO_3–K_2CO_3 system (Dessureault et al., 1990) shown in Fig. 1-10. At a composition and temperature corresponding to the minimum point, liquid and solid of the same composition exist in equilibrium.

A two-phase region with a minimum point as in Fig. 1-10 may be thought of as a two-phase "lens" which has been "pushed down" by virtue of the fact that the liquid is relatively more stable than the solid. Thermodynamically, this relative stability is expressed as $g^{E(l)} < g^{E(s)}$.

Conversely, if $g^{E(l)} > g^{E(s)}$ to a sufficient extent, then a two-phase region with a maximum will result. Such maxima in (liquid + solid) or (solid + solid) two-phase regions are nearly always associated with the existence of an intermediate phase, as will be discussed in Sec. 1.5.10.

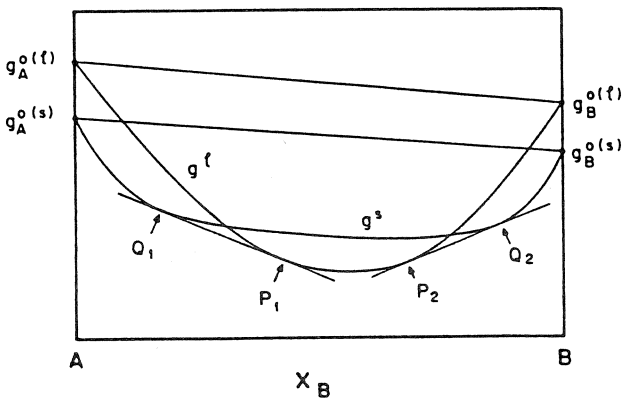

Figure 1-9. Isothermal Gibbs energy-composition curves for solid and liquid phases in a system A–B in which $g^{E(l)} > g^{E(s)}$. A phase diagram of the type of Fig. 1-10 results.

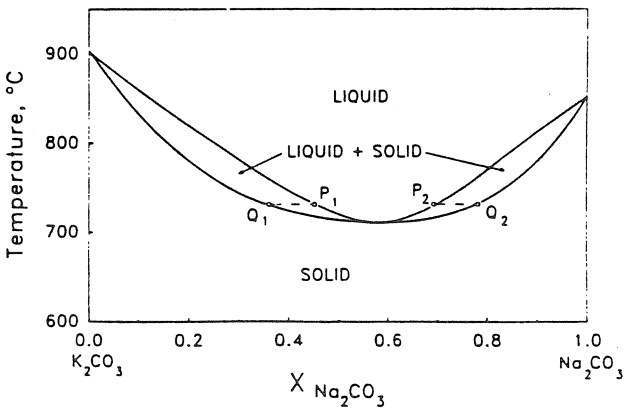

Figure 1-10. Phase diagram of the K_2CO_3–Na_2CO_3 system at $P=1$ bar (Dessureault et al., 1990).

1.5.5 Miscibility Gaps

If $g^E > 0$, then the solution is thermodynamically less stable than an ideal solution. This can result from a large difference in size of the component atoms, ions or molecules, which will lead to a (positive) lattice strain energy, or from differences in electronic structure, or from other factors.

In the Au–Ni system, g^E is positive in the solid phase. In the top panel of Fig. 1-11, $g^{E(s)}$ is plotted at 1200 K (Hultgren et al., 1973) and the ideal Gibbs energy of mixing, Δg_m^{ideal}, is also plotted at 1200 K. The sum of these two terms is the Gibbs energy of mixing of the solid solution, Δg_m^s, which is plotted at 1200 K as well as at other temperatures in the central panel of Fig. 1-11. Now, from Eq. (1-45), Δg_m^{ideal} is always negative and varies directly with T, whereas g^E varies less rapidly with temperature. As a result, the sum $\Delta g_m^s = \Delta g_m^{ideal} + g^E$ becomes less negative as T decreases. However, the limiting slopes to the Δg_m^{ideal} curve at $X_{Au} = 1$ and $X_{Ni} = 1$ are both infinite, whereas the limiting slopes of g^E are always finite (Henry's Law). Hence, Δg_m^s will always be negative as $X_{Au} \to 1$ and $X_{Ni} \to 1$ no matter how low the temperature. As a result, below a certain temperature the curve of Δg_m^s will exhibit two negative "humps". Common tangent lines P_1Q_1, P_2Q_2, P_3Q_3 to the two humps at different temperatures define the ends of tie-lines of a two-phase solid–solid *miscibility gap* in the Au–Ni phase diagram, which is shown in the lower panel in Fig. 1-11 (Hultgren et al., 1973). The peak of the gap occurs at the *critical* or *consolute* temperature and composition, T_c and X_c.

When $g^{E(s)}$ is positive for the solid phase in a system it is usually also the case that $g^{E(l)} < g^{E(s)}$ since the unfavorable factors (such as a difference in atomic dimensions) which are causing $g^{E(s)}$ to be positive will have less of an effect upon $g^{E(l)}$ in the liquid phase owing to the greater flexibility of the liquid structure to accommodate different atomic sizes, valencies, etc. Hence, a solid–solid miscibility gap is often associated with a minimum in the two-phase (solid + liquid) region, as is the case in the Au–Ni system.

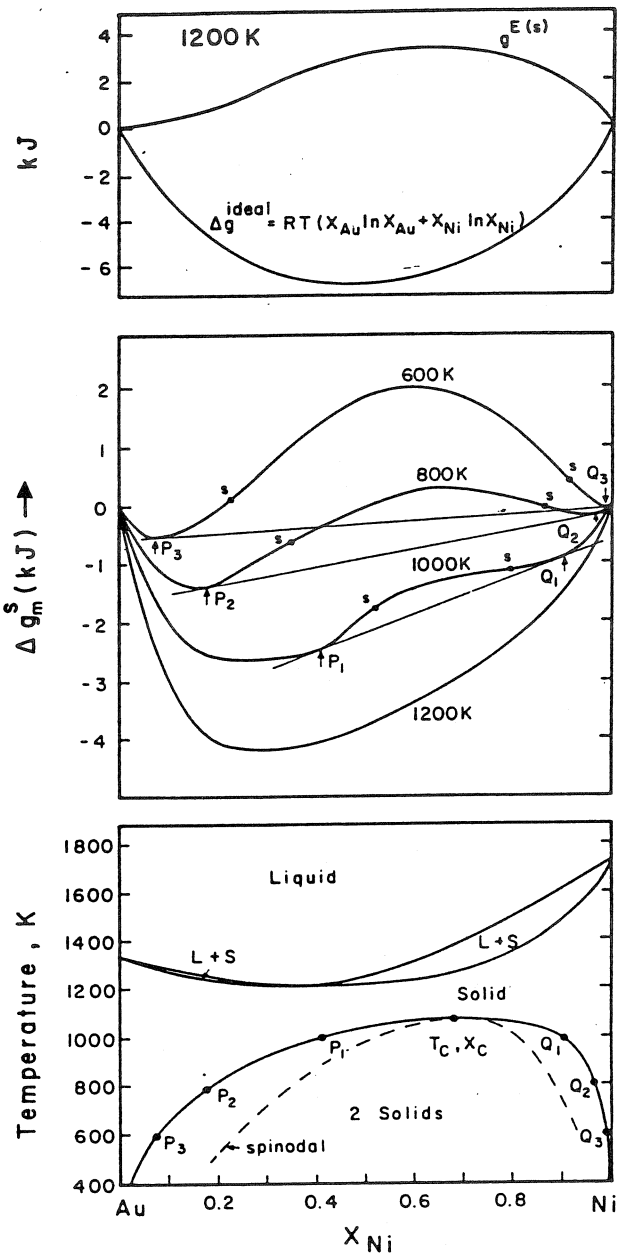

Figure 1-11. Phase diagram (after Hultgren et al., 1973) and Gibbs energy–composition curves of solid solutions for the Au–Ni system at $P = 1$ bar. Letters "s" indicate spinodal points (Reprinted from Pelton, 1983).

Below the critical temperature the curve of Δg^s_m exhibits two inflection points, indicated by the letter "s" in Fig. 1-11. These are known as the *spinodal points*. On the phase diagram their locus traces out the *spinodal curve* (Fig. 1-11). The spinodal curve is not part of the equilibrium phase diagram, but it is important in the kinetics of phase separation, as discussed in Chapter 6 (Binder and Fratzl, 2001).

1.5.6 Simple Eutectic Systems

The more positive g^E is in a system, the higher is T_c and the wider is the miscibility gap at any temperature. Suppose that $g^{E(s)}$ is so positve that T_c is higher than the minimum in the (solid + liquid) region. The result will be a phase diagram such as that of the MgO–CaO system shown in Fig. 1-12 (Doman et al., 1963; Wu, 1990).

The lower panel of Fig. 1-12 shows the Gibbs energy curves at 2450 °C. The two common tangents define two two-phase regions. As the temperature is decreased below 2450 °C, the g^s curve descends relative to g^l and the two points of tangency P_1 and P_2 approach each other until, at $T =$ 2374 °C, P_1 and P_2 become coincident at the composition E. That is, at $T = 2374$ °C

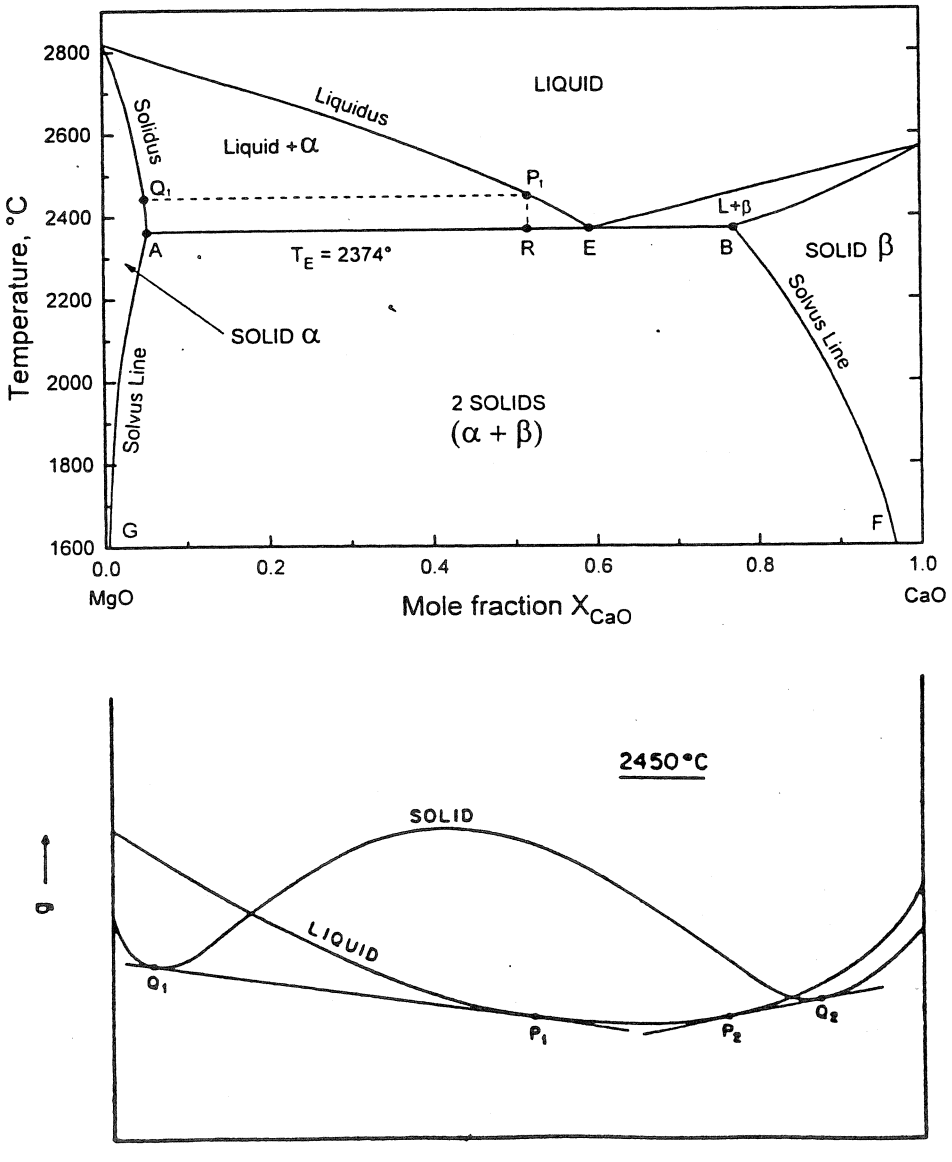

Figure 1-12. Phase diagram at $P = 1$ bar (after Doman et al., 1963, and Wu, 1990) and Gibbs energy–composition curves at 2450 °C for the MgO–CaO system. Solid MgO and CaO have the same crystal structure.

there is just one common tangent line contacting the two portions of the g^s curve at compositions A and B and contacting the g^l curve at E. This temperature is known as the *eutectic temperature*, T_E, and the composition E is the *eutectic composition*. For temperatures below T_E, g^l lies completely above the common tangent to the two portions of the g^s curve and so for $T<T_E$ a solid–solid miscibility gap is observed. The phase boundaries of this two-phase region are called the *solvus* lines. The word eutectic is from the Greek for "to melt well" since the system has its lowest melting point at the eutectic composition E.

This description of the thermodynamic origin of simple eutectic phase diagrams is strictly correct only if the pure solid components A and B have the same crystal structure. Otherwise, a curve for g^s which is continuous at all compositions cannot be drawn.

Suppose a liquid MgO–CaO solution of composition $X_{CaO}=0.52$ (composition P_1) is cooled from the liquid state very slowly under equilibrium conditions. At 2450 °C the first solid appears with composition Q_1. As T decreases further, solidification continues with the liquid composition following the liquidus curve from P_1 to E and the composition of the solid phase following the solidus curve from Q_1 to A. The relative proportions of the two phases at any T are given by the lever rule. At a temperature just above T_E, two phases are observed: a solid of composition A and a liquid of composition E. At a temperature just below T_E, two solids with compositions A and B are observed. Therefore, at T_E, during cooling, the following *binary eutectic reaction* occurs:

$$\text{liquid} \rightarrow \text{solid}_1 + \text{solid}_2 \qquad (1\text{-}71)$$

Under equilibrium conditions the temperature will remain constant at $T=T_E$ until all the liquid has solidified, and during the reaction the compositions of the three phases will remain fixed at A, B and E. For this reason the eutectic reaction is called an *invariant* reaction. More details on eutectic solidification may be found in Chapter 2 (Müller-Krumbhaar et al., 2001).

1.5.7 Regular Solution Theory

Many years ago Van Laar (1908) showed that the thermodynamic origin of a great many of the observed features of binary phase diagrams can be illustrated at least qualitatively by simple regular solution theory. A simple *regular solution* is one for which:

$$g^E = X_A X_B(\omega - \eta T) \qquad (1\text{-}72)$$

where ω and η are parameters independent of temperature and composition. Substituting Eq. (1-72) into Eq. (1-29) yields, for the partial properties:

$$g_A^E = X_B^2(\omega - \eta T), \quad g_B^E = X_A^2(\omega - \eta T) \qquad (1\text{-}73)$$

Several liquid and solid solutions conform approximately to regular solution behavior, particularly if g^E is small. Examples may be found for alloys, molecular solutions, and ionic solutions such as molten salts and oxides, among others. (The very low values of g^E observed for gaseous solutions generally conform very closely to Eq. (1-72).)

To understand why this should be so, we only need a very simple model. Suppose that the atoms or molecules of the components A and B mix substitutionally. If the atomic (or molecular) sizes and electronic structures of A and B are similar, then the distribution will be nearly random, and the configurational entropy will be nearly ideal. That is:

$$g^E \approx \Delta h_m - T S^{E(\text{non-config})} \qquad (1\text{-}74)$$

More will be said on this point in Sec. 1.10.5.

We now assume that the bond energies ε_{AA}, ε_{BB} and ε_{AB} of nearest-neighbor pairs are independent of temperature and composition and that the average nearest-neighbor coordination number, Z, is also constant. Finally, we assume that the enthalpy of mixing results mainly from the change in the total energy of nearest-neighbor pair bonds.

In one mole of solution there are $(N^0 Z/2)$ neareast-neighbor pair bonds, where N^0 is Avogadro's number. Since the distribution is assumed random, the probability that a given bond is an A–A bond is equal to X_A^2. The probabilities of B–B and A–B bonds are, respectively, X_B^2 and $2X_A X_B$. The molar enthalpy of mixing is then equal to the sum of the energies of the nearest-neighbor bonds in one mole of solution, minus the energy of the A–A bonds in X_A moles of pure A and the energy of the B–B bonds in X_B moles of pure B:

$$\begin{aligned}\Delta h_m &= (N^0 Z/2) \\ &\quad \times (X_A^2 \varepsilon_{AA} + X_B^2 \varepsilon_{BB} + 2X_{AB} \varepsilon_{AB}) \\ &\quad - (N^0 Z/2)(X_A \varepsilon_{AA}) - (N^0 Z/2)(X_B \varepsilon_{BB}) \\ &= (N^0 Z)[\varepsilon_{AB} - (\varepsilon_{AA} + \varepsilon_{BB})/2] X_A X_B \\ &= \omega X_A X_B \end{aligned} \qquad (1\text{-}75)$$

We now define σ_{AB}, σ_{AA} and σ_{BB} as the vibrational entropies of nearest-neighbor pair bonds. Following an identical argument to that just presented for the bond energies we obtain:

$$\begin{aligned} &s^{E(\text{non-config})} \\ &= (N^0 Z)[\sigma_{AB} - (\sigma_{AA} + \sigma_{BB})/2] = \eta X_A X_B \end{aligned} \qquad (1\text{-}76)$$

Eq. (1-72) has thus been derived. If A–B bonds are stronger than A–A and B–B bonds, then $(\varepsilon_{AB} - \eta_{AB} T) < [(\varepsilon_{AA} - \eta_{AA} T)/2 + (\varepsilon_{BB} - \eta_{BB} T)/2]$. Hence, $(\omega - \eta T) < 0$ and $g^E < 0$. That is, the solution is rendered more stable. If the A–B bonds are relatively weak, then the solution is rendered less stable, $(\omega - \eta T) > 0$ and $g^E > 0$.

Simple non-polar molecular solutions and ionic solutions such as molten salts often exhibit approximately regular behavior. The assumption of additivity of the energy of pair bonds is probably reasonably realistic for van der Waals or coulombic forces. For alloys, the concept of a pair bond is, at best, vague, and metallic solutions tend to exhibit larger deviations from regular behavior.

In several solutions it is found that $|\eta T| < |\omega|$ in Eq. (1-72). That is, $g^E \approx \Delta h_m = \omega X_A X_B$, and to a first approximation g^E is independent of T. This is more often the case in non-metallic solutions than in metallic solutions.

1.5.8 Thermodynamic Origin of Simple Phase Diagrams Illustrated by Regular Solution Theory

Figure 1-13 shows several phase diagrams, calculated for a hypothetical system A–B containing a solid and a liquid phase with melting points of $T^0_{f(A)} = 800$ K and $T^0_{f(B)} = 1200$ K and with entropies of fusion of both A and B set to 10 J/mol K, which is a typical value for metals. The solid and liquid phases are both regular with temperature-independent excess Gibbs energies

$$g^{E(s)} = \omega^s X_A X_B \quad \text{and} \quad g^{E(l)} = \omega^l X_A X_B$$

The parameters ω^s and ω^l have been varied systematically to generate the various panels of Fig. 1-13.

In panel (n) both phases are ideal. Panels (l) to (r) exhibit minima or maxima depending upon the sign and magnitude of $(g^{E(l)} - g^{E(s)})$, as has been discussed in Sec. 1.5.4. In panel (h) the liquid is ideal but positive deviations in the solid give rise to a solid–solid miscibility gap as discussed in Sec. 1.5.6. On passing from panel (h) to

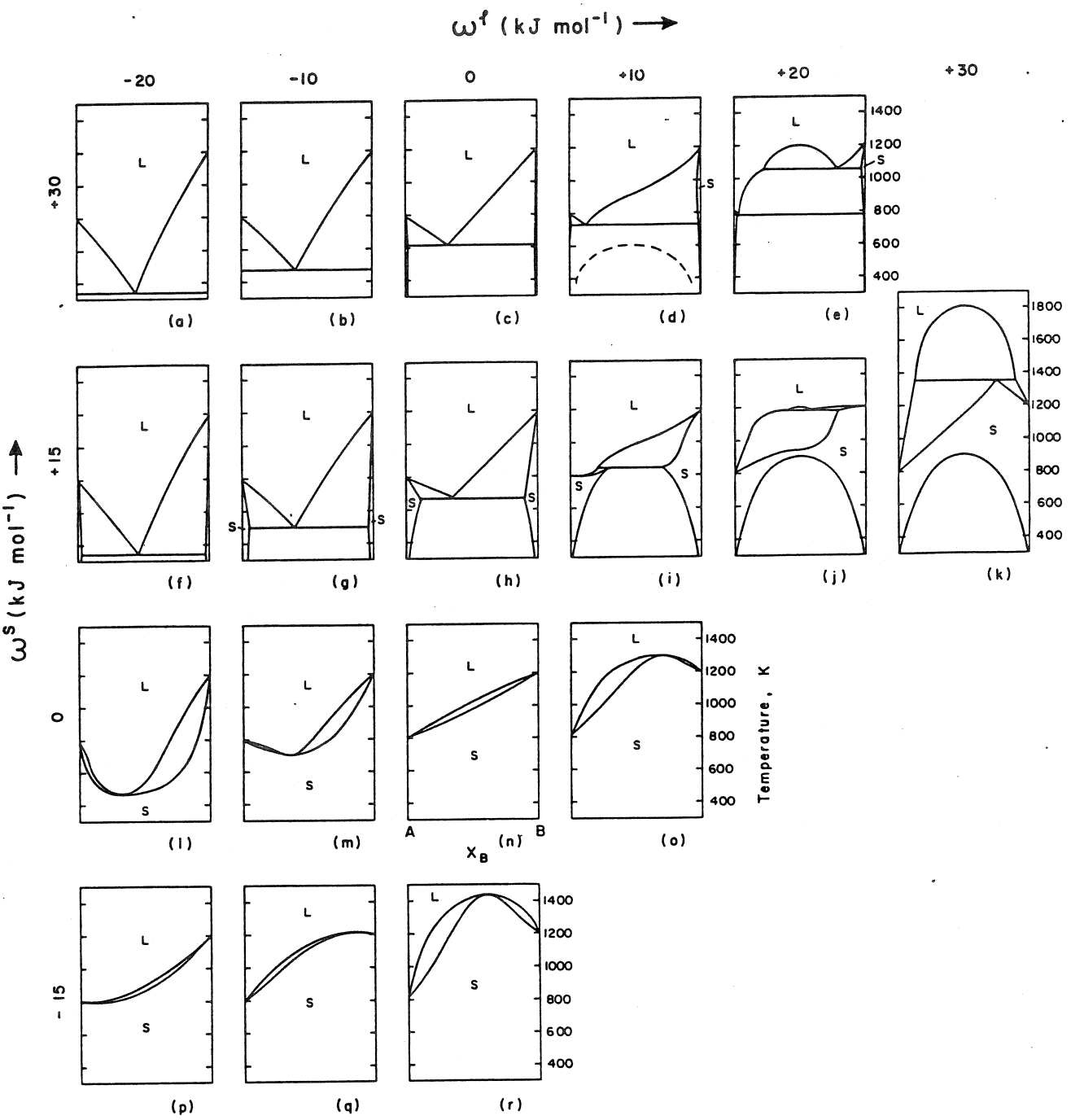

Figure 1-13. Topological changes in the phase diagram for a system A–B with regular solid and liquid phases, brought about by systematic changes in the regular solution parameters ω^s and ω^l. Melting points of pure A and B are 800 K and 1200 K. Entropies of fusion of both A and B are 10.0 J/mol K (Pelton and Thompson, 1975). The dashed curve in panel (d) is the metastable liquid miscibility gap (Reprinted from Pelton, 1983).

panel (c), an increase in $g^{E(s)}$ results in a widening of the miscibility gap so that the solubility of A in solid B and of B in solid A decreases. Panels (a) to (c) illustrate that negative deviations in the liquid cause a relative stabilization of the liquid with resultant lowering of the eutectic temperature.

Eutectic phase diagrams are often drawn with the maximum solid solubility occurring at the eutectic temperature (as in Fig. 1-12). However, panel (d) of Fig. 1-13, in

which the maximum solubility of A in the B-rich solid solution occurs at approximately $T=950$ K, illustrates that this need not be the case even for simple regular solutions.

1.5.9 Immiscibility – Monotectics

In Fig. 1-13(e), positive deviations in the liquid have given rise to a *liquid–liquid miscibility* gap. The $CaO-SiO_2$ system (Wu, 1990), shown in Fig. 1-14, exhibits such a feature. Suppose that a liquid of composition $X_{SiO_2}=0.8$ is cooled slowly from high temperatures. At $T=1815\,°C$ the miscibility gap boundary is crossed and a second liquid layer appears with a composition of $X_{SiO_2}=0.97$. As the temperature is lowered further, the composition of each liquid phase follows its respective phase boundary until, at 1692 °C, the SiO_2-rich liquid has a composition of $X_{SiO_2}=0.99$ (point B), and in the CaO-rich liquid $X_{SiO_2}=0.74$ (point A). At any temperature, the relative amounts of the two phases are given by the lever rule.

At 1692 °C the following invariant *binary monotectic reaction* occurs upon cooling:

$$\text{Liquid B} \rightarrow \text{Liquid A} + SiO_2\,(\text{solid}) \quad (1\text{-}77)$$

The temperature remains constant at 1692 °C and the compositions of the phases remain constant until all of liquid B is consumed. Cooling then continues with precipitation of solid SiO_2 with the equilibrium liquid composition following the liquidus from point A to the eutectic E.

Returning to Fig. 1-13, we see in panel (d) that the positive deviations in the liquid in this case are not large enough to produce immiscibility, but they do result in a flattening of the liquidus, which indicates a "tendency to immiscibility". If the nucleation of the solid phases can be suppressed by sufficiently rapid cooling, then a *metastable liquid–liquid miscibility gap* is observed as shown in Fig. 1-13(d). For example, in the Na_2O-SiO_2 system the flattened (or "S-shaped") SiO_2 liquidus heralds the existence of a metastable miscibility gap of importance in glass technology.

1.5.10 Intermediate Phases

The phase diagram of the Ag–Mg system (Hultgren et al., 1973) is shown in Fig. 1-15(d). An *intermetallic* phase, β', is seen centered approximately about the composition $X_{Mg}=0.5$. The Gibbs energy curve at 1050 K for such an intermetallic phase has the form shown schematically in Fig. 1-15(a). The curve $g^{\beta'}$ rises quite rapidly on either side of its minimum, which occurs near $X_{Mg}=0.5$. As a result, the β' phase appears on the phase diagram only over a limited composition range. This form of the curve $g^{\beta'}$ results from the fact that when $X_{Ag}\approx X_{Mg}$ a particularly stable crystal structure exists in which Ag and Mg atoms preferentially occupy different sites. The two common tangents P_1Q_1 and P_2Q_2 give rise to a maximum in the two-phase (β' + liquid) region of the phase diagram. (Although the maximum is observed very near $X_{Mg}=0.5$, there is no thermodynamic reason for the maximum to occur exactly at this composition.)

Another intermetallic phase, the ε phase, is also observed in the Ag–Mg system, Fig. 1-15. The phase is associated with a *peritectic* invariant ABC at 744 K. The Gibbs energy curves are shown schematically at the peritectic temperature in Fig. 1-15(c). One common tangent line can be drawn to g^{l}, $g^{\beta'}$ and g^{ε}.

Suppose that a liquid alloy of composition $X_{Mg}=0.7$ is cooled very slowly from the liquid state. At a temperature just above 744 K a liquid phase of composition C and

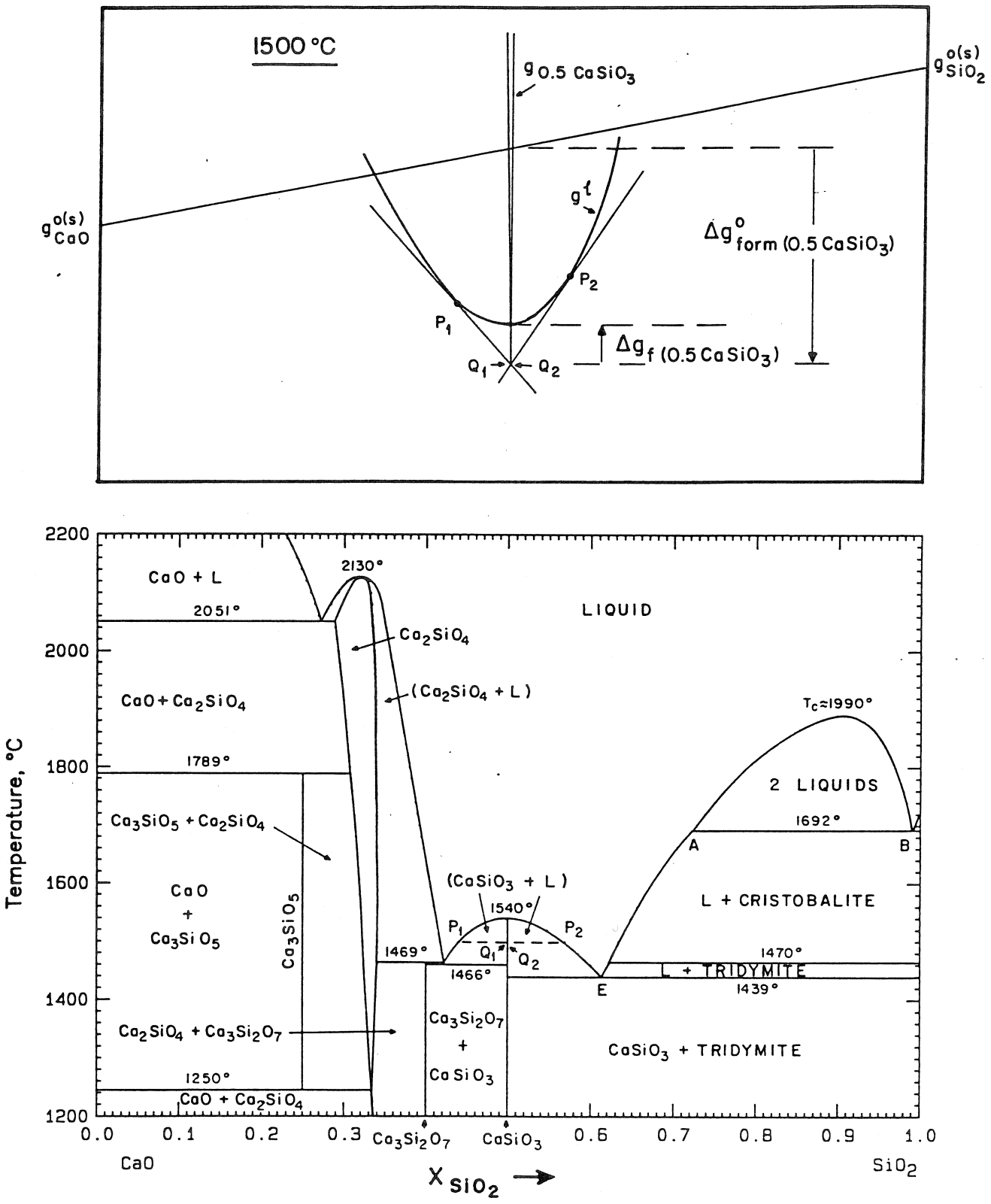

Figure 1-14. $CaO-SiO_2$ phase diagram at $P = 1$ bar (after Wu, 1990) and Gibbs energy curves at 1500 °C illustrating Gibbs energies of fusion and formation of the stoichiometric compound $CaSiO_3$.

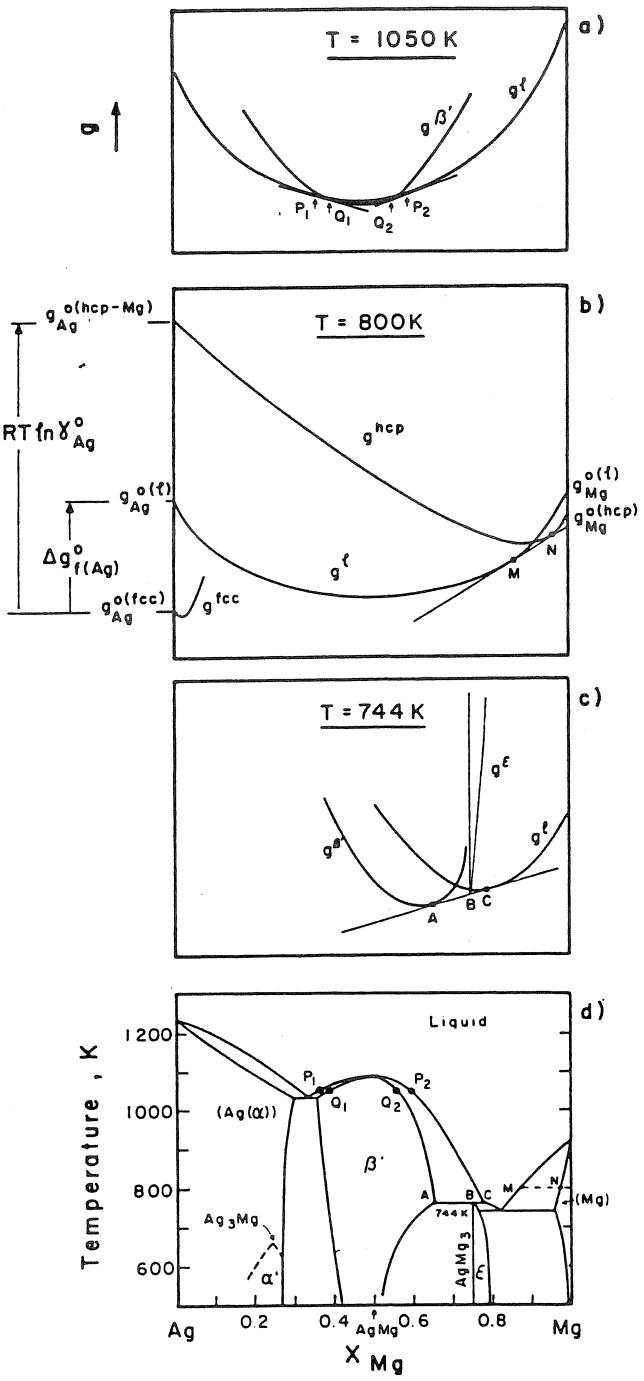

Figure 1-15. Ag–Mg phase diagram at $P = 1$ bar (after Hultgren at al., 1973) and Gibbs energy curves at three temperatures.

a β′ phase of composition A are observed at equilibrium. At a temperature just below 744 K the two phases at equilibrium are β′ of composition A and ε of composition B. The following invariant *binary peritectic reaction* thus occurs upon cooling:

$$\text{Liquid} + \beta' \text{ (solid)} \rightarrow \varepsilon \text{ (solid)} \qquad (1\text{-}78)$$

This reaction occurs isothermally at 744 K with all three phases at fixed compositions (at points A, B and C). For an alloy with overall composition between points A and B the reaction proceeds until all the liquid has been consumed. In the case of an alloy with overall composition between B and C, the β′ phase will be the first to be completely consumed.

Peritectic reactions occur upon cooling with formation of the product solid (ε in this example) on the surface of the reactant solid (β′), thereby forming a coating which can prevent further contact between the reactant solid and liquid. Further reaction may thus be greatly retarded so that equilibrium conditions can only be achieved by extremely slow cooling.

The Gibbs energy curve for the ε phase, g^{ε}, in Fig. 1-15(c) rises more rapidly on either side of its minimum than does the Gibbs energy $g^{\beta'}$ for the β′ phase in Fig. 1-15(a). As a result, the width of the single-phase region over which the ε phase exists (sometimes called its *range of stoichiometry* or *homogeneity range*) is narrower than for the β′ phase.

In the upper panel of Fig. 1-14 for the $CaO-SiO_2$ system, Gibbs energy curves at 1500 °C for the liquid and $CaSiO_3$ phases are shown schematically. $g_{0.5(CaSiO_3)}$ rises extremely rapidly on either side of its minimum. (We write $g_{0.5(CaSiO_3)}$ for 0.5 moles of the compound in order to normalize to a basis of one mole of components CaO and SiO_2.) As a result, the points of tangency Q_1 and Q_2 of the common tangents P_1Q_1 and P_2Q_2 nearly (but not exactly) coincide. Hence, the range of stoichiometry of the $CaSiO_3$ phase is very narrow (but never zero). The two-phase regions labelled ($CaSiO_3$ + liquid) in Fig. 1-14 are the two sides of a two-phase region that passes through a maximum at 1540 °C just as the (β′ + liquid) region passes through a maxi-

mum in Fig. 1-15(d). Because the $CaSiO_3$ single-phase region is so narrow, we refer to $CaSiO_3$ as a *stoichiometric compound.* Any deviation in composition from the stoichiometric 1:1 ratio of CaO to SiO_2 results in a very large increase in Gibbs energy.

The ε phase in Fig. 1-15 is based on the stiochiometry $AgMg_3$. The Gibbs energy curve, Fig. 1-15(c), rises extremely rapidly on the Ag side of the minimum, but somewhat less steeply on the Mg side. As a result, Ag is virtually insoluble in $AgMg_3$, while Mg is sparingly soluble. Such a phase with a narrow range of homogeneity is often called a *non-stoichiometric compound.* At low temperatures the β′ phase exhibits a relatively narrow range of stoichiometry about the 1:1 AgMg composition and can properly be called a compound. However, at higher temperatures it is debatable whether a phase with such a wide range of composition should be called a "compound".

From Fig. 1-14 it can be seen that if stoichiometric $CaSiO_3$ is heated it will melt isothermally at 1540 °C to form a liquid of the same composition. Such a compound is called *congruently melting* or simply a *congruent compound.* The compound Ca_2SiO_4 in Fig. 1-14 is congruently melting. The β′ phase in Fig. 1-15 is also congruently melting at the composition of the liquidus/solidus maximum.

It should be noted with regard to the congruent melting of $CaSiO_3$ in Fig. 1-14 that the limiting slopes dT/dX of both branches of the liquidus at the congruent melting point (1540 °C) are zero since we are really dealing with a maximum in a two-phase region.

The $AgMg_3$ (ε) compound in Fig. 1-15 is said to *melt incongruently.* If solid $AgMg_3$ is heated it will melt isothermally at 744 K by the reverse of the peritectic reaction, Eq. (1-78), to form a liquid of composition C and another solid phase, β′, of composition A.

Another example of an *incongruent compound* is $Ca_3Si_2O_7$ in Fig. 1-14, which melts incongruently (or peritectically) to form liquid and Ca_2SiO_4 at the peritectic temperature of 1469 °C.

An incongruent compound is always associated with a peritectic. However, the converse is not necessarily true. A peritectic is not always associated with an intermediate phase. See, for example, Fig. 1-13(i).

For purposes of phase diagram calculations involving stoichiometric compounds such as $CaSiO_3$, we may, to a good approximation, consider the Gibbs energy curve, $g_{0.5(CaSiO_3)}$, to have zero width. All that is then required is the value of $g_{0.5(CaSiO_3)}$ at the minimum. This value is usually expressed in terms of the *Gibbs energy of fusion* of the compound, $\Delta g^0_{f(0.5\,CaSiO_3)}$ or the *Gibbs energy of formation* $\Delta g^0_{form(0.5\,CaSiO_3)}$ of the compound from the pure solid components CaO and SiO_2 according to the reaction: $0.5\,CaO(sol) + 0.5\,SiO_2(sol) = 0.5\,CaSiO_3(sol)$. Both these quantities are interpreted graphically in Fig. 1-14.

1.5.11 Limited Mutual Solubility – Ideal Henrian Solutions

In Sec. 1.5.6, the region of two solids in the MgO–CaO phase diagram of Fig. 1-12 was described as a miscibility gap. That is, only one continuous g^s curve was assumed. If, somehow, the appearance of the liquid phase could be suppressed, then the two solvus lines in Fig. 1-12, when projected upwards, would meet at a critical point above which one continuous solid solution would exist at all compositions.

Such a description is justifiable only if the pure solid components have the same crystal structure, as is the case for MgO and CaO. However, consider the Ag–Mg system, Fig. 1-15, in which the terminal (Ag) solid solution is face-centered-cubic and the terminal (Mg) solid solution is hexagonal-close-packed. In this case, one continuous curve for g^s cannot be drawn. Each solid phase must have its own separate Gibbs energy curve, as shown schematically in Fig. 1-15(b) for the h.c.p. (Mg) phase at 800 K. In this figure, $g_{Mg}^{0(h.c.p.)}$ and $g_{Ag}^{0(f.c.c.)}$ are the standard molar Gibbs energies of pure h.c.p. Mg and pure f.c.c. Ag, while $g_{Ag}^{0(h.c.p.-Mg)}$ is the standard molar Gibbs energy of pure (hypothetical) h.c.p. Ag in the h.c.p. (Mg) phase.

Since the solubility of Ag in the h.c.p. (Mg) phase is limited we can, to a good approximation, describe it as a *Henrian ideal solution*. That is, when a solution is sufficiently dilute in one component, we can approximate $g_{solute}^{E} = RT \ln \gamma_{solute}$ by its value in an infinitely dilute solution. That is, if X_{solute} is small we set $\gamma_{solute} = \gamma_{solute}^{0}$ where γ_{solute}^{0} is the *Henrian activity coefficient* at $X_{solute} = 0$. Thus, for sufficiently dilute solutions we assume that γ_{solute} is independent of composition. Physically, this means that in a very dilute solution there is negligible interaction among solute particles because they are so far apart. Hence, each additional solute particle added to the solution produces the same contribution to the excess Gibbs energy of the solution and so $g^{E}_{solute} = dG^{E}/dn_{solute} = \text{constant}$.

From the Gibbs–Duhem equation, Eq. (1-56), if $dg^{E}_{solute} = 0$, then $dg^{E}_{solvent} = 0$. Hence, in a Henrian solution γ_{solute} is also constant and equal to its value in an infinitely dilute solution. That is, $\gamma_{solute} = 1$ and the solvent behaves ideally. In summary then, for dilute solutions ($X_{solvent} \approx 1$) *Henry's Law* applies:

$$\gamma_{solvent} \approx 1$$
$$\gamma_{solute} \approx \gamma_{solute}^{0} = \text{constant} \qquad (1\text{-}79)$$

(Care must be exercised for solutions other than simple substitutional solutions. Henry's Law applies only if the ideal activity is defined correctly, as will be discussed in Sec. 1.10).

Treating, then, the h.c.p. (Mg) phase in the Ag–Mg system (Fig. 1-15(b)) as a Henrian solution we write:

$$\begin{aligned} g^{h.c.p.} &= (X_{Ag}\, g_{Ag}^{0(f.c.c.)} + X_{Mg}\, g_{Mg}^{0(h.c.p.)}) \\ &\quad + RT\,(X_{Ag} \ln a_{Ag} + X_{Mg} \ln a_{Mg}) \\ &= (X_{Ag}\, g_{Ag}^{0(f.c.c.)} + X_{Mg}\, g_{Mg}^{0(h.c.p.)}) \\ &\quad + RT\,(X_{Ag} \ln (\gamma_{Ag}^{0} X_{Ag}) + X_{Mg} \ln X_{Mg}) \end{aligned} \qquad (1\text{-}80)$$

where a_{Ag} and γ_{Ag}^{0} are the activity and activity coefficient of silver with respect to pure f.c.c. silver as standard state. Let us now combine terms as follows:

$$\begin{aligned} g^{h.c.p.} &= [X_{Ag}(g_{Ag}^{0(f.c.c.)} + RT \ln \gamma_{Ag}^{0}) \\ &\quad + X_{Mg}\, g_{Mg}^{0(h.c.p.)}] \\ &\quad + RT\,(X_{Ag} \ln X_{Ag} + X_{Mg} \ln X_{Mg}) \end{aligned} \qquad (1\text{-}81)$$

Since γ_{Ag}^{0} is independent of composition, let us define:

$$g_{Ag}^{0(h.c.p.-Mg)} = (g_{Ag}^{0(f.c.c.)} + RT \ln \gamma_{Ag}^{0}) \qquad (1\text{-}82)$$

From Eqs. (1-81) and (1-82) it can be seen that, relative to $g_{Mg}^{0(h.c.p.)}$ and to the hypothetical standard state $g_{Ag}^{0(h.c.p.-Mg)}$ defined in this way, the h.c.p. solution is ideal. Eqs. (1-81) and (1-82) are illustrated in Fig. 1-15(b). It can be seen that as γ_{Ag}^{0} becomes larger, the point of tangency N moves to higher Mg concentrations. That is, as $(g_{Ag}^{0(h.c.p.-Mg)} - g_{Ag}^{0(f.c.c.)})$ becomes more positive, the solubility of Ag in h.c.p. (Mg) decreases.

It must be stressed that $g_{Ag}^{0(h.c.p.-Mg)}$ as defined by Eq. (1-82) is solvent-dependent. That is, $g_{Ag}^{0(h.c.p.-Mg)}$ is not the same as, say, $g_{Ag}^{0(h.c.p.-Cd)}$ for Ag in dilute h.c.p. (Cd) solid solutions.

Henrian activity coefficients can usually be expressed as functions of temperature:

$$RT \ln \gamma_i^0 = a - bT \tag{1-83}$$

where a and b are constants. If data are limited, it can further be assumed that $b \approx 0$ so that $RT \ln \gamma_i^0 \approx$ constant.

1.5.12 Geometry of Binary Phase Diagrams

The geometry of all types of phase diagrams of any number of components is governed by the Gibbs Phase Rule.

Consider a system with C components in which P phases are in equilibrium. The system is described by the temperature, the total pressure and the composition of each phase. In a C-component system, $(C-1)$ independent mole fractions are required to describe the composition of each phase (because $\sum X_i = 1$). Hence, the total number of variables required to describe the system is $[P(C-1)+2]$. However, as shown in Sec. 1.4.2, the chemical potential of any component is the same in all phases (α, β, γ, ...) since the phases are in equilibrium. That is:

$$\begin{aligned} & g_i^{\alpha}(T, P, X_1^{\alpha}, X_2^{\alpha}, X_3^{\alpha}, \ldots) \\ & = g_i^{\beta}(T, P, X_1^{\beta}, X_2^{\beta}, X_3^{\beta}, \ldots) \\ & = g_i^{\gamma}(T, P, X_1^{\gamma}, X_2^{\gamma}, X_3^{\gamma}, \ldots) = \ldots \end{aligned} \tag{1-84}$$

where $g_i^{\alpha}(T, P, X_1^{\alpha}, X_2^{\alpha}, X_3^{\alpha}, \ldots)$ is a function of temperature, of total pressure, and of the mole fractions X_1^{α}, X_2^{α}, X_3^{α}, ... in the α phase; and similarly for the other phases. Thus there are $C(P-1)$ independent equations in Eq. (1-84) relating the variables.

Let F be the differences between the number of variables and the number of equations relating them:

$$\begin{aligned} F &= P(C-1) + 2 - C(P-1) \\ F &= C - P + 2 \end{aligned} \tag{1-85}$$

This is the *Gibbs Phase Rule*. F is called the number of *degrees of freedom* or *variance* of the system and is the number of parameters which can and must be specified in order to completely specify the state of the system.

Binary temperature–composition phase diagrams are plotted at a fixed pressure, usually 1 bar. This then eliminates one degree of freedom. In a binary system, $C=2$. Hence, for binary isobaric $T-X$ diagrams the phase rule reduces to:

$$F = 3 - P \tag{1-86}$$

Binary $T-X$ diagrams contain single-phase areas and two-phase areas. In the single-phase areas, $F = 3-1 = 2$. That is, temperature and composition can be specified independently. These regions are thus called *bivariant*. In two-phase regions, $F = 3-2 = 1$. If, say, T is specified, then the compositions of both phases are determined by the ends of the tie-lines. Two-phase regions are thus termed *univariant*. Note that the overall composition can be varied within a two-phase region at constant T, but the overall composition is not a parameter in the sense of the phase rule. Rather, it is the compositions of the individual phases at equilibrium that are the parameters to be considered in counting the number of degrees of freedom.

When three phases are at equilibrium in a binary system at constant pressure, $F = 3-3 = 0$. Hence, the compositions of all three phases, as well as T, are fixed. There are two general types of three-phase *invariants* in binary phase diagrams. These are the *eutectic-type* and *peritectic-type* invariants as illustrated in Fig. 1-16. Let the three phases concerned be called α, β and γ, with β as the central phase as shown in Fig. 1-16. The phases α, β and γ can be solid, liquid or gaseous. At the eutectic-type invariant, the following invariant re-

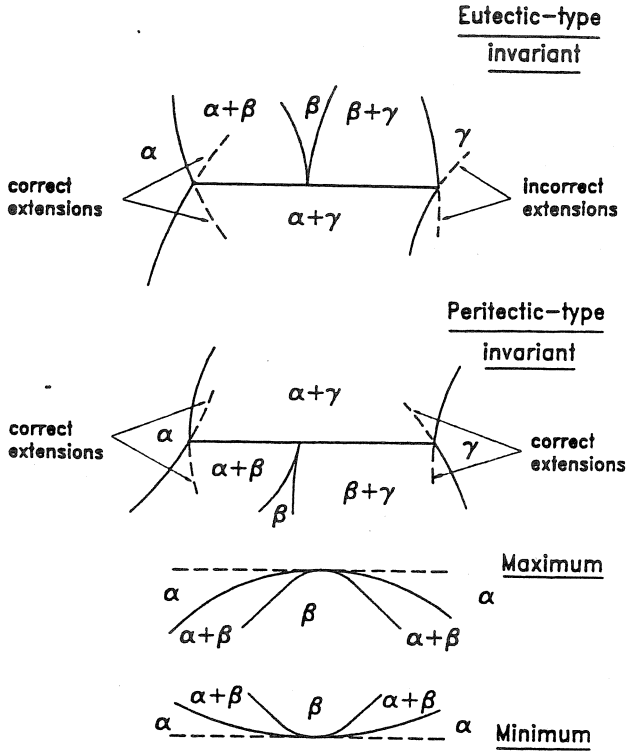

Figure 1-16. Some geometrical units of binary phase diagrams, illustrating rules of construction.

action occurs isothermally as the system is cooled:

$$\beta \rightarrow \alpha + \gamma \qquad (1\text{-}87)$$

whereas at the peritectic-type invariant the invariant reaction upon cooling is:

$$\alpha + \gamma \rightarrow \beta \qquad (1\text{-}88)$$

Some examples of eutectic-type invariants are: (i) *eutectics* (Fig. 1-12) in which $\alpha = \text{solid}_1$, $\beta = \text{liquid}$, $\gamma = \text{solid}_2$; the eutectic reaction is $l \rightarrow s_1 + s_2$; (ii) *monotectics* (Fig. 1-14) in which $\alpha = \text{liquid}_1$, $\beta = \text{liquid}_2$, $\gamma =$ solid; the monotectic reaction is $l_2 \rightarrow l_1 + s$; (iii) *eutectoids* in which $\alpha = \text{solid}_1$, $\beta = \text{solid}_2$, $\gamma = \text{solid}_3$; the eutectoid reaction is $s_2 \rightarrow s_1 + s_3$; (iv) *catatectics* in which $\alpha = \text{liquid}$, $\beta = \text{solid}_1$, $\gamma = \text{solid}_2$; the catatectic reaction is $s_1 \rightarrow l + s_2$.

Some examples of peritectic-type invariants are: (i) *peritectics* (Fig. 1-15) in which $\alpha = \text{liquid}$, $\beta = \text{solid}_1$, $\gamma = \text{solid}_2$. The peritectic reaction is $l + s_2 \rightarrow s_1$; (ii) *syntectics* (Fig. 1-13(k)) in which $\alpha = \text{liquid}_1$, $\beta =$ solid, $\gamma = \text{liquid}_2$. The syntectic reaction is $l_1 + l_2 \rightarrow s$; (iii) *peritectoids* in which $\alpha = \text{solid}_1$, $\beta = \text{solid}_2$, $\gamma = \text{solid}_3$. The peritectoid reaction is $s_1 + s_3 \rightarrow s_2$.

An important rule of construction which applies to invariants in binary phase diagrams is illustrated in Fig. 1-16. This *extension rule* states that at an invariant the extension of a boundary of a two-phase region must pass into the adjacent two-phase region and not into a single-phase region. Examples of both correct and incorrect constructions are given in Fig. 1-16. To understand why the "incorrect extensions" shown are not right consider that the $(\alpha + \gamma)$ phase boundary line indicates the composition of the γ-phase in equilibrium with the α-phase, as determined by the common tangent to the Gibbs energy curves. Since there is no reason for the Gibbs energy curves or their derivatives to change discontinuously at the invariant temperature, the extension of the $(\alpha + \gamma)$ phase boundary also represents the stable phase boundary under equilibrium conditions. Hence, for this line to extend into a region labeled as single-phase γ is incorrect.

Two-phase regions in binary phase diagrams can terminate: (i) on the pure component axes (at $X_A = 1$ or $X_B = 1$) at a transformation point of pure A or B; (ii) at a critical point of a miscibility gap; (iii) at an invariant. Two-phase regions can also exhibit maxima or minima. In this case, both phase boundaries must pass through their maximum or minimum at the same point as shown in Fig. 1-16.

All the *geometrical units* of construction of binary phase diagrams have now been discussed. The phase diagram of a binary alloy system will usually exhibit several of these units. As an example, the Fe–Mo phase diagram (Kubaschewski, 1982) is

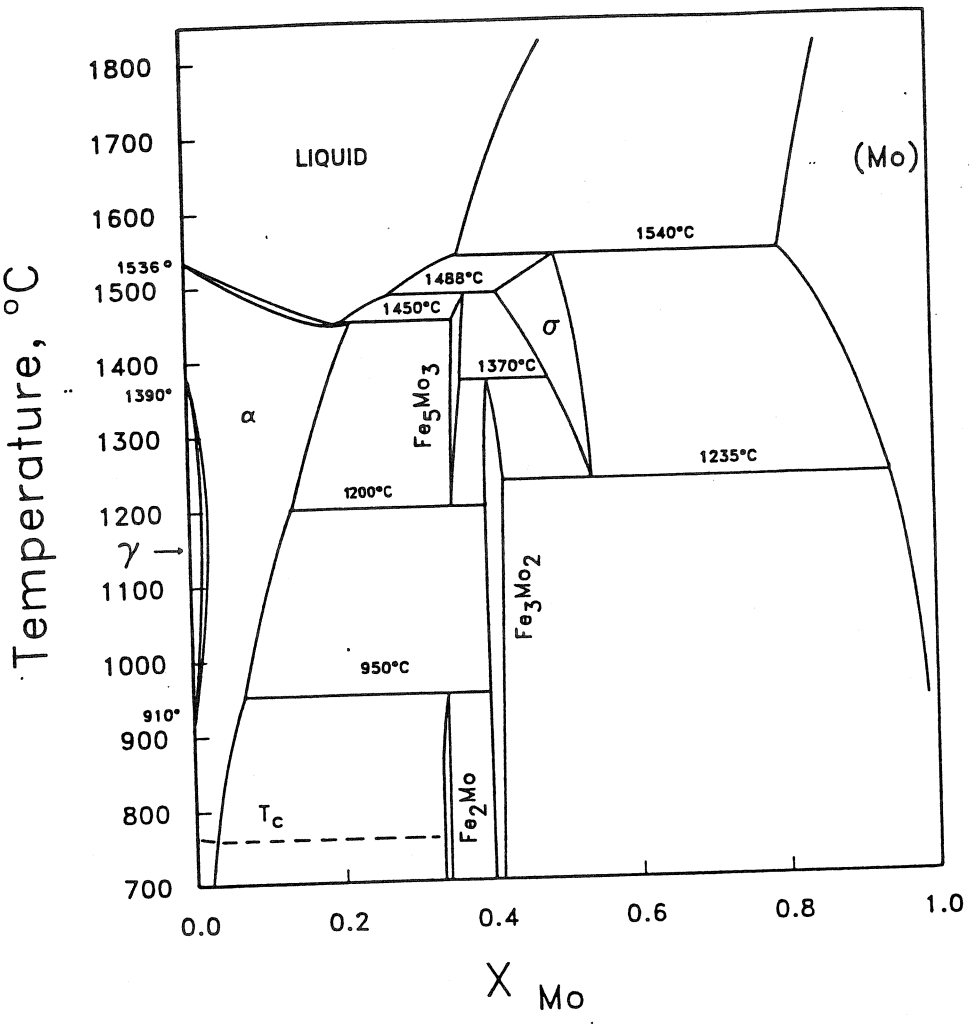

Figure 1-17. Fe–Mo phase diagram at $P = 1$ bar (Kubaschewski, 1982).

shown in Fig. 1-17. The invariants in this system are peritectics at 1540, 1488 and 1450 °C; eutectoids at 1235 and 1200 °C; peritectoids at 1370 and 950 °C. The two-phase (liquid + γ) region passes through a minimum at $X_{Mo} = 0.2$.

Between 910 °C and 1390 °C is a two-phase (α + γ) γ-*loop*. Pure Fe adopts the f.c.c. γ structure between these two temperatures but exists as the b.c.c. α phase at higher and lower temperatures. Mo, however, is more soluble in the b.c.c. than in the f.c.c. structure. That is, $g_{Mo}^{0(b.c.c.-Fe)} < g_{Mo}^{0(f.c.c.-Fe)}$ as discussed in Sec. 1.5.11. Therefore, small additions of Mo stabilize the b.c.c. structure.

In the $CaO-SiO_2$ phase diagram, Fig. 1-14, we observe eutectics at 1439, 1466 and 2051 °C; a monotectic at 1692 °C; and a peritectic at 1469 °C. The compound Ca_3SiO_5 dissociates upon heating to CaO and Ca_2SiO_4 by a peritectoid reaction at 1789 °C and dissociates upon cooling to CaO and Ca_2SiO_4 by a eutectoid reaction at 1250 °C. Maxima are observed at 2130 and 1540 °C. At 1470 °C there is an invariant associated with the tridymite → cristobalite transition of SiO_2. This is either a peritectic or a catatectic depending upon the relative solubility of CaO in tridymite and cristobalite. However, these solubilities are very small and unknown.

1.6 Application of Thermodynamics to Phase Diagram Analysis

1.6.1 Thermodynamic/Phase Diagram Optimization

In recent years the development of solution models, numerical methods and computer software has permitted a quantitative application of thermodynamics to phase diagram analysis. For a great many systems it is now possible to perform a simultaneous critical evaluation of available phase diagram measurements and of available thermodynamic data (calorimetric data, measurements of activities, etc.) with a view to obtaining optimized equations for the Gibbs energies of each phase which best represent all the data. These equations are consistent with thermodynamic principles and with theories of solution behavior.

The phase diagram can be calculated from these thermodynamic equations, and so one set of self-consistent equations describes all the thermodynamic properties and the phase diagram. This technique of analysis greatly reduces the amount of experimental data needed to fully characterize a system. All data can be tested for internal consistency. The data can be interpolated and extrapolated more accurately and metastable phase boundaries can be calculated. All the thermodynamic properties and the phase diagram can be represented and stored by means of a small set of coefficients.

Finally, and most importantly, it is often possible to estimate the thermodynamic properties and phase diagrams of ternary and higher-order systems from the assessed parameters for their binary sub-systems, as will be discussed in Sec. 1.11. The analysis of binary systems is thus the first and most important step in the development of databases for multicomponent systems.

1.6.2 Polynomial Representation of Excess Properties

Empirical equations are required to express the excess thermodynamic properties of the solution phases as functions of composition and temperature. For many simple binary substitutional solutions, a good representation is obtained by expanding the excess enthalpy and entropy as polynomials in the mole fractions X_A and X_B of the components:

$$h^E = X_A X_B [h_0 + h_1(X_B - X_A) + h_2(X_B - X_A)^2 + h_3(X_B - X_A)^3 + \ldots] \quad (1\text{-}89)$$

$$s^E = X_A X_B [s_0 + s_1(X_B - X_A) + s_2(X_B - X_A)^2 + s_3(X_B - X_A)^3 + \ldots] \quad (1\text{-}90)$$

where the h_i and s_i are empirical coefficients. As many coefficients are used as are required to represent the data in a given system. For most systems it is a good approximation to assume that the coefficients h_i and s_i are independent of temperature.

If the series are truncated after the first term, then:

$$g^E = h^E - Ts^E = X_A X_B (h_0 - Ts_0) \quad (1\text{-}91)$$

This is the equation for a regular solution discussed in Sec. 1.5.7. Hence, the polynomial representation can be considered to be an extension of regular solution theory. When the expansions are written in terms of the composition variable $(X_B - X_A)$, as in Eqs. (1-89) and (1-90), they are said to be in *Redlich–Kister form*. Other equivalent polynomial expansions such as orthogonal Legendre series have been discussed by Pelton and Bale (1986).

Differentiation of Eqs. (1-89) and (1-90) and substitution into Eq. (1-55) yields the

following expansions for the partial excess enthalpies and entropies:

$$h_A^E = X_B^2 \sum_{i=0} h_i[(X_B - X_A)^i - 2i\,X_A(X_B - X_A)^{i-1}] \quad (1\text{-}92)$$

$$h_B^E = X_A^2 \sum_{i=0} h_i[(X_B - X_A)^i + 2i\,X_B(X_B - X_A)^{i-1}] \quad (1\text{-}93)$$

$$s_A^E = X_B^2 \sum_{i=0} s_i[(X_B - X_A)^i - 2i\,X_A(X_B - X_A)^{i-1}] \quad (1\text{-}94)$$

$$s_B^E = X_A^2 \sum_{i=0} s_i[(X_B - X_A)^i + 2i\,X_B(X_B - X_A)^{i-1}] \quad (1\text{-}95)$$

Partial excess Gibbs energies, g_i^E, are then given by Eq. (1-52).

Eqs. (1-89) and (1-90), being based upon regular solution theory, give an adequate representation for most simple substitutional solutions in which deviations from ideal behavior are not too great. In other cases, more sophisticated models are required, as discussed in Sec. 1.10.

1.6.3 Least-Squares Optimization

Eqs. (1-89), (1-90) and (1-92) to (1-95) are linear in terms of the coefficients. Through the use of these equations, all integral and partial excess properties (g^E, h^E, s^E, g_i^E, h_i^E, s_i^E) can be expressed by linear equations in terms of the one set of coefficients $\{h_i, s_i\}$. It is thus possible to include all available experimental data for a binary phase in one simultaneous linear least-squares optimization. Details have been discussed by Bale and Pelton (1983), Lukas et al. (1977) and Dörner et al. (1980).

The technique of coupled thermodynamic/phase diagram analysis is best illustrated by examples.

The phase diagram of the LiF–NaF system is shown in Fig. 1-18. Data points measured by Holm (1965) are shown on the diagram. The Gibbs energy of fusion of each pure component at temperature T is given by:

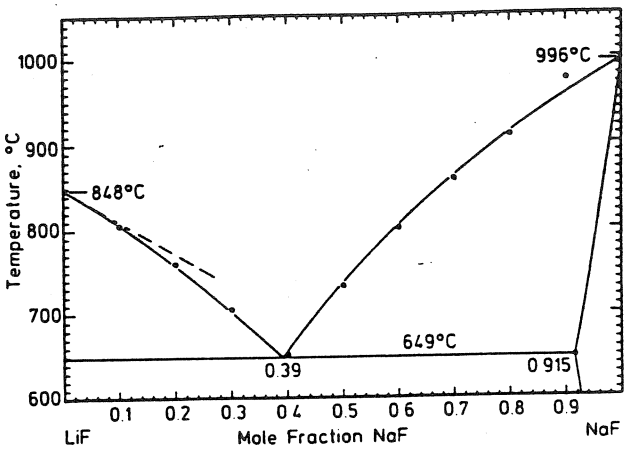

Figure 1-18. LiF–NaF phase diagram at $P = 1$ bar calculated from optimized thermodynamic parameters (Sangster and Pelton, 1987). Points are experimental from Holm (1965). Dashed line is theoretical limiting liquidus slope for negligible solid solubility.

$$\Delta g_f^0 = \Delta h_{f(T_f)}^0 (1 - T/T_f) + \int_{T_f}^{T} (c_p^l - c_p^s)(1 - 1/T)\,dT \quad (1\text{-}96)$$

where $\Delta h_{f(T_f)}^0$ is the enthalpy of fusion at the melting point T_f, and c_p^l and c_p^s are the heat capacities of the pure liquid and solid. The following values are taken from Barin et al. (1977):

$$\Delta g_{f(LiF)}^0 = 14.518 + 128.435\,T + 8.709 \times 10^{-3} T^2 - 21.494\,T \ln T - 2.65 \times 10^5 T^{-1} \quad \text{J/mol} \quad (1\text{-}97)$$

$$\Delta g_{f(NaF)}^0 = 10.847 + 156.584\,T + 4.950 \times 10^{-3} T^2 - 23.978\,T \ln T - 1.07 \times 10^5 T^{-1} \quad \text{J/mol} \quad (1\text{-}98)$$

Thermodynamic properties along the liquidus and solidus are related by equations like Eqs. (1-64) and (1-65). Taking the ideal activities to be equal to the mole fractions:

$$R\,T \ln X_i^l - R\,T \ln X_i^s + g_i^{E(l)} - g_i^{E(s)} = -\Delta g_{f(i)}^0 \quad (1\text{-}99)$$

where i=LiF or NaF. Along the LiF-rich liquidus, the liquid is in equilibrium with essentially pure solid LiF. Hence, $X^{s}_{LiF}=1$ and $g^{E(s)}_{Lif}=0$. Eq. (1-99) then reduces to:

$$RT \ln X^{l}_{LiF} + g^{E(l)}_{Lif} = -\Delta g^{0}_{f(LiF)} \qquad (1\text{-}100)$$

From experimental values of X^{l}_{LiF} on the liquidus and with Eq. (1-97) for $\Delta g^{0}_{f(LiF)}$, values of $g^{E(l)}_{Lif}$ at the measured liquidus points can be calculated from Eq. (1-100).

Along the NaF-rich solidus the solid solution is sufficiently concentrated in NaF that Henrian behavior (Sec. 1.5.11) can be assumed. That is, for the solvent, $g^{E(s)}_{NaF}=0$. Hence, Eq. (1-99) becomes:

$$RT \ln X^{(l)}_{NaF} - RT \ln X^{(s)}_{NaF} + g^{E(l)}_{NaF} = -\Delta g^{0}_{f(NaF)} \qquad (1\text{-}101)$$

Thus, from the experimental liquidus and solidus compositions and with the Gibbs energy of fusion from Eq. (1-98), values of $g^{E(l)}_{NaF}$ can be calculated at the measured liquidus points from Eq. (1-101).

Finally, enthalpies of mixing, h^{E}, in the liquid have been measured by calorimetry by Hong and Kleppa (1976).

Combining all these data in a least-squares optimization, the following expressions for the liquid were obtained by Sangster and Pelton (1987):

$$h^{E(l)} = X_{LiF} X_{NaF} \times [-7381 + 184 (X_{NaF} - X_{LiF})] \text{ J/mol} \qquad (1\text{-}102)$$

$$s^{E(l)} = X_{LiF} X_{NaF} \times [-2.169 - 0.562 (X_{NaF} - X_{LiF})] \text{ J/mol} \qquad (1\text{-}103)$$

Eqs. (1-102) and (1-103) then permit all other integral and partial properties of the liquid to be calculated.

For the NaF-rich Henrian solid solution, the solubility of LiF has been measured by Holm (1965) at the eutectic temperature where the NaF-rich solid solution is in equilibrium with pure solid LiF. That is, $a_{LiF}=1$ with respect to pure solid LiF as standard state. In the Henrian solution at saturation,

$$a_{LiF} = \gamma^{0}_{LiF} X_{LiF} = \gamma^{0}_{LiF}(1 - 0.915) = 1$$

Hence, the Henrian activity coefficient in the NaF-rich solid solution at 649 °C is $\gamma^{0}_{LiF}=11.76$. Since no solubilities have been measured at other temperatures, we assume that:

$$RT \ln \gamma^{0}_{LiF} = R(922) \ln(11.76) = 18\,900 \text{ J/mol} = \text{constant} \qquad (1\text{-}104)$$

Using the notation of Eq. (1-82):

$$g^{0(s,\,NaF)}_{LiF} = g^{0(s)}_{LiF} + 18\,900 \text{ J/mol} \qquad (1\text{-}105)$$

where $g^{0(s)}_{LiF}$ is the standard Gibbs energy of solid LiF, and $g^{0(s,\,NaF)}_{LiF}$ is the hypothetical standard Gibbs energy of LiF dissolved in solid NaF.

The phase diagram drawn in Fig. 1-18 was calculated from Eqs. (1-97) to (1-104). Complete details of the analysis of the LiF–NaF system are given by Sangster and Pelton (1987).

As a second example of thermodynamic/phase diagram optimization, consider the Cd–Na system. The phase diagram, with points measured by several authors (Mathewson, 1906; Kurnakow and Kusnetzow, 1907; Weeks and Davies, 1964) is shown in Fig. 1-19.

From electromotive force measurements on alloy concentration cells, several authors have measured the activity coefficient of Na in liquid alloys. The data are shown in Fig. 1-20 at 400 °C. From the temperature dependence of $g^{E}_{Na} = RT \ln \gamma_{Na}$, the partial enthalpy of Na in the liquid was obtained via Eq. (1-52). The results are shown in Fig. 1-21. Also, h^{E} of the liquid has been measured by Kleinstuber (1961) by direct calorimetry. These thermodynamic data for g^{E}_{Na}, h^{E}_{Na} and h^{E} were

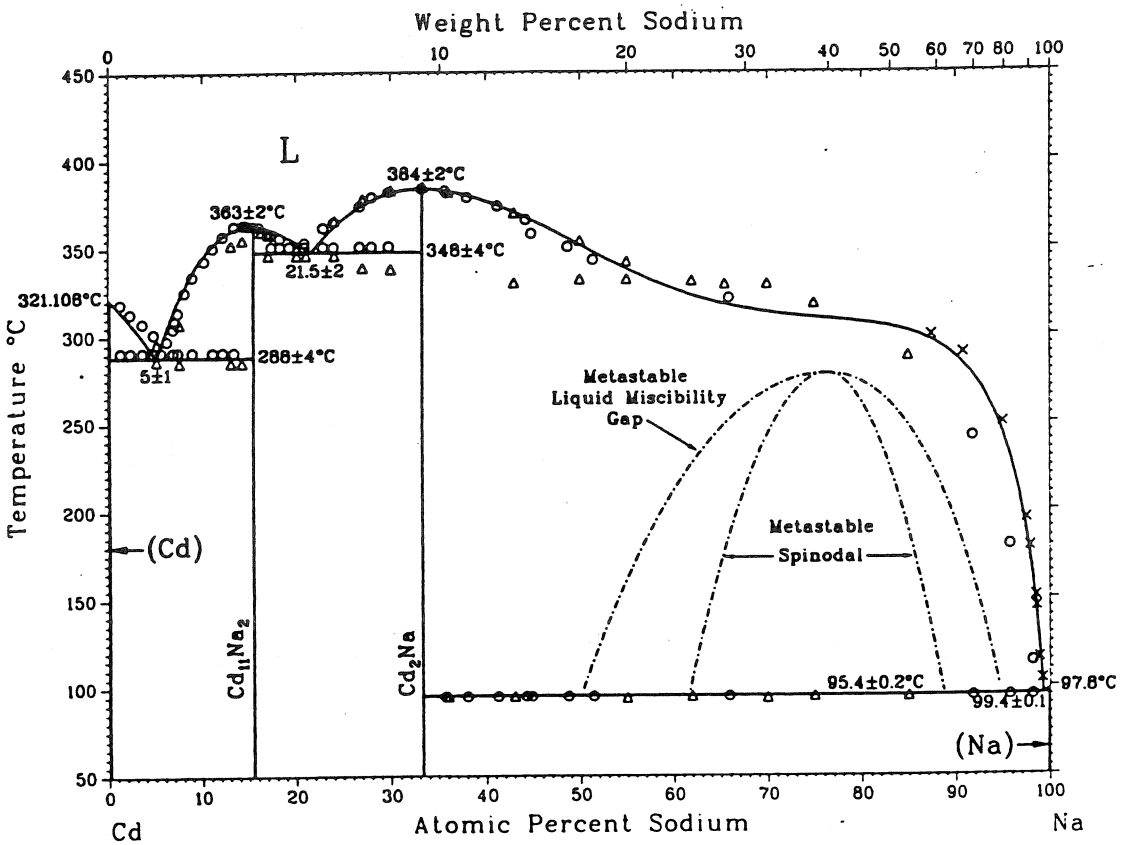

Figure 1-19. Cd–Na phase diagram at $P=1$ bar calculated from optimized thermodynamic parameters (Reprinted from Pelton, 1988a). ○ Kurnakow and Kusnetzow (1907), △ Mathewson (1906), × Weeks and Davies (1964).

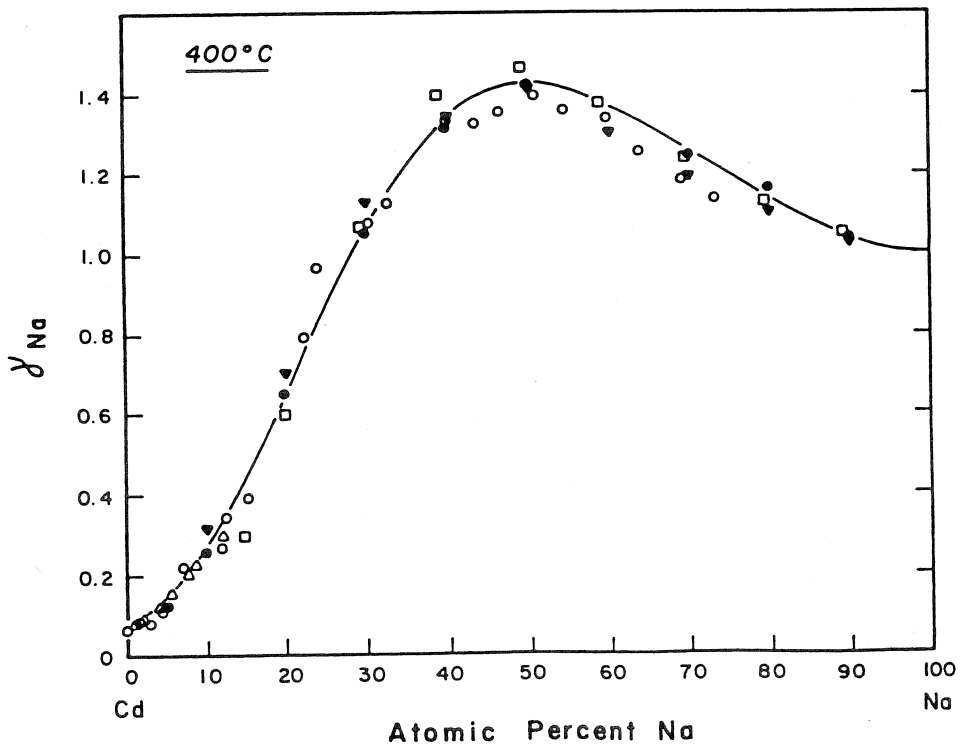

Figure 1-20. Sodium activity coefficient in liquid Cd–Na alloys at 400°C. Line is calculated from optimized thermodynamic parameters (Reprinted from Pelton, 1988a).
□ Hauffe (1940),
● Lantratov and Mikhailova (1971),
△ Maiorova et al. (1976),
▼ Alabyshev and Morachevskii (1957),
○ Bartlett et al. (1970).

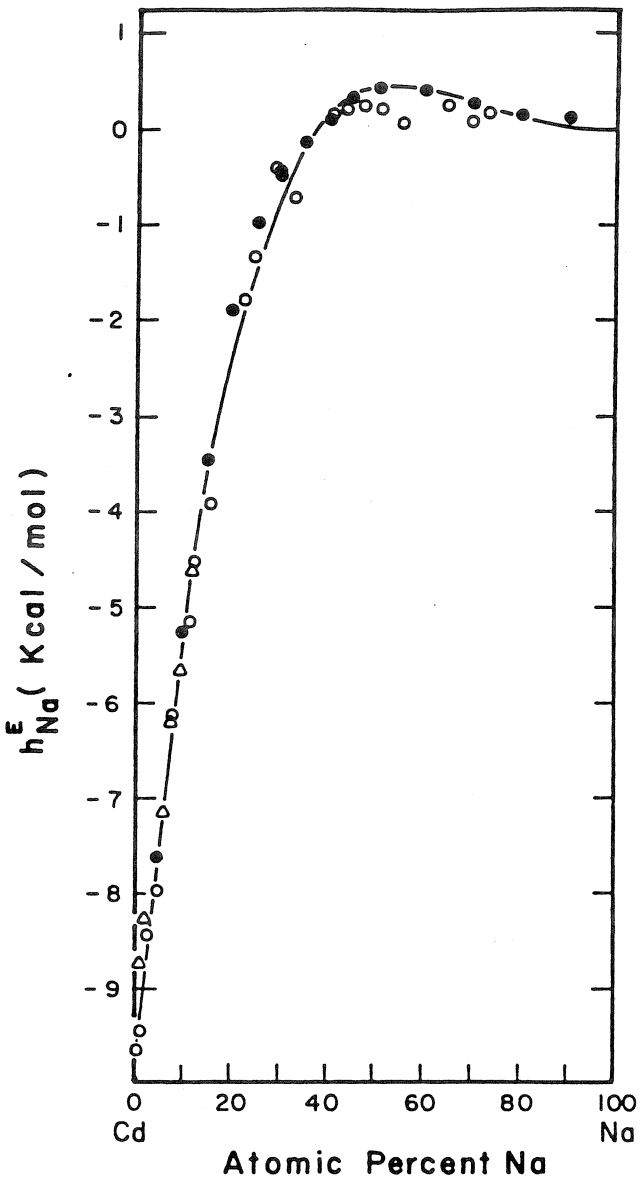

Figure 1-21. Partial excess enthalpy of sodium in liquid Cd–Na alloys. Line is calculated from optimized thermodynamic parameters (Reprinted from Pelton, 1988a). ● Lantratov and Mikhailova (1971), △ Maiorova et al. (1976), ○ Bartlett et al. (1970).

optimized simultaneously (Pelton, 1988a) to obtain the following expressions for h^E and s^E of the liquid:

$$h^{E(l)} = X_{Cd}\,X_{Na}[-12\,508 + 20\,316 \times (X_{Na} - X_{Cd}) - 8714\,(X_{Na} - X_{Cd})^2]\ \text{J/mol} \quad (1\text{-}106)$$

$$s^{E(l)} = X_{Cd}\,X_{Na}[-15.452 + 15.186 \times (X_{Na} - X_{Cd}) - 10.062\,(X_{Na} - X_{Cd})^2 - 1.122\,(X_{Na} - X_{Cd})^3]\ \text{J/mol K} \quad (1\text{-}107)$$

Eq. (1-106) reproduces the calorimetric data within 200 J/mol^{-1}. Eqs. (1-52), (1-58), (1-93) and (1-95) can be used to calculate h^E_{Na} and γ_{Na}. The calculated curves are compared to the measured points in Figs. 1-20 and 1-21.

For the two compounds, Gibbs energies of fusion were calculated (Pelton, 1988a) so as to best reproduce the measured phase diagram:

$$\Delta g^0_{f(1/13\,Cd_{11}Na_2)} = 6816 - 10.724\,T\ \text{J/g-atom} \quad (1\text{-}108)$$

$$\Delta g^0_{f(1/3\,Cd_2Na)} = 8368 - 12.737\,T\ \text{J/g-atom} \quad (1\text{-}109)$$

The optimized enthalpies of fusion of 6816 and 8368 J/g-atom agree within error limits with the values of 6987 and 7878 J/g-atom measured by Roos (1916). (See Fig. 1-14 for an illustration of the relation between the Gibbs energy of fusion of a compound and the phase diagram.)

The phase diagram shown in Fig. 1-19 was calculated from Eqs. (1-106) to (1-109) along with the Gibbs energies of fusion of Cd and Na taken from the literature (Chase, 1983). Complete details of the analysis of the Cd–Na system are given by Pelton (1988a).

It can thus be seen that one simple set of equations can simultaneously and self-consistently describe all the thermodynamic properties and the phase diagram of a binary system.

The exact optimization procedure will vary from system to system depending upon the type and accuracy of the available data, the number of phases present, the extent of solid solubility, etc. A large number of optimizations have been published in the *Calphad Journal* (Pergamon) since 1977.

1.6.4 Calculation of Metastable Phase Boundaries

In the Cd–Na system just discussed, the liquid exhibits positive deviations from ideal mixing. That is, $g^{E(l)} > 0$. This fact is reflected in the very flat liquidus in Fig. 1-19 as was discussed in Sec. 1.5.9.

By simply not including any solid phases in the calculation, the metastable liquid miscibility gap as well as the spinodal curve (Sec. 1.5.5) can be calculated as shown in Fig. 1-19. These curves are important in the formation of metallic glasses by rapid quenching.

Other metastable phase boundaries such as the extension of a liquidus curve below a eutectic can also be calculated thermodynamically by simply excluding one or more phases during the computations.

1.7 Ternary and Multicomponent Phase Diagrams

This section provides an introduction to ternary phase diagrams. For a more detailed treatment, see Prince (1966); Ricci (1964); Findlay (1951); or West (1965).

1.7.1 The Ternary Composition Triangle

In a ternary system with components A–B–C, the sum of the mole fractions is unity, $(X_A + X_B + X_C) = 1$. Hence, there are two independent composition variables. A representation of composition, symmetrical with respect to all three components, may be obtained with the equilateral "composition triangle" as shown in Fig. 1-22 for the Bi–Sn–Cd system. Compositions at the corners of the triangle correspond to the pure components. Along the edges of the triangle compositions corresponding to the three binary subsystems Bi–Sn, Sn–Cd and Cd–Bi are found. Lines of constant mole fraction X_{Bi} are parallel to the Sn–Cd edge, while lines of constant X_{Sn} and X_{Cd} are parallel to the Cd–Bi and Bi–Sn edges respectively. For example, at point *a* in Fig. 1-22, $X_{Bi} = 0.05$, $X_{Sn} = 0.45$ and $X_{Cd} = 0.50$.

Similar equilateral composition triangles can be drawn with coordinates in terms of wt.% of the three components.

1.7.2 Ternary Space Model

A ternary temperature–composition "phase diagram" at constant total pressure may be plotted as a three-dimensional "space model" within a right triangular prism with the equilateral composition triangle as base and temperature as vertical axis. Such a space model for a simple eutectic ternary system A–B–C is illustrated in Fig. 1-23. On the three vertical faces of the prism we find the phase diagrams of the three binary subsystems, A–B, B–C and C–A which, in this example, are all simple eutectic binary systems. The binary eutectic points are e_1, e_2 and e_3. Within the prism we see three *liquidus surfaces* descending from the melting points of pure A, B and C. Compositions on these surfaces correspond to compositions of liquid in equilibrium with A-, B- and C-rich solid phases.

In a ternary system at constant pressure, the Gibbs phase rule, Eq. (1-85), becomes:

$$F = 4 - P \qquad (1\text{-}110)$$

When the liquid and one solid phase are in equilibrium $P = 2$. Hence $F = 2$ and the system is bivariant. A ternary liquidus is thus a two-dimensional surface. We may choose two variables, say T and one composition coordinate of the liquid, but then the other liquid composition coordinate and the composition of the solid are fixed.

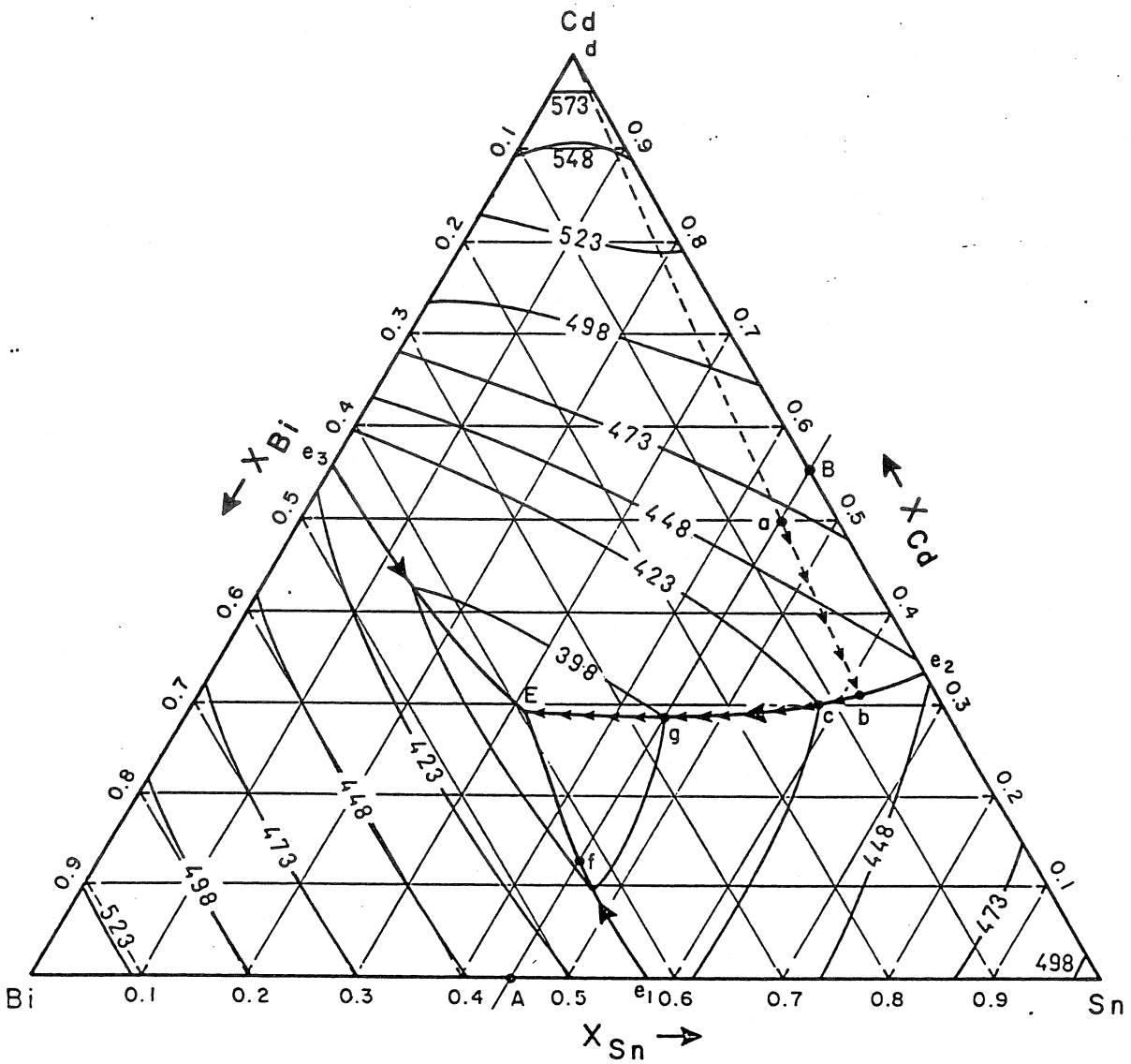

Figure 1-22. Projection of the liquidus surface of the Bi–Sn–Cd system onto the ternary composition triangle (after Bray et al., 1961–1962). Small arrows show the crystallization path of an alloy of overall composition at point *a*. (Reprinted from Pelton, 1996.)

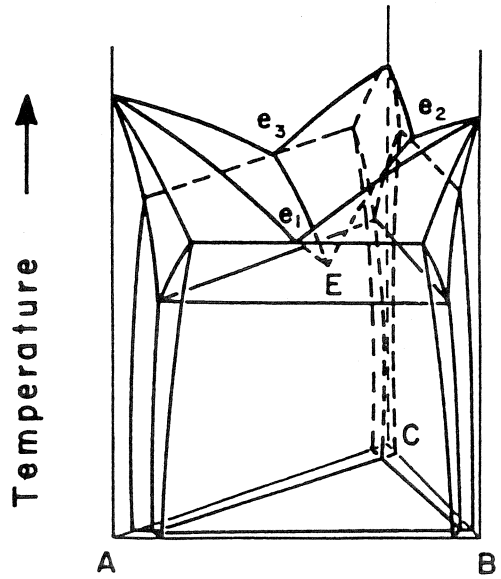

Figure 1-23. Perspective view of ternary space model of a simple eutectic ternary system. e_1, e_2, e_3 are the binary eutectics and E is the ternary eutectic. The base of the prism is the equilateral composition triangle. (Reprinted from Pelton, 1983.)

The A- and B-liquidus surfaces in Fig. 1-23 intersect along the line e_1E. Liquids with compositions along this line are therefore in equilibrium with A-rich and B-rich solid phases simultaneously. That is, $P=3$ and so $F-1$. Such "valleys" are thus called *univariant lines*. The three univariant lines meet at the *ternary eutectic point* E at which $P=4$ and $F=0$. This is an invariant point since the temperature and the compositions of all four phases in equilibrium are fixed.

1.7.3 Polythermal Projections of Liquidus Surfaces

A two-dimensional representation of the ternary liquidus surface may be obtained as an orthogonal projection upon the base composition triangle. Such a *polythermal projection* of the liquidus of the Bi–Sn–Cd system (Bray et al., 1961–62) is shown in Fig. 1-22. This is a simple eutectic ternary system with a space model like that shown in Fig. 1-23. The constant temperature lines on Fig. 1-22 are called *liquidus isotherms*. The univariant valleys are shown as heavier lines. By convention, the large arrows indicate the directions of decreasing temperature along these lines.

Let us consider the sequence of events occurring during the equilibrium cooling from the liquid of an alloy of overall composition a in Fig. 1-22. Point a lies within the field of *primary crystallization* of Cd. That is, it lies within the composition region in Fig. 1-22 in which Cd-rich solid will be the first solid to precipitate upon cooling. As the liquid alloy is cooled, the Cd-liquidus surface is reached at $T\approx 465$ K (slightly below the 473 K isotherm). A solid Cd-rich phase begins to precipitate at this temperature. Now, in this particular system, Bi and Sn are nearly insoluble in solid Cd, so that the solid phase is virtually pure Cd. (Note that this fact cannot be deduced from Fig. 1-22 alone.) Therefore, as solidification proceeds, the liquid becomes depleted in Cd, but the ratio X_{Sn}/X_{Bi} in the liquid remains constant. Hence, the composition path followed by the liquid (its *crystallization path*) is a straight line passing through point a and projecting to the Cd-corner of the triangle. This crystallization path is shown on Fig. 1-22 as the line ab.

In the general case in which a solid solution rather than a pure component or stoichiometric compound is precipitating, the crystallization path will not be a straight line. However, for equilibrium cooling, a straight line joining a point on the crystallization path at any T to the overall composition point a will extend through the composition, on the solidus surface, of the solid phase in equilibrium with the liquid at that temperature.

When the composition of the liquid has reached point b in Fig. 1-22 at $T\approx 435$ K, the relative proportions of the solid Cd and liquid phases at equilibrium are given by the *lever rule* applied to the *tie-line* dab: (moles of liquid)/(moles of Cd) = da/ab. Upon further cooling, the liquid composition follows the univariant valley from b to E while Cd and Sn-rich solids coprecipitate as a binary eutectic mixture. When the liquidus composition attains the ternary eutectic composition E at $T\approx 380$ K the invariant *ternary eutectic reaction* occurs:

$$\text{liquid} \rightarrow s_1 + s_2 + s_3 \qquad (1\text{-}111)$$

where s_1, s_2 and s_3 are the three solid phases and where the compositions of all four phases (as well as T) remain fixed until all liquid is solidified.

In order to illustrate several of the features of polythermal projections of liquidus surfaces, a projection of the liquidus of a hypothetical system A–B–C is shown in Fig. 1-24. For the sake of simplicity, iso-

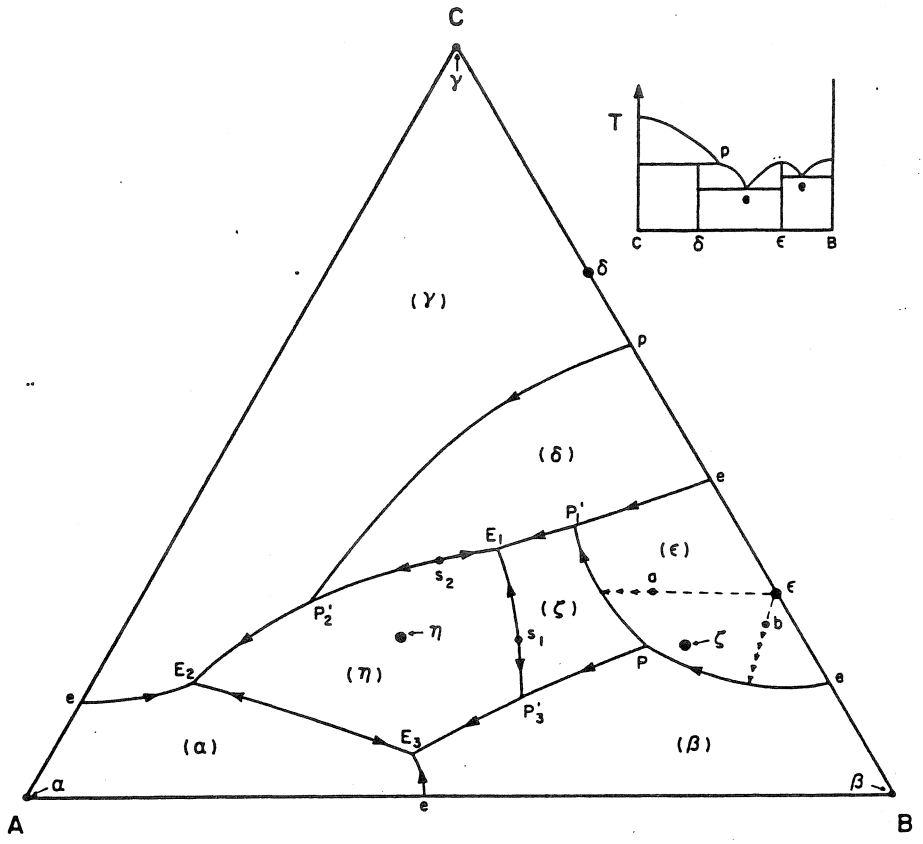

Figure 1-24. Projection of the liquidus surface of a system A–B–C. The binary subsystems A–B and C–A are simple eutectic systems. The binary phase diagram B–C is shown in the insert. All solid phases are assumed pure stoichiometric components or compounds. Small arrows show crystallization paths of alloys of compositions at points *a* and *b*. (Reprinted from Pelton, 1983.)

therms are not shown, only the univariant lines with arrows to show the directions of decreasing temperature. The binary subsystems A–B and C–A are simple eutectic systems, while the binary subsystem B–C contains one congruent binary phase, ε, and one incongruent binary phase, δ, as shown in the insert in Fig. 1-24. The letters *e* and *p* indicate binary eutectic and peritectic points. The ε and δ phases are called *binary compounds* since they have compositions within a binary subsystem. Two *ternary compounds*, η and ζ, with compositions within the ternary triangle, as indicated in Fig. 1-24, are also found in this system. All compounds, as well as pure solid A, B and C (the "α, β and γ" phases), are assumed to be stoichiometric (i.e., there is no solid solubility). The fields of primary crystallization of all the solids are indicated in parentheses in Fig. 1-24. The composition of the ε phase lies within its field, since ε is a congruent compound, while the composition of the δ phase lies outside of its field since δ is incongruent. Similarly for the ternary compounds, η is a congruently melting compound while ζ is incongruent. For the congruent compound η, the highest temperature on the η liquidus occurs at the composition of η.

The univariant lines meet at a number of *ternary eutectics E* (three arrows converging), a *ternary peritectic P* (one arrow entering, two arrows leaving the point), and several *ternary quasi-peritectics P'* (two arrows entering, one arrow leaving). Two *saddle points s* are also shown. These are points of maximum *T* along the univariant line but of minimum *T* on the liquidus surface along a section joining the compositions of the two solids. For example, s_1 is at a maximum along the univariant $E_1 P_3'$, but is a minimum point on the liquidus along the straight line $\zeta s_1 \eta$.

Let us consider the events occurring during cooling from the liquid of an alloy of overall composition *a* in Fig. 1-24. The primary crystallization product will be the ε phase. Since this is a pure stoichiometric solid the crystallization path of the liquid will be along a straight line passing through *a* and extending to the composition of ε as shown in the figure.

Solidification of ε continues until the liquid attains a composition on the univariant valley. Thereafter the liquid composition follows the valley towards the point P_1' in co-existence with ε and ζ. At point P_1' the invariant *ternary quasi-peritectic reaction* occurs isothermally:

$$\text{liquid} + \varepsilon \rightarrow \delta + \zeta \qquad (1\text{-}112)$$

Since there are two reactants in a quasi-peritectic reaction, there are two possible outcomes: (i) the liquid is completely consumed before the ε phase; in this case, solidification will be complete at the point P_1'; (ii) ε is completely consumed before the liquid. In this case, solidification will continue with decreasing T along the univariant line $P_1'E_1$ with co-precipitation of δ and ζ until, at E, the liquid will solidify eutectically (liquid $\rightarrow \delta + \zeta + \eta$). To determine whether outcome (i) or (ii) occurs, we use the mass balance criterion that, for three-phase equilibrium, the overall composition *a* must always lie within the *tie-triangle* formed by the compositions of the three phases. Now, the triangle joining the compositions of δ, ε and ζ does not contain the point *a*, but the triangle joining the compositions of δ, ζ and liquid at P_1' does contain the point *a*. Hence, outcome (ii) occurs.

An alloy of overall composition *b* in Fig. 1-24 solidifies with ε as primary crystallization product until the liquid composition contacts the univariant line. Thereafter, co-precipitation of ε and β occurs with the liquid composition following the univariant valley until the liquid reaches the peritectic composition P. The invariant *ternary peritectic reaction* then occurs isothermally:

$$\text{liquid} + \varepsilon + \beta \rightarrow \zeta \qquad (1\text{-}113)$$

Since there are three reactants, there are three possible outcomes: (i) the liquid is consumed before either ε or β and solidification terminates at P; (ii) ε is consumed first, solidification then continues along the path PP_3'; or (iii) β is consumed first and solidification continues along the path PP_1'. Which outcome occurs depends on whether the overall composition *b* lies within the tie-triangle (i) $\varepsilon\beta\zeta$; (ii) $\beta\zeta P$, or (iii) $\varepsilon\zeta P$. In the example shown, outcome (i) will occur.

1.7.4 Ternary Isothermal Sections

Isothermal projections of the liquidus surface do not provide information on the compositions of the solid phases at equilibrium. However, this information can be presented at any one temperature on an *isothermal section* such as that shown for the Bi–Sn–Cd system at 423 K in Fig. 1-25. This phase diagram is a constant temperature slice through the space model of Fig. 1-23.

The liquidus lines bordering the one-phase liquid region of Fig. 1-25 are identical to the 423 K isotherms of the projection in Fig. 1-22. Point *c* in Fig. 1-25 is point *c* on the univariant line in Fig. 1-22. An alloy with overall composition in the one-phase liquid region of Fig. 1-25 at 423 K will consist of a single liquid phase. If the overall composition lies within one of the two-phase regions, then the compositions of the two phases are given by the ends of the *tie-line* which passes through the overall composition. For example, a sample with overall composition *p* in Fig. 1-25 will consist

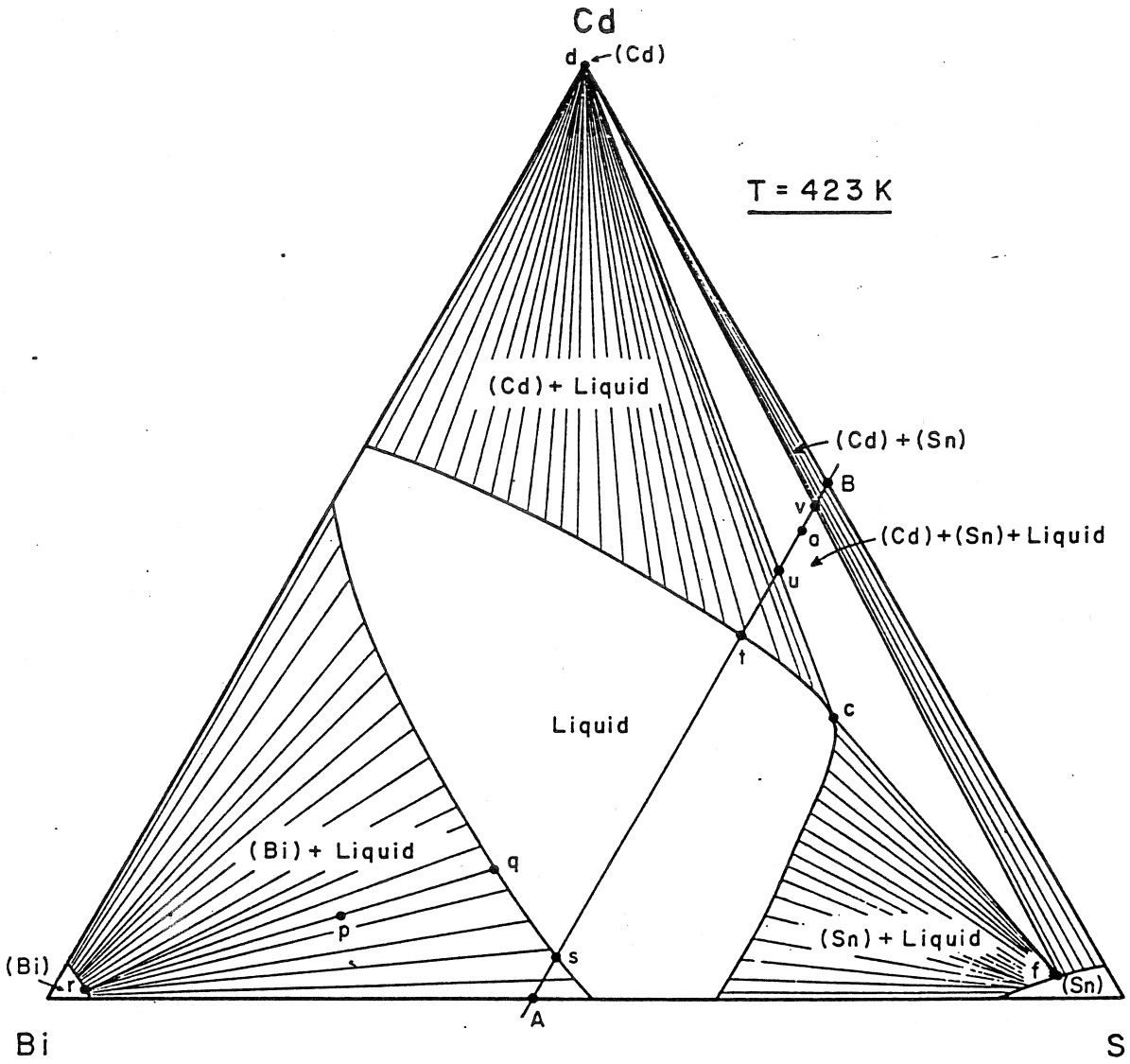

Figure 1-25. Isothermal section of the Bi–Sn–Cd system at 423 K at $P = 1$ bar (after Bray et al., 1961–1962). Extents of solid solubility in Bi and Sn have been exaggerated for clarity of presentation. (Reprinted from Pelton, 1996.)

of a liquid of composition q on the liquidus and a solid Bi-rich alloy of composition r on the solidus. The relative proportions of the two phases are given by the lever rule: (moles of liquid)/(moles of solid) $= pr/pq$, where pr and pq are the lengths of the tie-line segments.

In the case of solid Cd, the solid phase is nearly pure Cd, so all tie-lines of the (Cd+ liquid) region converge nearly to the corner of the triangle. In the case of Bi- and Sn-rich solids, some solid solubility is observed. (The actual extent of this solubility is somewhat exaggerated in Fig. 1-25 for the sake of clarity of presentation.) Alloys with overall compositions rich enough in Bi or Sn to lie within the single-phase (Sn) or (Bi) regions of Fig. 1-25 will consist at 423 K of single-phase solid solutions. Alloys with overall compositions at 423 K in the two-phase (Cd + Sn) region will consist of two solid phases.

Alloys with overall compositions within the three-phase triangle dcf will, at 423 K, consist of three phases: solid Cd- and Sn-rich solids with compositions at d and f and

liquid of composition *c*. To understand this better, consider an alloy of composition *a* in Fig. 1-25, which is the same composition as the point *a* in Fig. 1-22. In Sec. 1.7.3 we saw that when an alloy of this composition is cooled, the liquid follows the path *ab* in Fig. 1-22 with primary precipitation of Cd and then follows the univariant line with co-precipitation of Cd and Sn so that at 423 K the liquid is at the composition point *c*, and two solid phases are in equilibrium with the liquid.

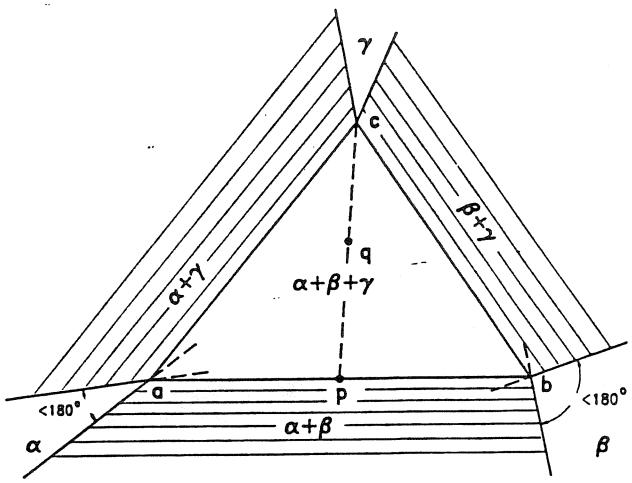

Figure 1-26. A tie-triangle in a ternary isothermal section illustrating the lever rule and the extension rule.

1.7.4.1 Topology of Ternary Isothermal Sections

At constant temperature the Gibbs energy of each phase in a ternary system is represented as a function of composition by a surface plotted in a right triangular prism with Gibbs energy as vertical axis and the composition triangle as base. Just as the compositions of phases at equilibrium in binary systems are determined by the points of contact of a common tangent line to their isothermal Gibbs energy curves, so the compositions of phases at equilibrium in a ternary system are given by the points of contact of a common tangent plane to their isothermal Gibbs energy surfaces. A common tangent plane can contact two Gibbs energy surfaces at an infinite number of pairs of points, thereby generating an infinite number of tie-lines within a two-phase region on an isothermal section. A common tangent plane to three Gibbs energy surfaces contacts each surface at a unique point, thereby generating a three-phase tie-triangle.

Hence, the principal topological units of construction of an isothermal ternary phase diagram are three-phase ($\alpha+\beta+\gamma$) tie-triangles as in Fig. 1-26 with their accompanying two-phase and single-phase areas. Each corner of the tie-triangle contacts a single-phase region, and from each edge of the triangle there extends a two-phase region. The edge of the triangle is a limiting tie-line of the two-phase region.

For overall compositions within the tie-triangle, the compositions of the three phases at equilibrium are fixed at the corners of the triangle. The relative proportions of the three phases are given by the *lever rule of tie-triangles*, which can be derived from mass balance considerations. At an overall composition *q* in Fig. 1-26 for example, the relative proportion of the γ phase is given by projecting a straight line from the γ corner of the triangle (point *c*) through the overall composition *q* to the opposite side of the triangle, point *p*. Then: (moles of γ)/(total moles) = *qp*/*cp* if compositions are expressed in mole fractions, or (weight of γ)/(total weight) = *qp*/*cp* if compositions are in weight percent.

Isothermal ternary phase diagrams are generally composed of a number of these topological units. An example for the Al–Zn–Mg system at 25 °C is shown in Fig. 1-27 (Köster and Dullenkopf, 1936). The β, γ, δ, θ, η and ζ phases are binary intermetallic compounds with small (~1 to 6%)

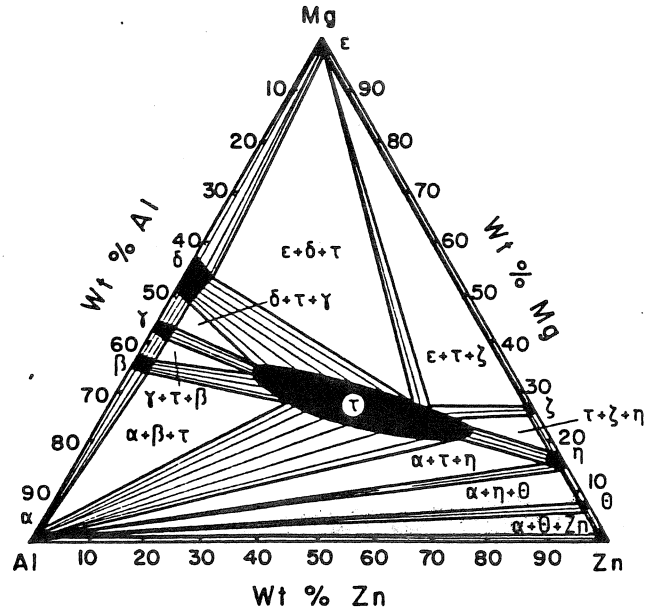

Figure 1-27. Ternary isothermal section of the Al–Zn–Mg system at 25°C at $P = 1$ bar (after Köster and Dullenkopf, 1936). (Reprinted from Pelton, 1983.)

ranges of stoichiometry which can dissolve a limited amount (~1 to 6%) of the third component. The τ phase is a ternary phase with a single-phase region existing over a fairly extensive oval-shaped central composition range. Examination of Fig. 1-27 shows that it consists of the topological units of Fig. 1-26.

An *extension rule*, a case of *Schreinemakers' Rule* (Schreinemakers, 1915), see Sec. 1.7.5, for ternary tie-triangles is illustrated in Fig. 1-26. At each corner, the extension of the boundaries of the single-phase regions, indicated by the broken lines, must either both project into the triangle as at point *a*, or must both project outside the triangle as at point *b*. Furthermore, the angle between these extensions must be less than 180°. For a proof, see Lipson and Wilson (1940) or Pelton (1995).

Many published phase diagrams violate this rule. For example, it is violated in Fig. 1-27 at the δ-corner of the (ε + δ + τ) tie-triangle.

Another important rule of construction, whose derivation is evident, is that within any two-phase region tie-lines must never cross one another.

1.7.5 Ternary Isopleths (Constant Composition Sections)

A vertical *isopleth*, or constant composition section through the space model of the Bi–Sn–Cd system, is shown in Fig. 1-28. The section follows the line *AB* in Fig. 1-22.

The phase fields on Fig. 1-28 indicate which phases are present when an alloy with an overall composition on the line *AB* is equilibrated at any temperature. For example, consider the cooling, from the liquid state, of an alloy of composition *a* which is on the line *AB* (see Fig. 1-22). At $T \approx 465$ K, precipitation of the solid (Cd) phase begins at point *a* in Fig. 1-28. At $T \approx 435$ K (point *b* in Figs. 1-22 and 1-28) the solid (Sn) phase begins to appear. Finally, at the eutectic temperature T_E, the ternary reaction occurs, leaving solid (Cd) + (Bi) + (Sn) at lower temperatures. The intersection of the isopleth with the univariant lines on Fig. 1-22 occurs at points *f* and *g* which are also indicated on Fig. 1-28. The intersection of this isopleth with the isothermal section at 423 K is shown in Fig. 1-25. The points *s*, *t*, *u* and *v* of Fig. 1-25 are also shown on Fig. 1-28.

It is important to note that on an isopleth the tie-lines do not, in general, lie in the plane of the diagram. Therefore, the diagram provides information only on which phases are present, not on their compositions. The boundary lines on an isopleth do not in general indicate the phase compositions, only the temperature at which a phase appears or disappears for a given overall composition. The lever rule cannot be applied on an isopleth.

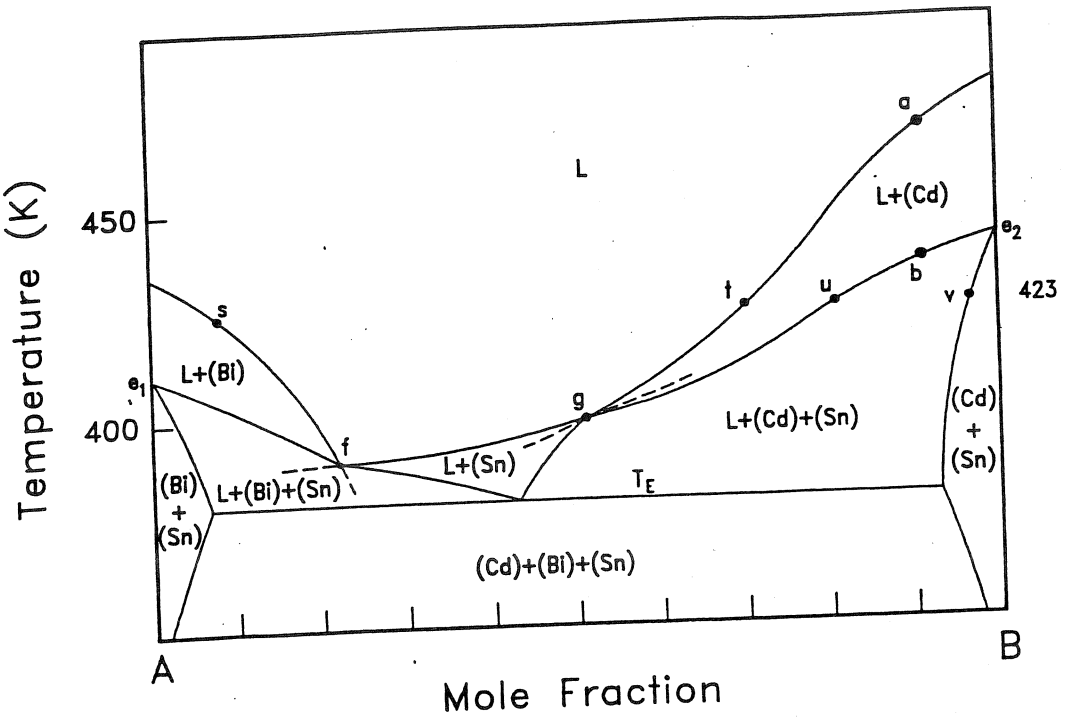

Figure 1-28. Isopleth (constant composition section) of the Bi–Sn–Cd system at $P=1$ bar following the line AB at $X_{Sn} = 0.45$ of Fig. 1-22. (Reprinted from Pelton, 1996).

Certain geometrical rules apply to isopleths. As a phase boundary line is crossed, one and only one phase either appears or disappears. This *Law of Adjoining Phase Regions* (Palatnik and Landau, 1964) is illustrated by Fig. 1-28. The only apparent exception occurs for the horizontal invariant line at T_E. However, if we consider this line to be a degenerate infinitely narrow four-phase region (L+(Cd)+(Bi)+(Sn)), then the law is also obeyed here.

Three or four boundary lines meet at intersection points. At an intersection point, such as point f or g, *Schreinemakers' Rule* applies. This is discussed in Sec. 1.9.

Apparent exceptions to these rules (such as, for example, five boundaries meeting at an intersection point) can occur if the section passes exactly through a node (such as a ternary eutectic point) of the space model. However, these apparent exceptions are really only limiting cases (see Prince, 1963 or 1966).

1.7.5.1 Quasi-Binary Phase Diagrams

Several of the binary phase diagrams in the preceding sections (Figs. 1-5, 1-10, 1-12, 1-14, 1-18) are actually isopleths of ternary systems. For example, Fig. 1-12 is an isopleth at constant $X_O = n_O/(n_{Mg} + n_{Ca} + n_O) = 0.5$ of the Mg–Ca–O system. However, all tie-lines lie within (or virtually within) the plane of the diagram because $X_O = 0.5$ in every phase. Therefore, the diagram is called a *quasi-binary* phase diagram.

1.7.6 Multicomponent Phase Diagrams

Only an introduction to multicomponent phase diagrams will be presented here. For more detailed treatments see Palatnik and Landau (1964), Prince (1963), Prince (1966) and Hillert (1998).

For systems of four or more components, two-dimensional sections are usually plot-

ted with one or more compositional variables held constant. Hence these sections are similar to the ternary isopleths discussed in Sec. 1.7.5. In certain cases, sections at constant chemical potential of one or more components (for example, at constant oxygen partial pressure) can be useful. These are discussed in Sec. 1.8.

Two sections of the Fe–Cr–V–C system (Lee and Lee, 1992) are shown in Figs. 1-29 and 1-30. The diagram in Fig. 1-29 is a T-composition section at constant Cr and V content, while Fig. 1-30 is a section at constant $T = 850\,°C$ and constant C content of 0.3 wt.%. The interpretation and topological rules of construction of these sections are the same as those for ternary isopleths, as discussed in Sec. 1.7.5. In fact, the same rules apply to a two-dimensional constant-composition section for a system of any number of components. The phase fields on the diagram indicate the phases present at equilibrium for an overall composition lying on the section. Tie-lines do not, in general, lie in the plane of the diagram, so the diagram does not provide information on the compositions or amounts of the phases present. As a phase boundary is crossed, one and only one phase appears or disappears (Law of Adjoining Phase Regions). If temperature is an axis, as in Fig. 1-29, then horizontal invariants like the line *AB* in Fig. 1-29 can appear. These can be considered as degenerate infinitely narrow phase fields of $(C + 1)$ phases, where C is the number of components (for isobaric diagrams). For example in Fig. 1-29, on the line *AB*, five phases are present. Three or four phase boundaries meet at intersection points at which Schreinemakers' Rule applies. It is illustrated by the extrapolations in Fig. 1-29 at points *a*, *b* and *c* and in Fig. 1-30 at points *b*, *c*, *n*, *i* and *s* (see discussions in Sec. 1.9).

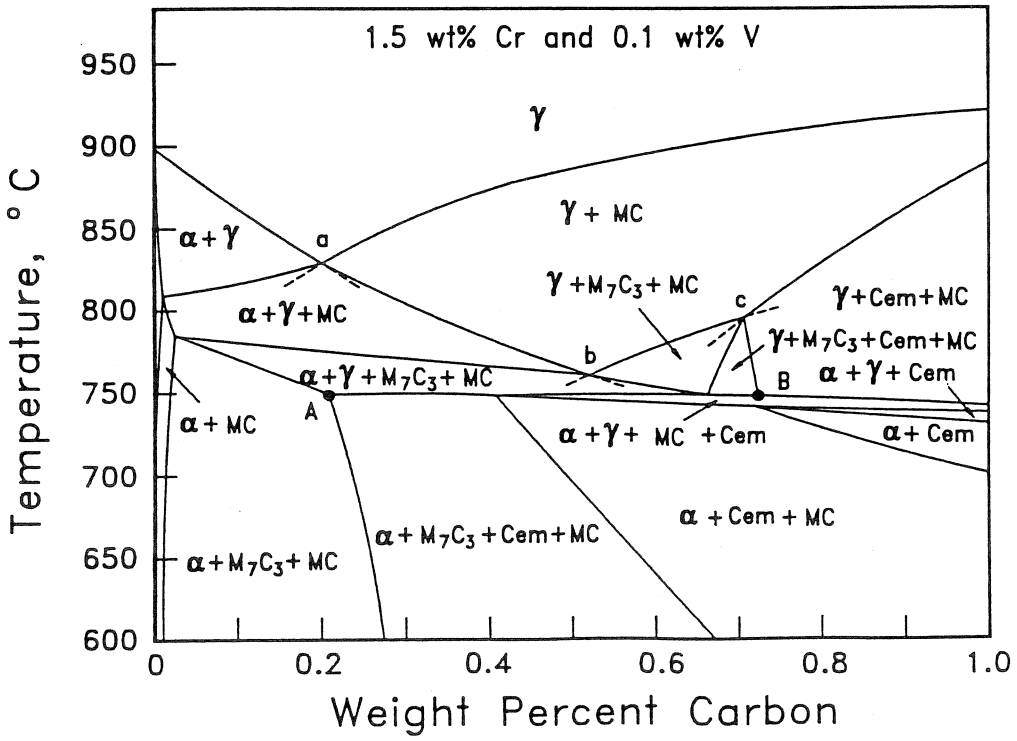

Figure 1-29. Section of the Fe–Cr–V–C system at 1.5 wt.% Cr and 0.1 wt.% V at $P = 1$ bar (Lee and Lee, 1992).

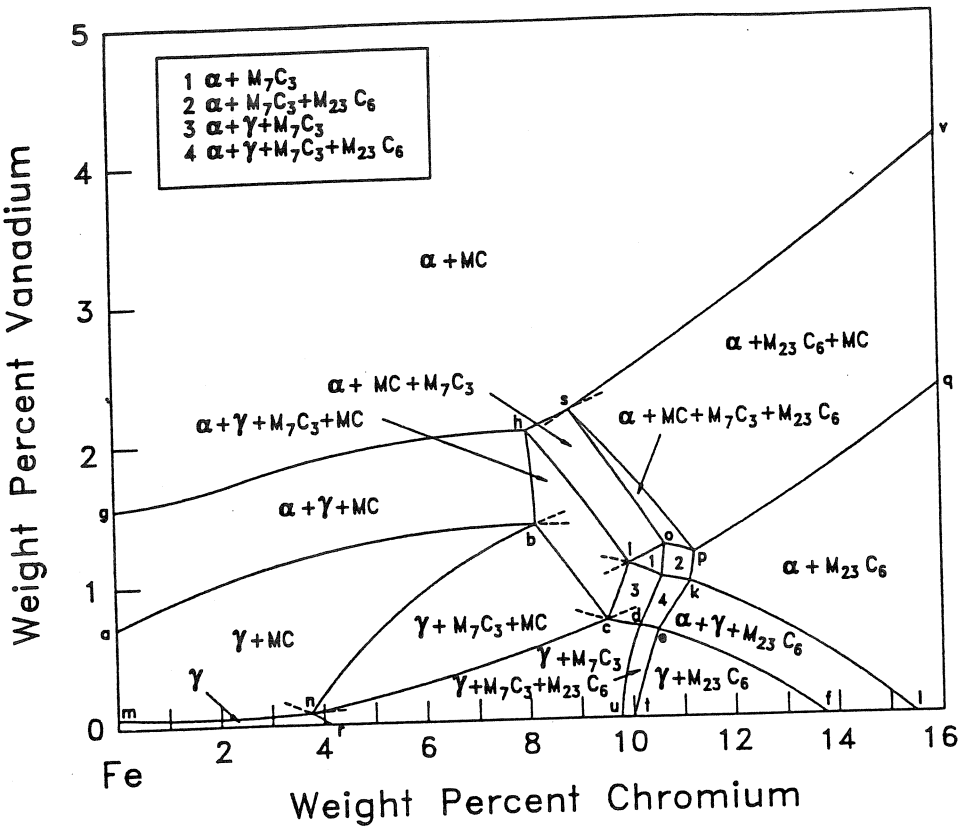

Figure 1-30. Section of the Fe–Cr–V–C system at 850 °C and 0.3 wt.% C at $P = 1$ bar (Lee and Lee, 1992).

1.7.7 Nomenclature for Invariant Reactions

As discussed in Sec. 1.5.12, in a binary isobaric temperature–composition phase diagram there are two possible types of invariant reactions: "eutectic-type" ($\beta \rightarrow \alpha + \gamma$), and "peritectic type" ($\alpha + \gamma \rightarrow \beta$). In a ternary system, there are "eutectic-type" ($\alpha \rightarrow \beta + \gamma + \delta$), "peritectic-type" ($\alpha + \beta + \gamma \rightarrow \delta$), and "quasiperitectic-type" ($\alpha + \beta \rightarrow \gamma + \delta$) invariants (Sec. 1.7.3). In a system of C components, the number of types of invariant reaction is equal to C. A reaction with one reactant, such as ($\alpha \rightarrow \beta + \gamma + \delta + \varepsilon$) is clearly a "eutectic-type" invariant reaction but in general there is no standard terminology. These reactions are conveniently described according to the numbers of reactants and products (in the direction which occurs upon cooling). Hence the reaction ($\alpha + \beta \rightarrow \gamma + \delta + \varepsilon$) is a *2 → 3 reaction*; the reaction ($\alpha \rightarrow \beta + \gamma + \delta$) is a *1 → 3 reaction*; and so on. The ternary peritectic-type *3 → 1 reaction* ($\alpha + \beta + \gamma \rightarrow \delta$) is an invariant reaction in a ternary system, a univariant reaction in a quaternary system, a bivariant reaction in a quinary system, etc.

1.7.8 Reciprocal Ternary Phase Diagrams

A *reciprocal ternary salt system* is one consisting of two cations and two anions, such as the Na^+, K^+/F^-, Cl^- system of Fig. 1-31. The condition of charge neutrality ($n_{Na^+} + n_{K^+} = n_{F^-} + n_{Cl^-}$) removes one degree of freedom. The system is thus *quasiternary* and its composition can be represented by two variables, usually chosen as the *cationic mole fraction* $X_K = n_K/(n_{Na} + n_K)$ and the *anionic mole fraction* $X_{Cl} = n_{Cl}/(n_F + n_{Cl})$, where n_i = number of moles of ion i. Note that $X_{Na} = (1 - X_K)$ and $X_F = (1 - X_{Cl})$.

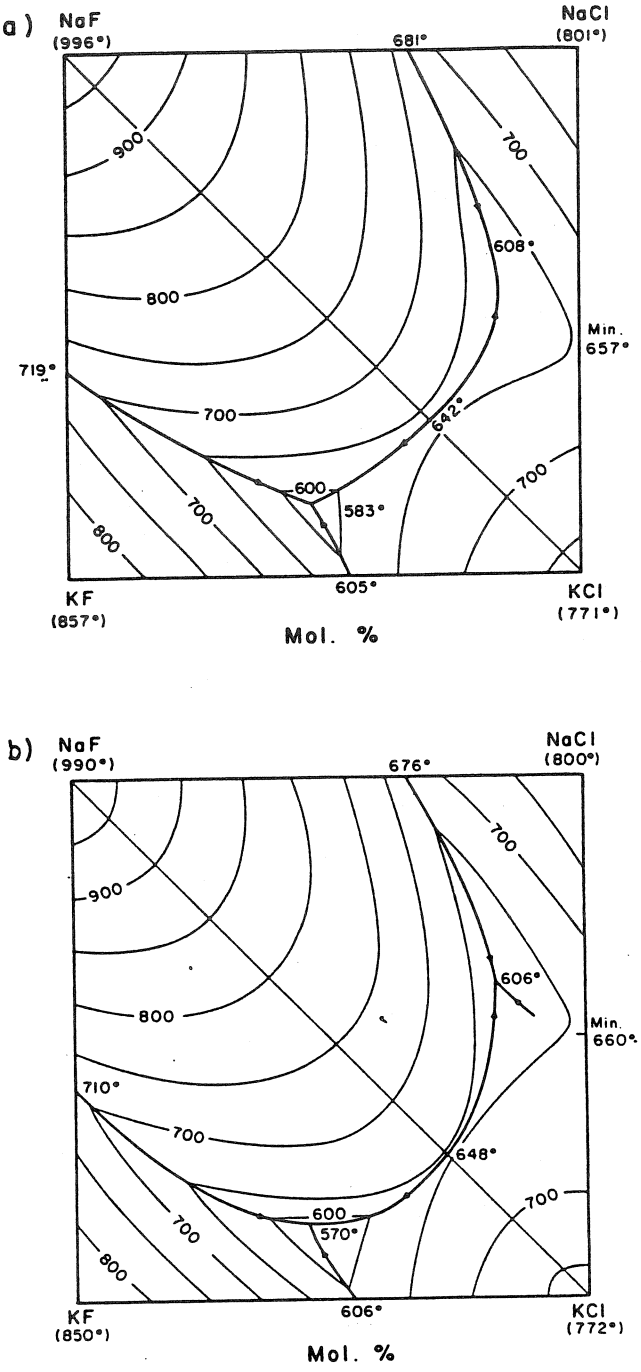

Figure 1-31. Projection of the liquidus surface of the Na^+, K^+/F^-, Cl^- reciprocal ternary system.
a) Calculated from optimized binary thermodynamic parameters.
b) As reported by Polyakov (1940).

The assumption has, of course, been made that the condition ($n_{Na}+n_K=n_F+n_{Cl}$) holds exactly in every phase. If there is a deviation from this exact stoichiometry, then the phase diagram is no longer quasi-ternary but is an isopleth of the four-component Na–K–F–Cl system, and tie-lines no longer necessarily lie in the plane of the diagram.

In Fig. 1-31 the cationic and anionic fractions are plotted as axes of a square. Compositions corresponding to the four neutral salts (KF, KCl, NaCl, NaF) are found at the corners of the square. Edges of the square correspond to the binary subsystems such as NaF–NaCl. A ternary space model (analogous to Fig. 1-23) can be constructed with temperature as vertical axis. The phase diagram of Fig. 1-31 is a polythermal projection of the liquidus surface upon the composition square.

In this system, three of the binary edges are simple eutectic systems, while the NaCl–KCl binary system exhibits a solidus/liquidus minimum. There is a ternary eutectic at 570 °C in Fig. 1-31(b). The NaF–KCl diagonal contains a saddle point at 648 °C in Fig. 1-31(b). This saddle point is a eutectic of the *quasibinary system* NaF–KCl. That is, a binary phase diagram NaF–KCl could be drawn with one simple eutectic at 648 °C. However, the NaCl–KF system, which forms the other diagonal, is not a quasibinary system. If compositions lying on this diagonal are cooled at equilibrium from the liquid, solid phases whose compositions do not lie on this diagonal can precipitate. Hence, a simple binary phase diagram cannot be drawn for the NaCl–KF system.

For systems such as Ca^{2+}, Na^+/F^-, SO_4^{2-} in which the ions do not all have the same charge, composition axes are conveniently expressed as equivalent ionic fractions (e.g. $Y_{Ca}=2n_{Ca}/(2n_{Ca}+n_{Na})$), see Sec. 1.9.2.1.

The concept of reciprocal systems can be generalized beyond simple salt systems and is closely related to the sublattice model (Sec. 1.10.1).

For further discussion and references, see Pelton (1988b) and Blander (1964).

1.8 Phase Diagrams with Potentials as Axes

So far we have considered mainly isobaric temperature–composition phase diagrams. However there are many other kinds of phase diagrams of interest in materials science and technology with pressure, chemical potentials, volume, etc. as axes. These can be classified into geometrical types according to their rules of construction.

For instance, binary isothermal $P-X$ diagrams as in Fig. 1-8 are members of the same type as binary isobaric $T-X$ diagrams because they are both formed from the same topological units of construction. Other useful phase diagrams of this same geometrical type are isothermal chemical potential–composition diagrams for ternary systems. An example is shown in the lowest panel of Fig. 1-32 (Pelton and Thompson, 1975) for the Co–Ni–O system at $T = 1600$ K (and at a constant total hydrostatic pressure of 1 bar). Here the logarithm of the equilibrium partial pressure of O_2 is plotted versus the metal ratio $\xi = n_{Ni}/(n_{Co}+n_{Ni})$, where n_i = number of moles of i. There are two phases in this system under these conditions, a solid alloy solution stable at lower p_{O_2}, and a solid solution of CoO and NiO stable at higher p_{O_2}. For instance, point a gives p_{O_2} for the equilibrium between pure Co and pure CoO at 1600 K. Between the two single-phase regions is a two-phase (alloy + oxide) region. At any overall composition on the tie-line cd between points c and d, two phases will be observed, an alloy of composition d and an oxide of composition c. The lever rule applies just as for binary $T-X$ diagrams.

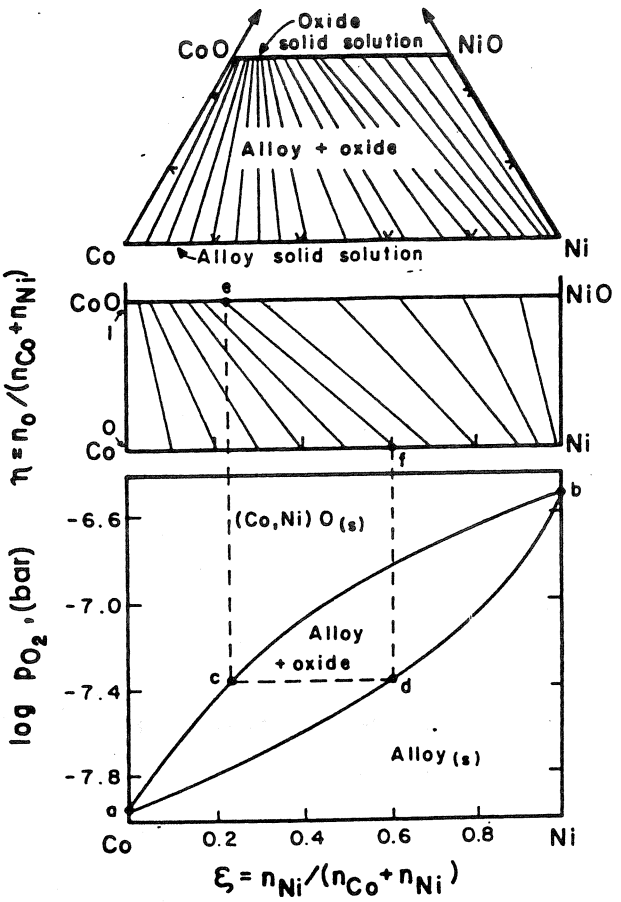

Figure 1-32. Corresponding phase diagrams for the Co–Ni–O system at 1600 K (from Pelton and Thompson, 1973).

The usual isothermal section of the ternary Co–Ni–O system at 1600 K is shown in the top panel of Fig. 1-32. There are two single-phase regions with a two-phase region between them. The single-phase areas are very narrow because oxygen is only very slightly soluble in the solid alloy and CoO and NiO are very stoichiometric oxides. In the central panel of Fig. 1-32 this same diagram is shown with the composition triangle "opened up" by putting the oxygen corner at infinity. This can be done if the vertical axis becomes $\eta = n_O/(n_{Co}+n_{Ni})$ with the horizontal axis as $\xi = n_{Ni}/(n_{Co}+n_{Ni})$. These are known as *Jänecke coordinates*. It can be seen in Fig. 1-32 that each tie-line, ef, of the isothermal section corresponds to a tie-line cd of the

$\log p_{O_2} - \xi$ diagram. This underscores the fact that every tie-line of a ternary isothermal section corresponds to a constant chemical potential of each of the components.

Another example of a $\log p_{O_2} - \xi$ diagram is shown for the Fe–Cr–O system at 1573 K in the lower panel of Fig. 1-33 (Pelton and Schmalzried, 1973). The corresponding ternary isothermal section in Jänecke coordinates is shown in the upper panel. Each of the invariant three-phase tie-triangles in the isothermal section corresponds to an invariant line in the $\log p_{O_2} - \xi$ diagram. For example, the (spinel + (Fe, Cr) O + alloy) triangle with corners at points *a*, *b* and *c* corresponds to the "eutectic-like" or *eutecular* invariant with the same phase compositions *a*, *b* and *c* at $\log p_{O_2} \approx -10.7$. We can see that within a three-phase tie-triangle, p_{O_2} is constant.

An example of yet another kind of phase diagram of this same geometrical type is shown in Fig. 1-34. For the quaternary $Fe-Cr-O_2-SO_2$ system at $T = 1273$ K and at constant $p_{SO_2} = 10^{-7}$ bar, Fig. 1-34 is a plot of $\log p_{O_2}$ versus the molar metal ratio

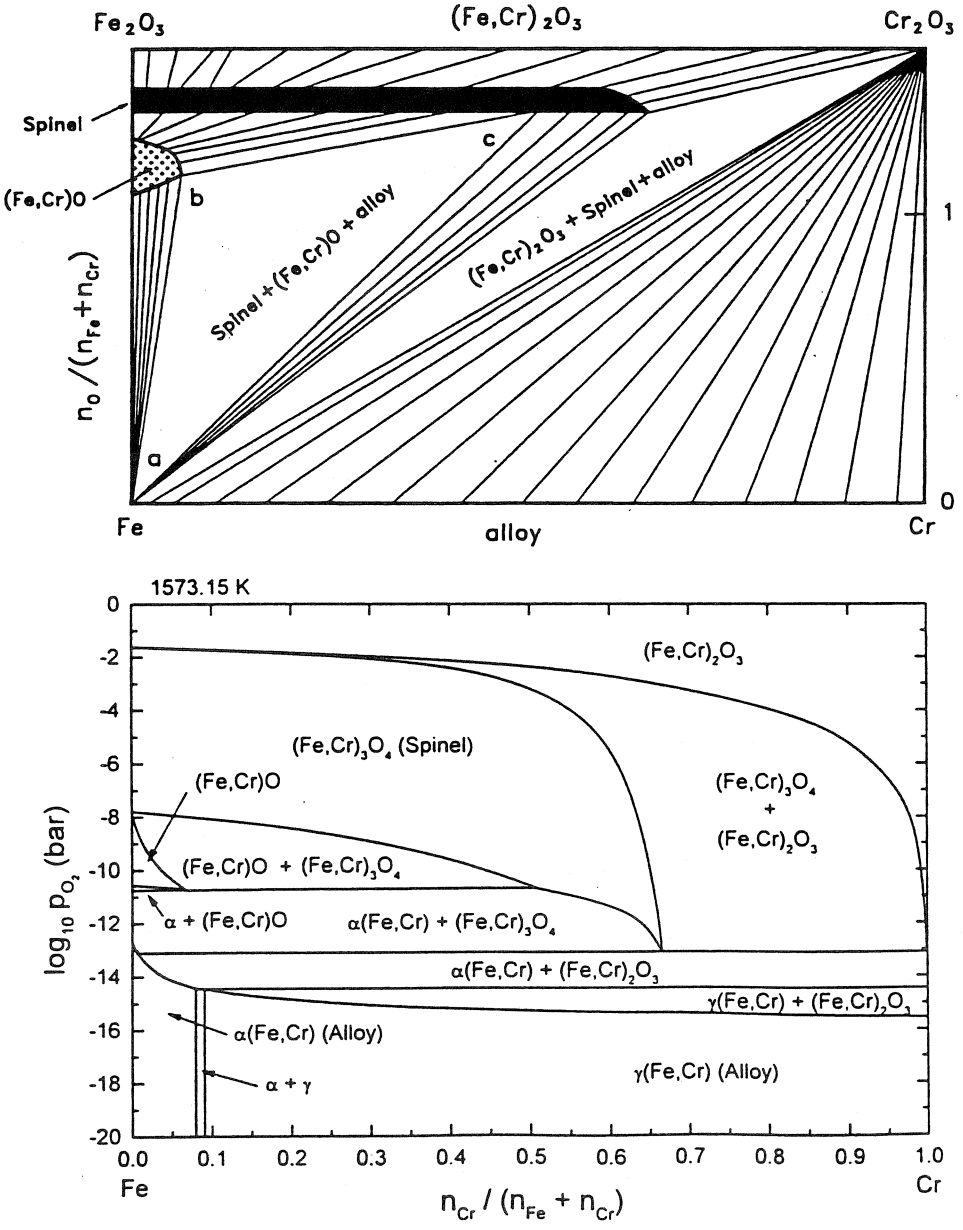

Figure 1-33. Corresponding phase diagrams for the Fe–Cr–O system at 1573 K (Pelton and Schmalzried, 1973). Experimental points from Katsura and Muan (1964).

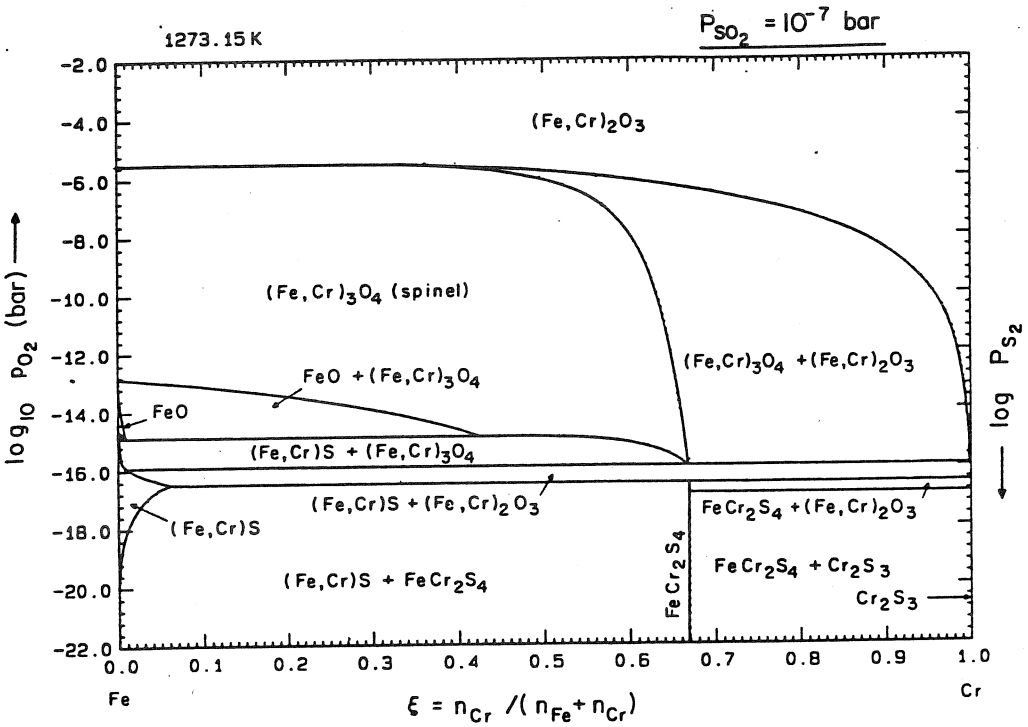

Figure 1-34. Calculated phase diagram of log p_{O_2} versus molar metal ratio at $T = 1273.15$ K and $p_{SO_2} = 10^{-7}$ bar for the Fe–Cr–SO_2–O_2 system.

ξ. Since log p_{O_2} varies as $-1/2$ log p_{S_2} when p_{SO_2} and T are constant, Fig. 1-34 is also a plot of log p_{S_2} versus ξ.

Plotting T versus ξ at constant p_{O_2} in the Fe–Cr–O system, or at constant p_{O_2} and p_{SO_2} in the Fe–Cr–SO_2–O_2 system, will also result in phase diagrams of this same geometrical type. Often for ceramic systems, we encounter "binary" phase diagrams such as that for the "CaO–Fe_2O_3" system in Fig. 1-35, which has been taken from Phillips and Muan (1958). How are we to interpret such a diagram? How, for instance, do we interpret the composition

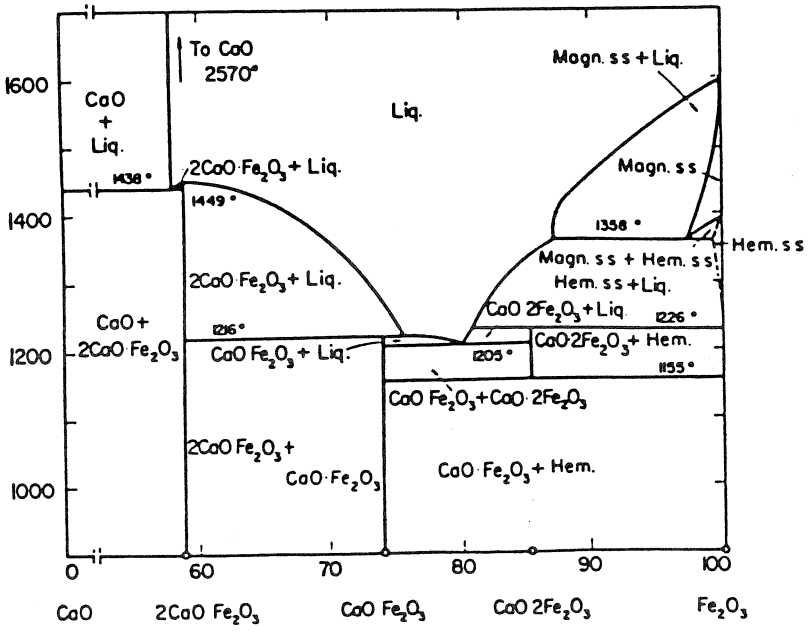

Figure 1-35. Phase diagram for the "CaO–Fe_2O_3" system in air ($p_{O_2} = 0.21$ bar) from Phillips and Muan (1958) (Reprinted by permission of the American Ceramic Society from Levin et al., 1964).

axis when applied to the magnetite phase? In light of the preceding discussion, it can be seen that such diagrams are really $T-\xi$ plots at constant p_{O_2}, where ξ is the metal ratio in any phase. The diagram will be different at different oxygen partial pressures. If p_{O_2} is not fixed, the diagram cannot be interpreted.

It can be seen that the diagrams discussed above are of the same geometrical type as binary $T-X$ diagrams because they are all composed of the same geometrical units of construction as in Fig. 1-16. Their interpretation is thus immediately clear to anyone familiar with binary $T-X$ diagrams. Chemical potential–composition

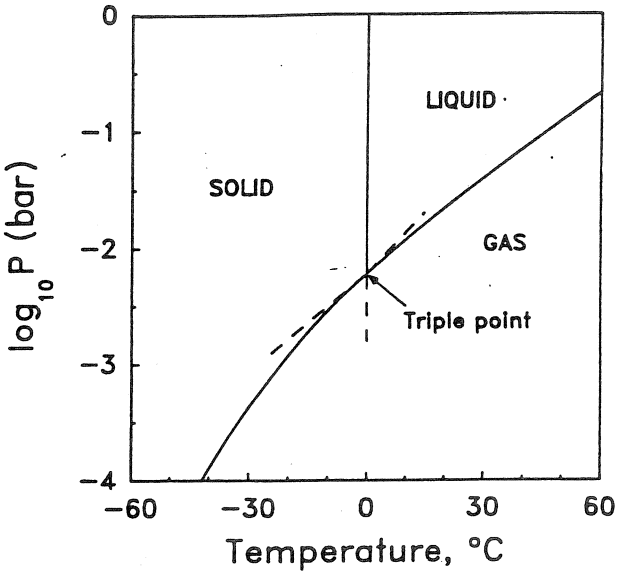

Figure 1-36. Pressure-temperature phase diagram of H_2O.

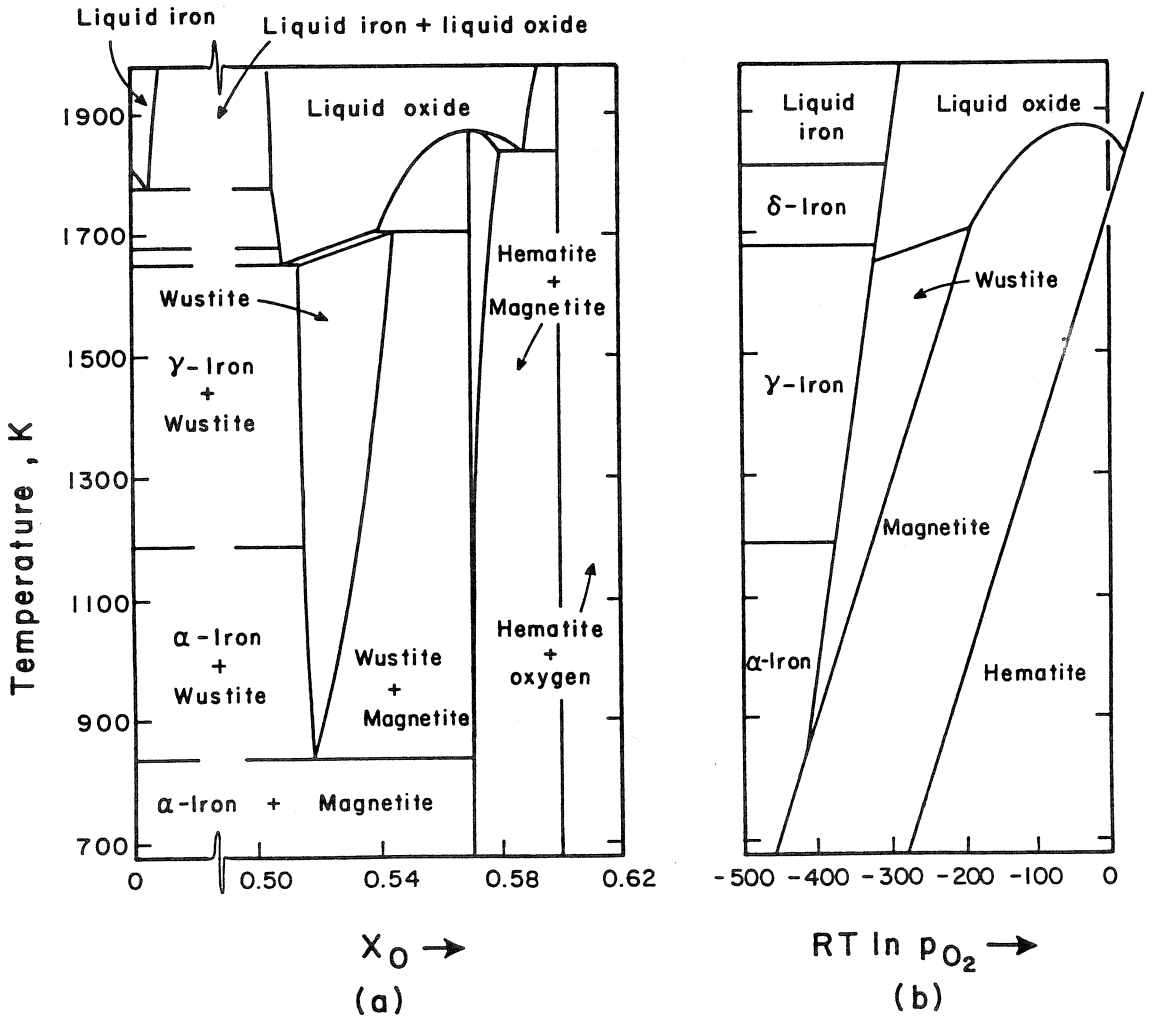

Figure 1-37. Corresponding phase diagrams for the Fe–O system at P_{TOTAL} = 1 bar (after Muan and Osborn, 1965).

diagrams (Figs. 1-32 to 1-34) are useful in the study of hot corrosion, metallurgical roasting processes, chemical vapor deposition, and many aspects of materials processing.

Another important geometrical type of phase diagram is exemplified by $P-T$ phase diagrams for one-component systems, as shown for H_2O in Fig. 1-36. In such diagrams (see also Chapter 10 by Kunz (2001)) bivariant single-phase regions are indicated by areas, univariant two-phase regions by lines, and invariant three-phase regions by *triple points*. An important rule of construction is the *extension rule*, which is illustrated by the broken lines in Fig. 1-36. At a triple point, the extension of any two-phase line must pass into the single-phase region of the third phase. Clearly, the predominance diagrams of Figs. 1-1 to 1-3 are of this same geometrical type.

As yet another example of this geometrical type of diagram, a plot of $RT \ln p_{O_2}$ versus T for the Fe–O system is shown in Fig. 1-37(b). Again, one-, two- and three-phase regions are indicated by areas, lines and triple points respectively. Fig. 1-37(a) is the binary T–composition phase diagram for the Fe–O system. The correspondence between Figs. 1-37(a) and 1-37(b) is evident. Each two-phase line of Fig. 1-37(b) "opens up" to a two-phase region of Fig. 1-37(a). Each tie-line of a two-phase region in Fig. 1-37(a) can thus be seen to correspond to a constant p_{O_2}. Triple points in Fig. 1-37(b) become horizontal invariant lines in Fig. 1-37(a).

Yet another type of phase diagram is shown in Fig. 1-38. This is an isothermal

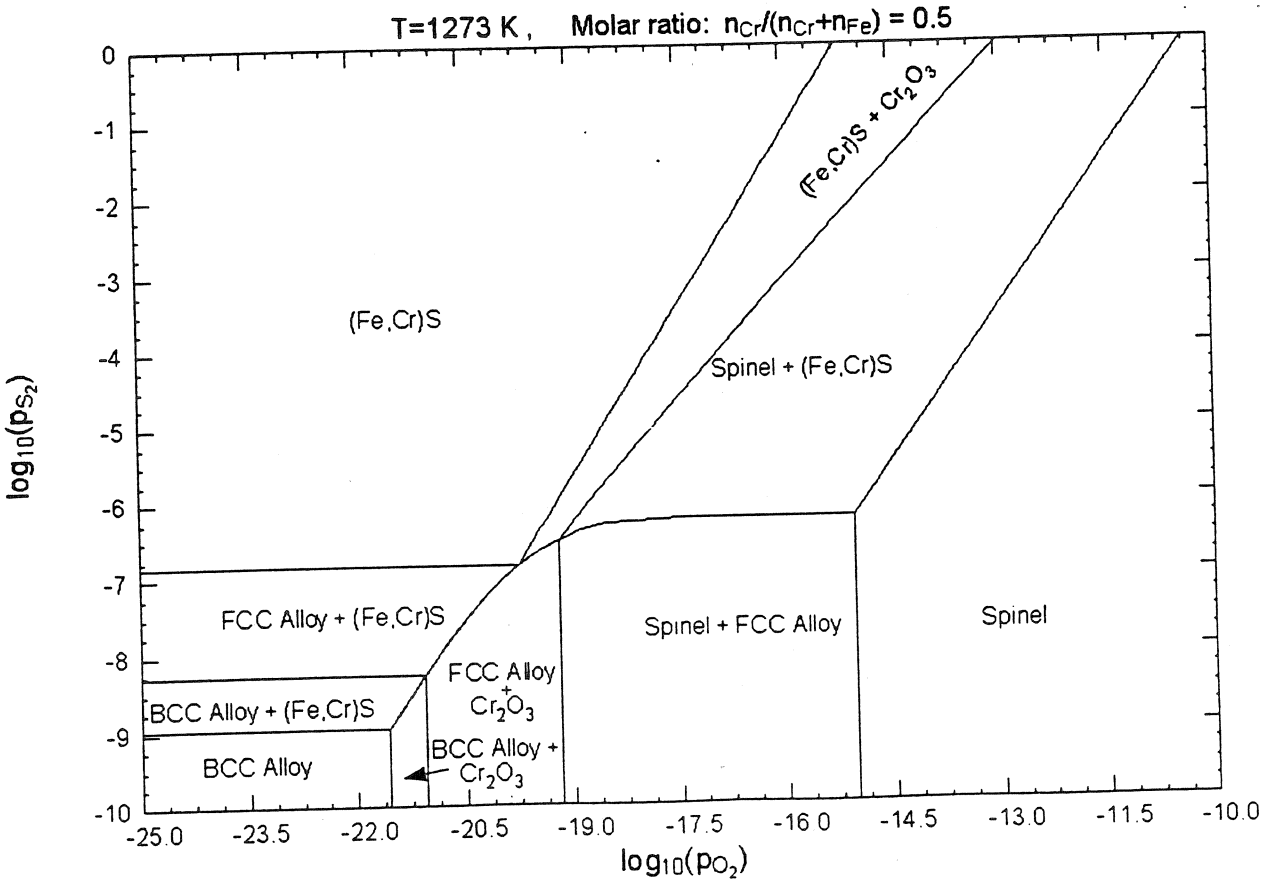

Figure 1-38. Phase diagram of log p_{S_2} versus log p_{O_2} at 1273 K and constant molar metal ratio $n_{Cr}/(n_{Fe}+n_{Cr}) = 0.5$ in the Fe–Cr–S_2–O_2 system.

section at constant molar metal ratio $n_{Cr}/(n_{Fe}+n_{Cr})=0.5$ for the Fe–Cr–S_2–O_2 system. This diagram was calculated thermodynamically from model parameters. The axes are the equilibrium sulfur and oxygen partial pressures. Three or four boundary lines can meet at an intersection point. Some of the boundary lines on Fig. 1-38 separate a two-phase region ($\alpha+\beta$) from another two-phase region ($\alpha+\gamma$). These lines thus represent the conditions for three-phase ($\alpha+\beta+\gamma$) equilibrium.

1.9 General Phase Diagram Geometry

Although the various phase diagrams shown in the preceding sections may appear to have quite different geometries, it can be shown that, in fact, all true phase diagram sections obey the same set of geometrical rules. Although these rules do not apply directly to phase diagram projections such as Figs. 1-22, 1-24 and 1-31, such diagrams can be considered to consist of portions of several phase diagram sections projected onto a common plane.

By "true" phase diagram we mean one in which each point of the diagram represents one unique equilibrium state. In the present section we give the general geometrical rules that apply to all true phase diagram sections, and we discuss the choices of axes and constants that ensure that the diagram is a true diagram.

We must first make some definitions. In a system of C components we can define $(C+2)$ *thermodynamic potentials* ϕ_i. These are T, P, μ_1, μ_2, ..., μ_C, where μ_i is the chemical potential defined in Eq. (1-23). For each potential there is a *corresponding extensive variable* q_i related by:

$$\phi_i = (\partial U/\partial q_i)_{q_j(j\neq i)} \qquad (1\text{-}114)$$

Table 1-1. Corresponding pairs of potentials ϕ_i and extensive variables q_i.

ϕ_i:	T	P	μ_1	μ_2 ... μ_C
q_i:	S	$-V$	n_1	n_2 ... n_C

where U is the internal energy of the system. The corresponding potentials and extensive variables are listed in Table 1-1. It may also be noted that the corresponding pairs are found together in the terms of the *general Gibbs–Duhem equation:*

$$S\,dT - V\,dP + \sum n_i\,d\mu_i = 0 \qquad (1\text{-}115)$$

1.9.1 General Geometrical Rules for All True Phase Diagram Sections

The *Law of Adjoining Phase Regions* applies to all true sections. As a phase boundary line is crossed, one and only one phase either appears or disappears.

If the vertical axis is a potential (T, P, μ_i), then horizontal invariant lines like the eutectic line in Fig. 1-12 or the line AB in Fig. 1-29 will be seen when the maximum number of phases permitted by the phase rule are at equilibrium. However, if these are considered to be degenerate infinitely narrow phase fields, then the Law of Adjoining Phase Regions still applies. This is illustrated schematically in Fig. 1-39 where the three-phase eutectic line has been "opened up". Similarly, if both axes are potentials, then many phase boundaries may be degenerate infinitely narrow regions. For example, all phase boundaries on Figs. 1-1 to 1-3, 1-36 and 1-37(b) are degenerate two-phase regions which are schematically shown "opened up" on Fig. 1-40.

All phase boundary lines in a true phase diagram meet at nodes where exactly four lines converge, as in Fig. 1-41. N phases (α_1, α_2, ..., α_N) where $N\geq 1$ are common

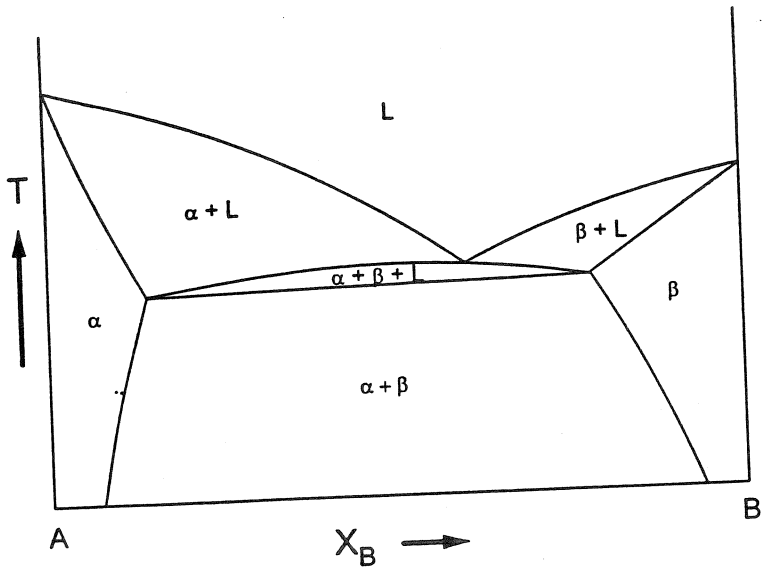

Figure 1-39. An isobaric binary T–X phase diagram (like Fig. 1-12) with the eutectic line "opened up" to illustrate that this is a degenerate 3-phase region.

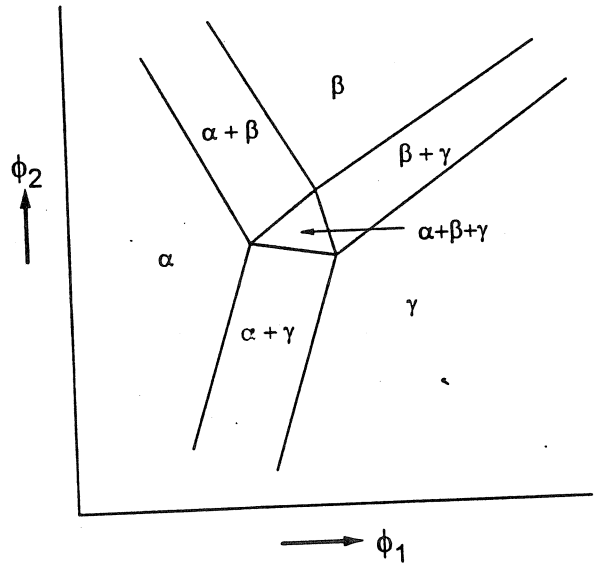

Figure 1-40. A potential–potential phase diagram (like Fig. 1-1 or Fig. 1-36) with the phase boundaries "opened up" to illustrate that they are degenerate 2-phase regions.

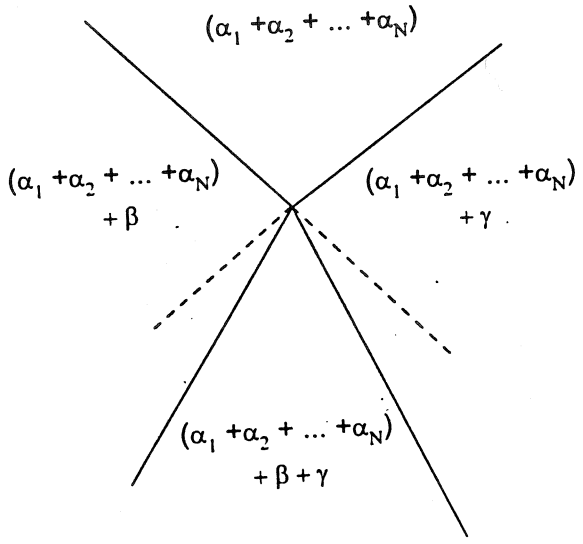

Figure 1-41. A node in a true phase diagram section.

to all four regions. *Schreinemakers' Rule* states that the extensions of the boundaries of the N-phase region must either both lie within the $(N+1)$-phase regions as in Fig. 1-41 or they must both lie within the $(N+2)$-phase region. This rule is illustrated by the extrapolations in Fig. 1-29 at points *a*, *b* and *c* and in Fig. 1-30 at points *b*, *c*, *n*, *i* and *s*. The applicability of Schreinemakers' Rule to systems of any number of components was noted by Hillert (1985) and proved by Pelton (1995). In the case of degenerate phase regions, all nodes can still be considered to involve exactly four boundary lines if the degenerate boundaries are "opened up" as in Figs. 1-39 and 1-40.

An objection might be raised that a minimum or a maximum in a two-phase region in a binary temperature–composition phase diagram, as in Fig. 1-10 or in the lower panel of Fig. 1-16, represents an ex-

ception to Schreinemakers' Rule. However, the extremum in such a case is not actually a node where four phase boundaries converge, but rather a point where two boundaries touch. Such extrema in which two phase boundaries touch with zero slope may occur for a C-phase region in a phase diagram of a C-component system when one axis is a potential. For example, in an isobaric temperature–composition phase diagram of a four-component system, we may observe a maximum or a minimum in a four-phase region separating two three-phase regions. A similar maximum or minimum in a $(C-n)$-phase region, where $n>0$, may also occur, but only for a degenerate or special composition path. For further discussion, see Hillert (1998).

1.9.1.1 Zero Phase Fraction Lines

All phase boundaries on true phase diagram sections are *zero phase fraction* (*ZPF*) *lines*, a very useful concept introduced by Gupta et al. (1986). There are ZPF lines associated with each phase. On one side of its ZPF line the phase occurs, while on the other side it does not. For example, in Fig. 1-30 the ZPF line for the α phase is the line *abcdef*. The ZPF line for the γ phase is *ghijkl*. For the MC phase the ZPF line is *mnciopq*. The ZPF line for M_7C_3 is *rnbhspket*, and for $M_{23}C_6$ it is *udjosv*. These five ZPF lines yield the entire two-dimensional phase diagram. Phase diagram sections plotted on triangular coordinates as in Figs. 1-25 and 1-27 also consist of ZPF lines.

In the case of phase diagrams with degenerate regions, ZPF lines for two different phases may be coincident over part of their lengths. For example, in Fig. 1-12, line *CABD* is the ZPF line of the liquid, while *CEBF* and *DEAG* are the ZPF lines for the α and β phases respectively. In Fig. 1-1, all lines are actually two coincident ZPF lines.

The ZPF line concept is very useful in the development of general algorithms for the thermodynamic calculation of phase diagrams as discussed in Sec. 1-12.

1.9.2 Choice of Axes and Constants of True Phase Diagrams

In a system of C components, a two-dimensional diagram is obtained by choosing two axis variables and holding $(C-1)$ other variables constant. However, not all choices of variables will result in a true phase diagram. For example on the $P-V$ diagram for H_2O shown schematically in Fig. 1-42, at any point in the area where the (S+L) and (L+G) regions overlap there are two possible equilibrium states of the system. Similarly, the diagram of carbon activity versus X_{Cr} at constant T and P in the Fe–Cr–C system in Fig. 1-43 (Hillert, 1997) exhibits a region in which there is no unique equilibrium state.

In order to be sure that a diagram is a true phase diagram, we must choose one *and only one* variable (either ϕ_i or q_i) from

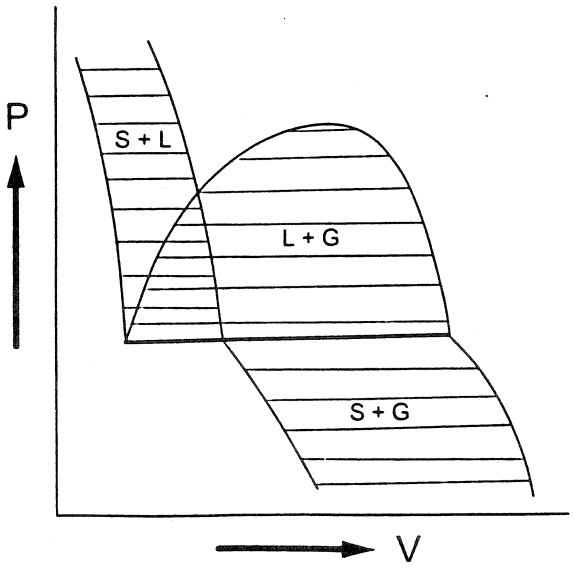

Figure 1-42. Schematic $P-V$ diagram for H_2O. This is not a true phase diagram.

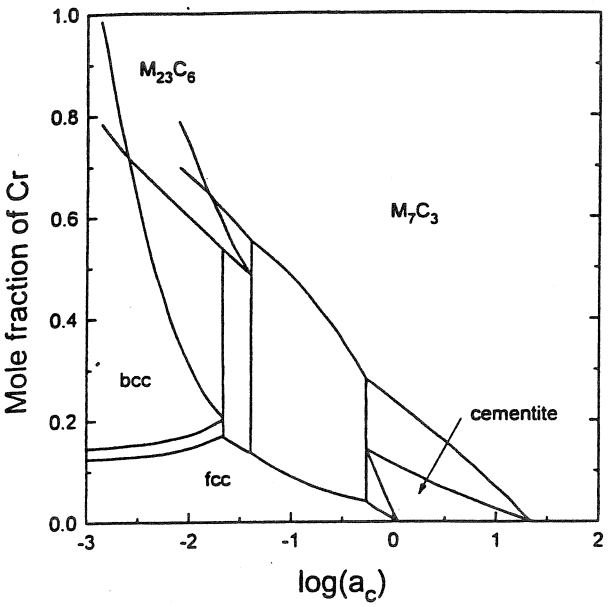

Figure 1-43. Carbon activity versus mole fraction of Cr at constant T and P in the Fe–Cr–C system. This is not a true phase diagram (from Hillert, 1997).

each of the $(C+2)$ conjugate pairs in Table 1-1. (Also, at least one of these must be an extensive variable q_i.) From among the $n(1 \le n \le C+2)$ selected extensive variables, $(n-1)$ independent ratios are then formed. These $(n-1)$ ratios along with the $(C+2-n)$ selected potentials are the $(C+1)$ required variables. Two are chosen as axis variables and the remainder are held constant.

As a first example, consider a binary system with components A–B. The conjugate pairs are (T, S), $(P, -V)$, (μ_A, n_A) and (μ_B, n_B). Let us choose one variable from each pair as follows: T, P, n_A, n_B. From the selected extensive variables, n_A and n_B, we form a ratio such as $n_B/(n_A+n_B)=X_B$. The resultant phase diagram variables are T, P, X_B. Choosing any two as axes and holding the third constant will give a true phase diagram as in Fig. 1-6 or Fig. 1-8.

As a second example, consider Fig. 1-38 for the Fe–Cr–S_2–O_2 system. We choose one variable from each conjugate pair as follows: T, P, μ_{S_2}, μ_{O_2}, n_{Fe}, n_{Cr}. From the selected extensive variables we form the ratio $n_{Fe}/(n_{Fe}+n_{Cr})$. Fig. 1-38 is a plot of μ_{S_2} versus μ_{O_2} at constant T, P and $n_{Fe}/(n_{Fe}+n_{Cr})$.

In Fig. 1-28 the selected variables are T, P, n_{Bi}, n_{Sn} and n_{Cd}, and ratios are formed from the selected extensive variables as $n_{Cd}/(n_{Cd}+n_{Bi})$ and $n_{Sn}/(n_{Cd}+n_{Bi}+n_{Sn}) = X_{Sn}$. Fig. 1-28 is a plot of T versus $n_{Cd}/(n_{Cd}+n_{Bi})$ at constant P and X_{Sn}.

Fig. 1-42, the $P-V$ diagram for H_2O, is not a true phase diagram because P and V are members of the same conjugate pair. For the diagram shown in Fig. 1-43, we can choose one variable from each pair as follows: T, P, μ_C, n_{Fe}, n_{Cr}. However the vertical axis is $X_{Cr}=n_{Cr}/(n_{Fe}+n_{Cr}+n_C)$. This ratio is not allowed because it contains n_C which is not on the list of chosen variables. That is, since we have chosen μ_C to be an axis variable, we cannot also choose n_C. Hence, Fig. 1-43 is not a true phase diagram. A permissible choice for the vertical axis would be $n_{Cr}/(n_{Fe}+n_{Cr})$ (see Fig. 1-33). Note that many regions of Figs. 1-42 and 1-43 do represent unique equilibrium states. That is, the procedure given here is a sufficient, but not necessary, condition for constructing true phase diagrams.

To apply this procedure simply, the components of the system should be formally defined to correspond to the desired axis variables or constants. For example, in Fig. 1-1 we wish to plot p_{SO_2} and $\log p_{O_2}$ as axes. Hence we define the components as Cu–SO_2–O_2 rather than Cu–S–O.

In several of the phase diagrams in this chapter, $\log p_i$ or $RT \ln p_i$ has been substituted for μ_i as axis variable or constant. From Eq. (1-32), this substitution can clearly be made if T is constant. However, even when T is an axis of the phase diagram as in Fig. 1-37(b), this substitution is still permissible since μ_i^0 is a monotonic function of T. The substitution of $\ln a_i$ for

μ_i results in a progressive expansion and displacement of the axis with increasing T that preserves the overall geometry of the diagram.

1.9.2.1 Tie-lines

If only potentials (T, P, μ_i) are held constant, then all tie-lines lie in the plane of the phase diagram section. In this case, the compositions of the individual phases at equilibrium can be read from the phase diagram, and the lever rule applies as, for example, in Figs. 1-6, 1-25, 1-33 or 1-34. However, if a ratio of extensive variables, such as a composition, is held constant as in the isopleths of Figs. 1-28 to 1-30, then in general, tie-lines do not lie in the plane.

If both axes are composition variables (ratios of n_i), and if only potentials are held constant, then it is desirable that the tie-lines (which lie in the plane) be straight lines. It can be shown (Pelton and Thompson, 1975) that this will only be the case if the denominators of the two composition variable ratios are the same. For example, in the central panel of Fig. 1-32, which is in Jänecke coordinates, the composition variables, $n_{Co}/(n_{Co}+n_{Ni})$ and $n_O/(n_{Co}+n_{Ni})$, have the same denominator. This same diagram can be plotted on triangular coordinates as in the upper panel of Fig. 1-32 and such a diagram can also be shown (Pelton and Thompson, 1975) to give straight tie-lines.

Similarly, in the quasiternary reciprocal phase diagram of Fig. 1-31 the vertical and horizontal axes are $n_{Na}/(n_{Na}+n_K)$ and $n_{Cl}/(n_{Cl}+n_F)$. To preserve charge neutrality, $(n_{Na}+n_K)=(n_{Cl}+n_F)$, and so the tie-lines are straight. Generally, in quasiternary reciprocal salt phase diagrams, straight tie-lines are obtained by basing the composition on one equivalent of charge. For example, in the $CaCl_2$–NaCl–CaO–Na_2O system we would choose as axes the *equivalent cationic and anionic fractions*, $n_{Na}/(n_{Na}+2n_{Ca})$ and $n_{Cl}/(n_{Cl}+2n_O)$, whose denominators are equal because of charge neutrality.

1.9.2.2 Corresponding Phase Diagrams

When only potentials are held constant and when both axes are also potentials, then the geometry exemplified by Figs. 1-1 to 1-3, 1-26 and 1-37(b) results. Such diagrams were called "type-1 phase diagrams" by Pelton and Schmalzried (1973). If only potentials are held constant and one axis is a potential while the other is a composition variable, then the geometry exemplified by Figs. 1-8, 1-12, 1-34, 1-37(a), and the lower panel of Fig. 1-33 results. These were termed "type-2" diagrams. Finally, if only potentials are held constant and both axes are compositions, then a "type-3" diagram as in the upper panels of Figs. 1-32 and 1-33 results.

If the ϕ_i axis of a phase diagram is replaced by a composition variable that varies as its conjugate variable q_i (ex: q_i/q_j, $q_i/(q_i+q_j)$), then the new diagram and the original diagram are said to form a pair of *corresponding phase diagrams*. For instance, Figs. 1-37(a) and 1-37(b) are corresponding type-1 and type-2 phase diagrams, while Fig. 1-33 shows a corresponding pair of type-2 and type-3 diagrams. It is useful to draw corresponding diagrams beside each other as in Figs. 1-37 or 1-33 because the information contained in the two diagrams is complementary.

1.9.2.3 Theoretical Considerations

A complete rigorous proof that the procedure described in this section will always generate a true phase diagram is beyond the scope of this chapter. As an outline of the proof, we start with the generalized

stability criterion:

$$(\partial\phi_1/\partial q_1)_{\phi_2,\,\phi_3,\,\ldots,\,q_N,\,q_{N+1},\,q_{N+2},\,\ldots,\,q_{C+2}} \geq 0 \qquad (1\text{-}116)$$

This equation states that a potential ϕ_i always increases as its conjugate variable q_i increases when either ϕ_j or q_j from every other conjugate pair is held constant. For instance, μ_i of a component always increases as that component is added to a system (that is, as n_i is increased) at constant T and P, when either the number of moles or the chemical potential of every other component is held constant. In a binary system, for example, this means that the equilibrium Gibbs energy envelope is always convex, as shown in Fig. 1-6. If the envelope were concave, then the system would be unstable and would separate into two phases, as shown in Fig. 1-11.

Consider first a phase diagram with axes ϕ_1 and ϕ_2 with ϕ_3, ϕ_4, ..., ϕ_{C+1} and q_{C+2} constant. Such a diagram is always a true phase diagram. If the potential ϕ_1 is now replaced by q_1, the diagram still remains a true phase diagram because of Eq. (1-116). The sequence of equilibrium states that occurs as q_1 is increased will be the same as that which occurs as ϕ_1 is increased when all the other variables (ϕ_i or q_i) are held constant.

A true phase diagram is therefore obtained if the axis variables and constants are chosen from the variables ϕ_1, ϕ_2, ..., ϕ_N, q_{N+1}, q_{N+2}, ..., q_{C+1} with q_{C+2} held constant. The extensive variables can be normalized as (q_i/q_{C+2}) or by any other independent and unique set of ratios.

It should be noted that at least one extensive variable, q_{C+2}, is considered to be constant across the entire diagram. In practice, this means that one of the extensive variables must be either positive or negative everywhere on the diagram. For certain formal choices of components, extensive composition variables can have negative values. For example, in the predominance diagram of Fig. 1-1, if the components are chosen as $Cu-SO_2-O_2$, then the compound Cu_2S is written as $Cu_2(SO_2)O_{-2}$; that is $n_{O_2}=-1$. This is no problem in Fig. 1-1, since μ_{O_2} rather than n_{O_2} was chosen from the conjugate pair and is plotted as an axis variable. However, suppose we wish to plot a diagram of μ_{Cu} versus μ_{SO_2} at constant T and P in this system. In this case, the chosen variables would be T, P, μ_{SO_2}, n_{O_2}. Since one of the selected extensive variables must always be positive, and since n_{O_2} is the only selected extensive variable, it is necessary that n_{O_2} be positive everywhere. For instance, a phase field for Cu_2S is not permitted. In other words, only compositions in the $Cu-SO_2-O_2$ subsystem are permitted. A different phase diagram would result if we plotted μ_{Cu} versus μ_{SO_2} in the $Cu-SO_2-S_2$ subsystem with n_{S_2} always positive. Cu_2O would then not appear, for example. That is, at a given μ_{Cu} and p_{SO_2} we could have a low p_{O_2} and a high p_{S_2} in equilibrium with, for example, Cu_2S, or we could have a high p_{O_2} and a low p_{S_2} in equilibrium with, for example, Cu_2O. Hence the diagram will not be a true diagram unless compositions are limited to the $Cu-SO_2-O_2$ or $Cu-SO_2-S_2$ triangles. As a second example, if μ_{SiO} and μ_{CO} are chosen as variables in the SiO–CO–O system, then the diagram must be limited to $n_O>0$ (SiO–CO–O subsystem) or to $n_O<0$ (SiO–CO–Si–C subsystem).

1.9.2.4 Other Sets of Conjugate Pairs

The set of conjugate pairs in Table 1-1 is only one of many such sets. For example, if we make the substitution ($H=TS+\sum n_i\mu_i$) in Eq. (1-115), then we obtain another form of the general Gibbs–Duhem equation:

$$-H\,\mathrm{d}(1/T) - (V/T)\,\mathrm{d}P + \sum n_i\,\mathrm{d}(\mu_i/T) = 0 \qquad (1\text{-}117)$$

This defines another set of pairs of conjugate potentials and extensive variables: $(1/T, -H)$, $(P, -V/T)$, $(\mu_i/T, n_i)$. Choosing one and only one variable from each pair, we can construct a true phase diagram by the procedure described above. However, these diagrams may be of limited practical utility. This is discussed by Hillert (1997).

1.10 Solution Models

In Sec. 1.4.7, the thermodynamic expressions for simple ideal substitutional solutions were derived and in Secs. 1.5.7 and 1.6.2, the regular solution model and polynomial extensions thereof were discussed. For other types of solutions such as ionic mixtures, interstitial solutions, polymeric solutions, etc., the most convenient definition of ideality may be different. In the present section we examine some of these solutions. We also discuss structural ordering and its effect on the phase diagram. For further discussion, see Pelton (1997).

1.10.1 Sublattice Models

The sublattice concept has proved to be very useful in thermodynamic modeling. Sublattice models, which were first developed extensively for molten salt solutions, find application in ceramic, interstitial solutions, intermetallic solutions, etc.

1.10.1.1 All Sublattices Except One Occupied by Only One Species

In the simplest limiting case, only one sublattice is occupied by more than one species. For example, liquid and solid MgO–CaO solutions can be modeled by assuming an anionic sublattice occupied only by O^{2-} ions, while Mg^{2+} and Ca^{2+} ions mix on a cationic sublattice. In this case the model is formally the same as that of a simple substitutional solution, because the site fractions X_{Mg} and X_{Ca} of Mg^{2+} and Ca^{2+} cations on the cationic sublattice are numerically equal to the overall component mole fractions X_{MgO} and X_{CaO}. Solid and liquid MgO–CaO solutions have been shown (Wu et al., 1993) to be well represented by simple polynomial equations for g^E.

As a second example, the intermetallic ε-FeSb phase exhibits non-stoichiometry toward excess Fe. This phase was modeled (Pei et al., 1995) as a solution of Fe and stoichiometric FeSb by assuming two sublattices: an "Fe sublattice" occupied only by Fe atoms and an "Sb sublattice" occupied by both Fe and Sb atoms such that, per gram atom,

$$\Delta g_m = 0.5\,RT\,(y_{Fe} \ln y_{Fe} + y_{Sb} \ln y_{Sb}) + \alpha\, y_{Fe}\, y_{Sb} \qquad (1\text{-}118)$$

where $y_{Sb} = (1 - y_{Fe}) = 2X_{Sb}$ is the site fraction of Sb atoms on the "Sb sites" and α is an empirical polynomial in y_{Sb}.

1.10.1.2 Ionic Solutions

Let us take as an example a solution, solid or liquid, of NaF, KF, NaCl and KCl as introduced in Sec. 1.7.8. If the cations are assumed to mix randomly on a cationic sublattice while the anions mix randomly on an anionic sublattice, then the molar Gibbs energy of the solution can be modeled by the following equation which contains an ideal mixing term for each sublattice:

$$\begin{aligned} g = {} & (X_{Na} X_{Cl}\, g^0_{NaCl} + X_K X_F\, g^0_{KF} \\ & + X_{Na} X_F\, g^0_{NaF} + X_K X_{Cl}\, g^0_{KCl}) \\ & + RT\,(X_{Na} \ln X_{Na} + X_K \ln X_K) \\ & + RT\,(X_F \ln X_F + X_{Cl} \ln X_{Cl}) + g^E \end{aligned} \qquad (1\text{-}119)$$

where the factor $(X_{Na} X_{Cl})$, for example, is the probability, in a random mixture, of

finding a Na ion and a Cl ion as nearest neighbors. Differentiation of Eq. (1-119) gives the following expression for the activity of NaF:

$$RT \ln a_{NaF} = -X_K X_{Cl} \Delta G^{exchange} + RT \ln (X_{Na} X_F) + g^E_{NaF} \quad (1\text{-}120)$$

where $\Delta G^{exchange}$ is the Gibbs energy change for the following *exchange reaction* among the pure salts:

$$NaCl + KF = NaF + KCl; \quad (1\text{-}121)$$

$$\Delta G^{exchange} = g^0_{NaF} + g^0_{KCl} - g^0_{NaCl} - g^0_{KF}$$

In this example, $\Delta G^{exchange} < 0$. The salts NaF and KCl are thus said to form the *stable pair.* The first term on the right of Eq. (1-120) is positive. The members of the stable pair thus exhibit positive deviations, and in Fig. 1-31 this is reflected by the flat liquidus surfaces with widely spaced isotherms for NaF and KCl. That is, the mixing of pure NaF and KCl is unfavorable because it involves the formation of K^+-F^- and Na^+-Cl^- nearest-neighbor pairs at the expense of the energetically preferable Na^+-F^- and K^+-Cl^- pairs. If $\Delta G^{exchange}$ is sufficiently large, a miscibility gap will be formed, centered close to the *stable diagonal* joining the stable pair.

Blander (1964) proposed the following expression for g^E in Eq. (1-119):

$$g^E = X_{Na} g^E_{NaCl-NaF} + X_K g^E_{KCl-KF} + X_F g^E_{NaF-KF} + X_{Cl} g^E_{NaCl-KCl} - X_{Na} X_K X_F X_{Cl} (\Delta G^{exchange})^2 / ZRT \quad (1\text{-}122)$$

where, for example, $g^E_{NaCl-NaF}$ is the excess Gibbs energy in the NaCl–NaF binary system at the same cationic fraction X_{Na} as in the ternary, and where Z is the first coordination number. That is, g^E contains a contribution from each binary system. The final term in Eq. (1-122) is a first-order correction for non-random mixing which accounts for the fact that the number of Na^+-F^- and K^+-Cl^- nearest-neighbor pairs will be higher than the number of such pairs in a random mixture. This term is usually not negligible.

The phase diagram in Fig. 1-31(a) was calculated by means of Eqs. (1-119) and (1-122) solely from optimized excess Gibbs energies of the binary systems and from compiled data for the pure salts. Agreement with the measured diagram is very good.

Eqs. (1-119) and (1-122) can easily be modified for solutions in which the numbers of sites on the two sublattices are not equal, as in $MgCl_2-MgF_2-CaCl_2-CaF_2$ solutions. Also, in liquid salt solutions the ratio of the number of lattice sites on one sublattice to that on the other sublattice can vary with concentration, as in molten $NaCl-MgCl_2-NaF-MgF_2$ solutions. In this case, it has been proposed (Saboungi and Blander, 1975) that the molar ionic fractions in all but the random mixing terms of these equations should be replaced by equivalent ionic fractions. Finally, the equations can be extended to multicomponent solutions. These extensions are all discussed by Pelton (1988b).

For solutions such as liquid NaF–KF–NaCl–KCl for which $\Delta G^{exchange}$ is not too large, these equations are often sufficient. For solutions with larger exchange Gibbs energies, however, in which liquid immiscibility appears, these equations are generally unsatisfactory. It was recognized by Saboungi and Blander (1974) that this is due to the effect of non-randomness upon the second nearest-neighbor cation–cation and anion–anion interactions. To take account of this, Blander proposed additional terms in Eq.(1-122). Dessureault and Pelton (1991) modified Eqs. (1-119) and (1-122) to account more rigorously for non-random mixing effects, with good re-

sults for several molten salt systems with miscibility gaps. See also section 1.10.4.

1.10.1.3 Interstitial Solutions

As an example of the application of the sublattice model to interstitial solutions we will take the f.c.c. phase of the Fe–V–C system. Lee and Lee (1991) have modeled this solution using two sublattices: a metallic sublattice containing Fe and V atoms, and an interstitial lattice containing C atoms and vacancies, va. The numbers of sites on each sublattice are equal. An equation identical to Eq. (1-119) can be written for the molar Gibbs energy:

$$\begin{aligned} g = {} & (X_{Fe} X_{va} g^0_{Feva} + X_{Fe} X_C g^0_{FeC} \\ & + X_V X_{va} g^0_{Vva} + X_V X_C g^0_{VC}) \\ & + RT (X_{Fe} \ln X_{Fe} + X_V \ln X_V) \\ & + RT (X_C \ln X_C + X_{va} \ln X_{va}) + g^E \end{aligned} \qquad (1\text{-}123)$$

where $X_{Fe}=(1-X_V)$ and $X_C=(1-X_{va})$ are the site fractions on the two sublattices and "Feva" and "Vva" are simply pure Fe and V, i.e., $g^0_{Feva}=g^0_{Fe}$. An expression for g^E as in Eq. (1-122), although without the final non-random mixing term, was used by Lee and Lee with optimized binary g^E parameters. Their calculated Fe–V–C phase diagram is in good agreement with experimental data. The sublattice model has been similarly applied to many interstitial solutions by several authors.

1.10.1.4 Ceramic Solutions

Many ceramic solutions contain two or more cationic sublattices. As an example, consider a solution of Ti_2O_3 in $FeTiO_3$ (ilmenite) under reducing conditions. There are two cationic sublattices, the A and B sublattices. In $FeTiO_3$, Fe^{2+} ions and Ti^{4+} ions occupy the A and B sublattices, respectively. With additions of Ti_2O_3, Ti^{3+} ions occupy both sublattices. The solution can be represented as $(Fe^{2+}_{1-x}Ti^{3+}_x)_A$ $(Ti^{4+}_{1-x}Ti^{3+}_x)_B$ where x is the overall mole fraction of Ti_2O_3. The ions are assumed to mix randomly on each sublattice so that:

$$\Delta s^{ideal} = -2R[(1-x)\ln(1-x) + x \ln x] \qquad (1\text{-}124)$$

Deviations from ideal mixing are assumed to occur due to interlattice cation–cation interactions according to

$$\begin{aligned} & (Fe^{2+}_A - Ti^{4+}_B) + (Ti^{3+}_A - Ti^{3+}_B) \\ & = (Fe^{2+}_A - Ti^{3+}_B) + (Ti^{3+}_A - Ti^{4+}_B) \\ & \Delta G = a + bT \end{aligned} \qquad (1\text{-}125)$$

where a and b are the adjustable parameters of the model. The probability that an A–B pair is an $(Fe^{2+}_A - Ti^{3+}_B)$ or a $(Ti^{3+}_A - Ti^{4+}_B)$ pair is equal to $x(1-x)$. Hence, $g^E = x(1-x)(a+bT)$.

Similar models can be proposed for other ceramic solutions such as spinels, pseudobrookites, etc. These models can rapidly become very complex mathematically as the number of possible species on the lattices increases. For instance, in Fe_3O_4–Co_3O_4 spinel solutions, Fe^{2+}, Fe^{3+}, Co^{2+} and Co^{3+} ions are all distributed over both the tetrahedral and octahedral sublattices. Four independent equilibrium constants are required (Pelton et al., 1979) to describe the cation distribution even for the ideal mixing approximation. This complexity has been rendered much more tractable by the "compound energy model" (Sundman and Ågren, 1981; Hillert et al., 1988). This is not actually a model, but is rather a mathematical formalism permitting the formulation of various models in terms of the Gibbs energies, g^0, of "pseudocomponents" so that equations similar to Eq. (1-119) can be used directly.

1.10.1.5 The Compound Energy Formalism

As an example, the model for the $FeTiO_3$–Ti_2O_3 solution in Sec. 1.10.1.4 will be reformulated. By taking all combinations of an A-sublattice species and a B-sublattice species, we define two real components, $(Fe^{2+})_A(Ti^{4+})_BO_3$ and $(Ti^{3+})_A(Ti^{3+})_BO_3$, as well as two "pseudocomponents", $(Fe^{2+})_A(Ti^{3+})_BO_3^-$ and $(Ti^{3+})_A(Ti^{4+})_BO_3^+$.

Pseudocomponents, as in the present example, may be charged. Similarly to Eq. (1-119) the molar Gibbs energy can be written

$$g = (1-x)^2\, g^0_{FeTiO_3} + x^2\, g^0_{Ti_2O_3} + x(1-x)\, g^0_{FeTiO_3^-} + x(1-x)\, g^0_{Ti_2O_3^+} - T\Delta s^{ideal} \quad (1\text{-}126)$$

Note that charge neutrality is maintained in Eq. (1-126). The Gibbs energies of the two pseudocomponents are calculated from the equation

$$\Delta G = a + bT = g^0_{FeTiO_3^-} + g^0_{Ti_2O_3^+} - g^0_{FeTiO_3} - g^0_{Ti_2O_3} \quad (1\text{-}127)$$

where ΔG is the Gibbs energy change of Eq. (1-125) and is a parameter of the model. One of $g^0_{FeTiO_3^-}$ or $g^0_{Ti_2O_3^+}$ may be assigned an arbitrary value. The other is then given by Eq. (1-127). By substitution of Eq. (1-127) into Eq. (1-126) it may be shown that this formulation is identical to the regular solution formulation given in Sec. 1.10.1.4. Note that excess terms, g^E, could be added to Eq. (1-126), thereby giving more flexibility to the model. In the present example, however, this was not required.

The compound energy formalism is described and developed by Barry et al. (1992), who give many more examples. An advantage of formulating the sublattice model in terms of the compound energy formalism is that it is easily extended to multicomponent solutions. It also provides a conceptual framework for treating many different phases with different structures. This facilitates the development of computer software and databases because many different types of solutions can be treated as cases of one general formalism.

1.10.1.6 Non-Stoichiometric Compounds

Non-stoichiometric compounds are generally treated by a sublattice model. Consider such a compound $A_{1-\delta}B_{1+\delta}$. The sublattices normally occupied by A and B atoms will be called, respectively, the A-sublattice and the B-sublattice. Deviations from stoichiometry (where $\delta = 0$) can occur by the formation of defects such as B atoms on A sites, vacant sites, atoms occupying interstitial sites, etc. Generally, one type of defect will predominate for solutions with excess A and another type will predominate for solutions with excess B. These are called the majority defects.

Consider first a solution in which the majority defects are A atoms on B sites and B atoms on A sites: $(A_{1-x}B_x)_A(A_yB_{1-y})_B$. It follows that $\delta = (x-y)$. In the compound energy formalism we can write, for the molar Gibbs energy,

$$g = (1-x)(1-y)\, g^0_{AB} + (1-x)\, y\, g^0_{AA} + x(1-y)\, g^0_{BB} + xy\, g^0_{BA} + RT[x\ln x + (1-x)\ln(1-x) + y\ln y + (1-y)\ln(1-y)] \quad (1\text{-}128)$$

where g^0_{AB} is the molar Gibbs energy of (hypothetical) defect-free stoichiometric AB. Now the defect concentrations at equilibrium are those that minimize g. Therefore, setting $(\partial g/\partial x) = (\partial g/\partial y) = 0$ at constant δ, we obtain

$$\frac{xy}{(1-x)(1-y)} = \exp\left(-(1-x-y)\frac{\Delta g_1 + \Delta g_2}{RT}\right) \quad (1\text{-}129)$$

where $\Delta g_1 = (g^0_{AA} - g^0_{AB})$ and $\Delta g_2 = (g^0_{BB} - g^0_{AB})$ are the Gibbs energies of formation of the majority defects and where g^0_{BA} has been set equal to g^0_{AB}. At a given composition $\delta = (x-y)$, and for given values of the parameters Δg_1 and Δg_2, Eq. (1-129) can be solved to give x and y, which can then be substituted into Eq. (1-128) to give g. The more positive are Δg_1 and Δg_2, the more steeply g rises on either side of its minimum, and the narrower is the range of stoichiometry of the compound.

Consider another model in which the majority defects are vacancies on the B-sublattice and B atoms on interstitial sites. We now have three sublattices with occupancies $(A)_A(B_{1-y}va_y)_B(B_x va_{1-x})_I$ where "I" indicates the interstitial sublattice. The A-sublattice is occupied exclusively by A atoms. A vacancy is indicated by va. Stoichiometric defect-free AB is represented by (A)(B)(va) and $(x-y) = 2\delta/(1-\delta)$. Per mole of $A_{1-\delta}B_{1+\delta}$, the Gibbs energy is:

$$g = (1-\delta)\{[(1-x)(1-y)g^0_{ABva} + (1-x)y g^0_{Avava} + x(1-y)g^0_{ABB} + xy g^0_{AvaB} + RT[x\ln x + (1-x)\ln(1-x) + y\ln y + (1-y)\ln(1-y)]\} \quad (1\text{-}130)$$

Eq. (1-130) is identical to Eq. (1-128) apart from the factor $(1-\delta)$, and gives rise to an equilibrium constant as in Eq. (1-129). Other choices of majority defects result in very similar expressions. The model can easily be modified to account for other stoichiometries A_mB_n, for different numbers of available interstitial sites, etc., and its extension to multicomponent solutions is straightforward.

1.10.2 Polymer Solutions

For solutions of polymers in monomeric solvents, very large deviations from simple Raoultian ideal behaviour (i.e. from Eq. (1-40)) are observed. This large discrepancy can be attributed to the fact that the individual segments of the polymer molecule have considerable freedom of movement. Flory (1941, 1942) and Huggins (1942) proposed a model in which the polymer segments are distributed on the solvent sites. A large polymer molecule can thus be oriented (i.e. bent) in many ways, thereby greatly increasing the entropy. To a first approximation the model gives an ideal mixing term with mole fractions replaced by volume fractions in Eq. (1-45):

$$\Delta g_m^{ideal} = RT\left(X_A \ln \frac{X_A v^0_A}{X_A v^0_A + X_B v^0_B} + X_B \ln \frac{X_B v^0_B}{X_A v^0_A + X_B v^0_A}\right) \quad (1\text{-}131)$$

Lewis and Randall (1961) have compared the Flory–Huggins equation with experimental data in several solutions. In general, the measured activities lie between those predicted by Eq. (1-131) and by the Raoultian ideal equation, Eq. (1-45). A recent review of the thermodynamics of polymer solutions is given by Trusler (1999).

1.10.3 Calculation of Limiting Slopes of Phase Boundaries

From the measured limiting slope $(dT/dX)_{X_A=1}$ of the liquidus at the melting point of a pure component A, much information about the extent of solid solubility, as well as the structure of the liquid, can be inferred. Similar information can be obtained from the limiting slopes of phase boundaries at solid-state transformation points of pure components.

Eq. (1-65) relates the activities along the liquidus and the solidus to the Gibbs energy of fusion:

$$RT\ln a^l_A - RT\ln a^s_A = -\Delta g^0_{f(A)} \quad (1\text{-}132)$$

In the limit $X_A \rightarrow 1$, the liquidus and solidus converge at the melting point $T_{f(A)}$. Let us assume that, in the limit, Raoult's Law, Eq. (1-40), holds for both phases. That is, $a_A^l = X_A^l$ and $a_A^s = X_A^s$. Furthermore, from Eq. (1-60),

$$\Delta g^0_{f(A)} \rightarrow \Delta h_{f(A)} (1 - T/T_{f(A)})$$

Finally, we note that

$$\lim_{X_A \rightarrow 1} (\ln X_A) = \lim_{X_A \rightarrow 1} (\ln (1 - X_B)) = - X_B$$

Substituting these various limiting values into Eq. (1-132) yields:

$$\lim_{X_A \rightarrow 1} (dX_A^l/dT - dX_A^s/dT) = \Delta h^0_{f(A)}/R(T_{f(A)})^2 \qquad (1\text{-}133)$$

If the limiting slope of the liquidus, $\lim_{X_A \rightarrow 1} (dX_A^l/dT)$, is known, then the limiting slope of the solidus can be calculated, or vice versa, as long as the enthalpy of fusion is known.

For the LiF–NaF system in Fig. 1-18, the broken line is the limiting liquidus slope at $X_{LiF} = 1$ calculated from Eq. (1-133) under the assumption that there is no solid solubility (that is, that $dX_A^s/dT = 0$). Agreement with the measured limiting liquidus slope is very good, thereby showing that the solid solubility of NaF in LiF is not large.

In the general case, the solute B may dissolve to form more than one "particle". For example, in dilute solutions of Na_2SO_4 in $MgSO_4$, each mole of Na_2SO_4 yields two moles of Na^+ ions which mix randomly with the Mg^{2+} ions on the cationic sublattice. Hence, the real mole fraction of solvent, X_A, is $(1 - \nu X_B)$ where ν is the number of moles of foreign "particles" contributed by one mole of solute. In the present example, $\nu = 2$.

Eq. (1-133) now becomes:

$$\lim_{X_A \rightarrow 1} (dX_A^l/dT - dX_A^s/dT) = \Delta h^0_{f(A)}/\nu R(T_{f(A)})^2 \qquad (1\text{-}134)$$

The broken line in Fig. 1-44 is the limiting liquidus slope calculated from Eq. (1-134) under the assumption of negligible solid solubility.

It can be shown (Blander, 1964) that Eq. (1-134) applies very generally with the factor ν as defined above. For example, adding LiF to NaF introduces only one foreign

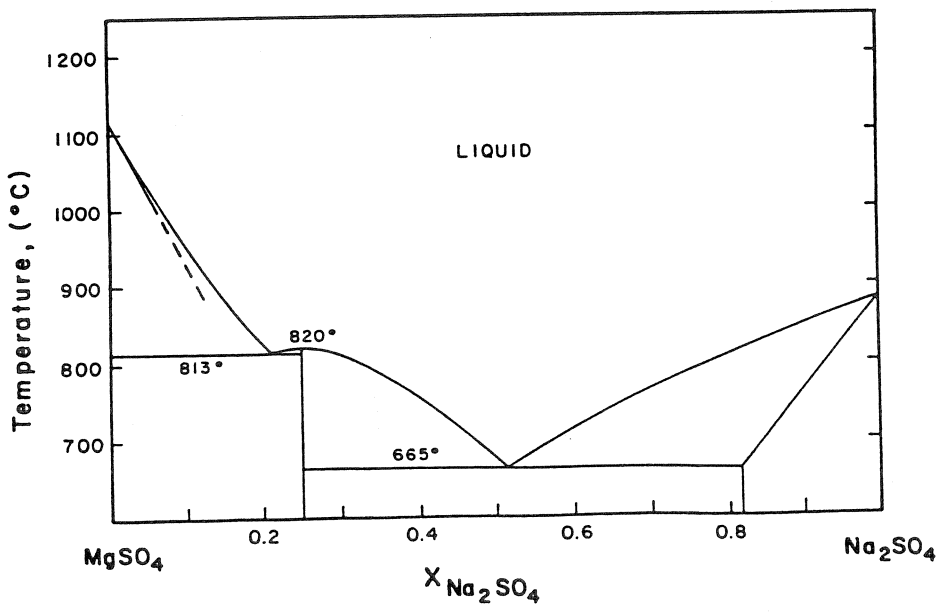

Figure 1-44. Phase diagram of the $MgSO_4$–Na_2SO_4 system calculated for an ideal ionic liquid solution. Broken line is the theoretical limiting liquidus slope calculated for negligible solid solubility taking into account the ionic nature of the liquid. Agreement with the measured diagram (Ginsberg, 1909) is good.

particle Li^+. The F^- ion is not "foreign". Hence, $\nu=1$. For additions of Na_2SO_4 to $MgSO_4$, $\nu=2$ since two moles of Na^+ ions are supplied per mole of Na_2SO_4. For $CaCl_2$ dissolved in water, $\nu=3$, and so on. For C dissolving interstitially in solid Fe, $\nu=1$. The fact that the solution is interstitial has no influence on the validity of Eq. (1-134). Eq. (1-134) is thus very general and very useful. It is independent of the solution model and of the excess properties, which become zero at infinite dilution.

An equation identical to Eq. (1-134) but with the enthalpy of transition, Δh^0_{tr}, replacing the enthalpy of fusion, relates the limiting phase boundary slopes at a transformation temperature of a component.

1.10.4 Short-Range Ordering

The basic premise of the regular solution model (Sec. 1.5.7) is that random mixing occurs even when g^E is not zero. To account for non-random mixing, the regular solution model has been extended though the *quasichemical model for short-range ordering* developed by Guggenheim (1935) and Fowler and Guggenheim (1939) and modified by Pelton and Blander (1984, 1986) and Blander and Pelton (1987). The model is outlined below. For a more complete development, see the last two papers cited above, Degterov and Pelton (1996), Pelton et al. (2000) and Pelton and Chartrand (2000).

For a binary system, consider the formation of two nearest-neighbor 1–2 pairs from a 1–1 and a 2–2 pair:

$$(1\text{–}1) + (2\text{–}2) = 2(1\text{–}2) \qquad (1\text{-}135)$$

Let the molar Gibbs energy change for this reaction be $(\omega - \eta T)$. Let the nearest-neighbor coordination numbers of 1 and 2 atoms or molecules be Z_1 and Z_2. The total number of bonds emanating from an i atom or molecule is $Z_i X_i$. Hence, mass balance equations can be written as

$$Z_1 X_1 = 2n_{11} + n_{12}$$
$$Z_2 X_2 = 2n_{22} + n_{12} \qquad (1\text{-}136)$$

where n_{ij} is the number of i–j bonds in one mole of solution. "Coordination equivalent fractions" may be defined as:

$$Y_1 = 1 - Y_2 = Z_1 X_1/(Z_1 X_1 + Z_2 X_2) \qquad (1\text{-}137)$$

where the total number of pairs in one mole of solution is $(Z_1 X_1 + Z_2 X_2)/2$. Letting X_{ij} be the fraction of i–j pairs in solution, Eq. (1-136) may be written as:

$$2Y_1 = 2X_{11} + X_{12}$$
$$2Y_2 = 2X_{22} + X_{12} \qquad (1\text{-}138)$$

The molar enthalpy and excess entropy of mixing are assumed to be directly related to the number of 1–2 pairs:

$$\Delta h_m - T s^{E(\text{non-config})} = (Z_1 X_1 + Z_2 X_2)\, X_{12}(\omega - \eta T)/4 \qquad (1\text{-}139)$$

An approximate expression for the configurational entropy of mixing is given by a one-dimensional Ising model:

$$\Delta s_m^{\text{config}} = -R(X_1 \ln X_1 + X_2 \ln X_2) - \frac{R}{2}(Z_1 X_1 + Z_2 X_2) \times [X_{11} \ln(X_{11}/Y_1^2) + X_{22} \ln(X_{22}/Y_2^2) + X_{12} \ln(X_{12}/2Y_1 Y_2)] \qquad (1\text{-}140)$$

The equilibrium distribution is calculated by minimizing Δg_m with respect to X_{12} at constant composition. This results in a "quasichemical" equilibrium constant for the reaction, Eq. (1-135):

$$\frac{X_{12}^2}{X_{11} X_{22}} = 4 \exp\left(\frac{-(\omega - \eta T)}{RT}\right) \qquad (1\text{-}141)$$

When $(\omega - \eta T) = 0$, the solution of Eqs. (1-138) and (1-141) gives a random distribu-

tion with $X_{11}=Y_1^2$, $X_{22}=Y_2^2$ and $2Y_1Y_2$, and Eq. (1-140) reduces to the ideal Raoultian entropy of mixing. When $(\omega-\eta T)$ becomes very negative, 1–2 pairs predominate. A plot of Δh_m or $s^{E(\text{non-config})}$ versus composition then becomes V-shaped and a plot of $\Delta s_m^{\text{config}}$ becomes m-shaped, with minima at $Y_1=Y_2=1/2$, which is the composition of maximum ordering, as illustrated in Fig. 1-45. When $(\omega-\eta T)$ is quite negative, the plot of g^E also has a negative V-shape.

For Fe–S liquid solutions, the activity coefficients of sulfur as measured by several authors are plotted in Fig. 1-46. It is clear in this case that the model should be applied with $Z_{Fe}=Z_S$. The curves shown in Fig. 1-46 were calculated from the quasichemical model with $(\omega-\eta T)$ expanded as

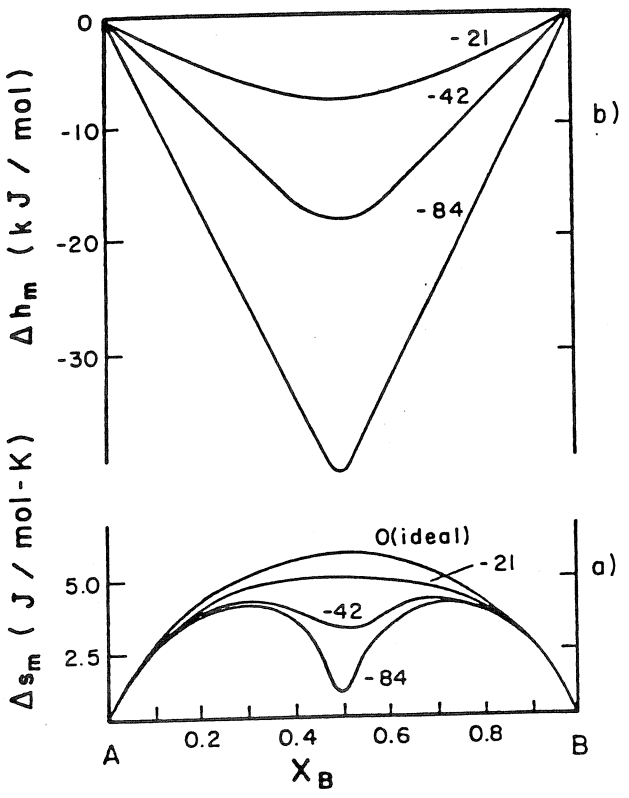

Figure 1-45. Molar enthalpy and entropy of mixing curves for a system AB calculated at 1000°C with $Z_1=Z_2=2$ from the quasichemical model for short-range ordering with $(\omega-\eta T)=0$, −21, −42, and −84 kJ.

the following optimized (Kongoli et al., 1998) polynomial:

$$(\omega-\eta T)=-(70017+9T)-74042\,Y_S-(798-15T)\,Y_S^3+40791\,Y_S^7 \quad \text{J/mol}^{-1} \tag{1-142}$$

Far fewer parameters are required than if a polynomial expansion of g^E (as in Sec. 1.6.2) were used. Furthermore, and more importantly, the model permits successful predictions of the properties of multicomponent systems as illustrated in Fig. 1-47, where measured sulfur activities in quaternary liquid Fe–Ni–Cu–S solutions are compared with activities calculated (Kongoli et al., 1998) solely from the optimized model parameters for the Fe–S, Ni–S and Cu–S binary systems. A pair exchange reaction like Eq. (1-135) was assumed for each M–S pair (M=Fe, Ni, Cu), and an optimized polynomial expansion of $(\omega_{MS}-\eta_{MS}T)$ as a function of Y_S, similar to Eq. (1-142), was obtained for each binary. Three equilibrium constant equations like Eq. (1-141) were written, and it was assumed that $(\omega_{MS}-\eta_{MS}T)$ in the quaternary system was constant at constant Y_S. No adjustable ternary or quaternary parameters were required to obtain the agreement shown in Fig. (1-47), although the model permits the inclusion of such terms if required.

Silicate slags are known to exhibit such short-range ordering. In the $CaO-SiO_2$ system, Δh_m has a strong negative V-shape, as in Fig. 1-45, but with the minimum at $X_{SiO_2}=1/3$ which is the composition corresponding to Ca_2SiO_4. That is, the ordering is associated with the formation of orthosilicate anions SiO_4^{4-}. In the phase diagram, Fig. 1-14, the CaO-liquidus can be seen to descend sharply near the composition $X_{SiO_2}=1/3$. The quasichemical model has been extended by Pelton and Blander (1984) to treat silicate slags. The diagram

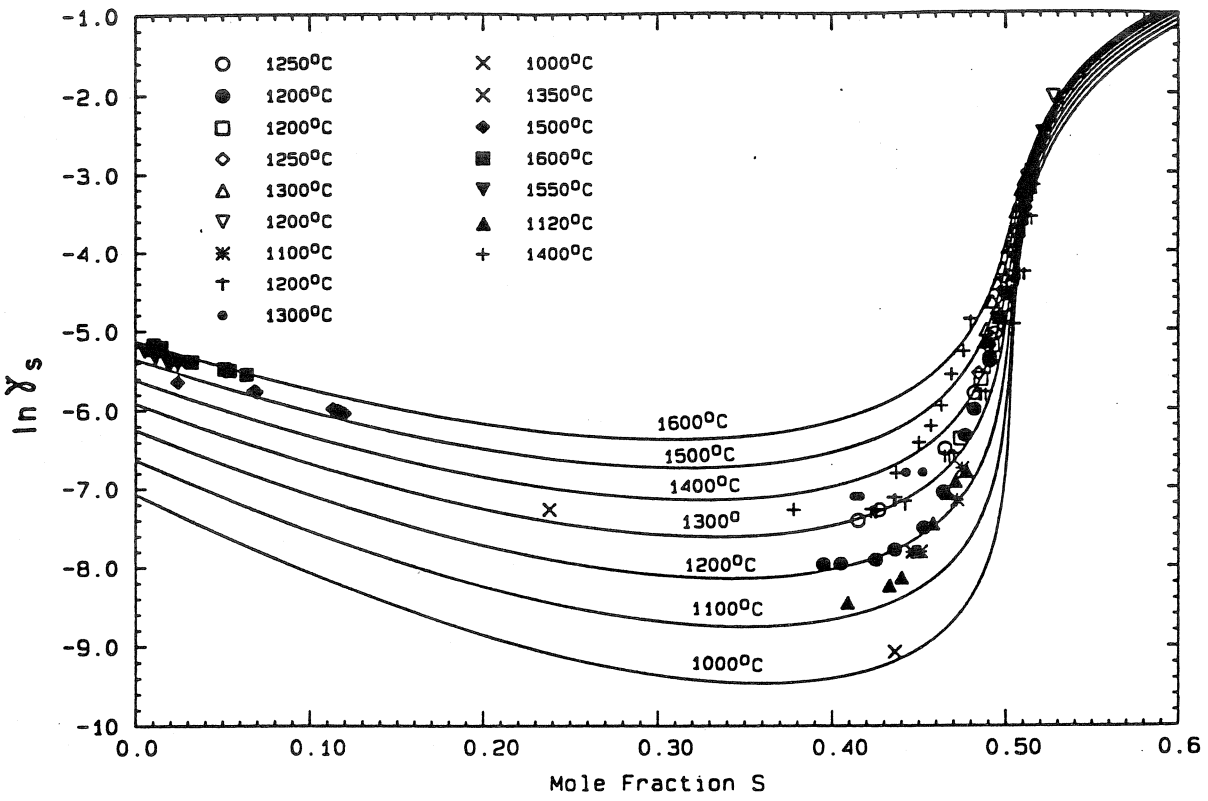

Figure 1-46. Activity coefficient of sulfur in liquid Fe–S solutions calculated from optimized quasichemical model parameters and comparison with experimental data (Kongoli et al., 1998).

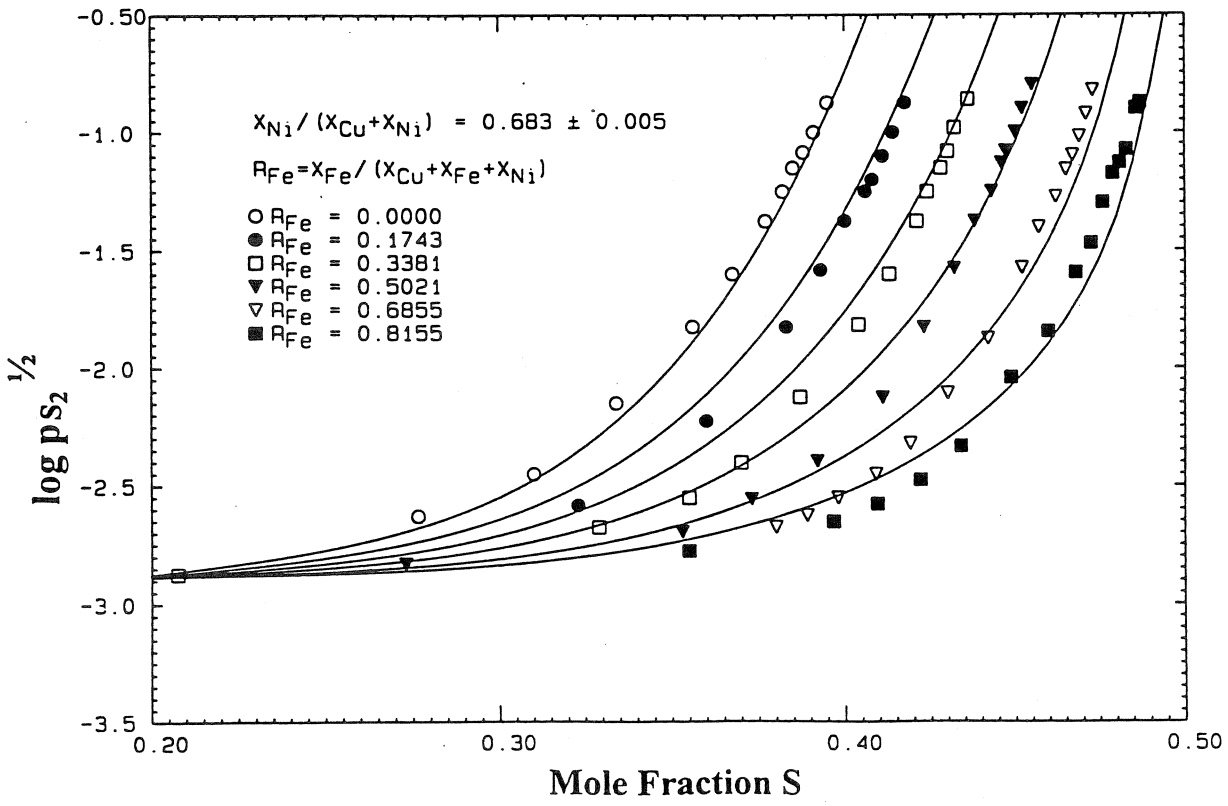

Figure 1-47. Equilibrium partial pressure of sulfur at 1200°C over Fe–Ni–Cu–S mattes predicted by the quasichemical model from binary data (Kongoli et al., 1998) and comparison with experimental data (Bale and Toguri, 1996).

shown in Fig. 1-14 is thermodynamically calculated (Wu, 1990).

Many liquid alloy solutions exhibit short-range ordering. The ordering is strongest when one component is relatively electropositive (on the left side of the periodic table) and the other is relatively electronegative. Liquid alloys such as Alk–Au (Hensel, 1979), Alk–Pb (Saboungi et al., 1985) and Alk–Bi (Petric et al., 1988a), where Alk = (Na, K, Rb, Cs), exhibit curves of Δh_m and Δs_m similar to those in Fig. 1-45 with one composition of maximum ordering. For example, in the Au–Cs system the minima occur near the composition AuCs; in Mg–Bi alloys the minima occur near the Mg_3Bi_2 composition, while in K–Pb alloys the maximum ordering is at K_4Pb.

It has also been observed that certain liquid alloys exhibit more than one composition of ordering. For example, in K–Te alloys, the "excess stability function", which is the second derivative of Δg_m, exhibits peaks near the compositions KTe_8, KTe and K_2Te (Petric et al., 1988b) thereby providing evidence of ordering centred on these compositions. The liquid might be considered as consisting of a series of mutually soluble "liquid intermetallic compounds".

When $(\omega - \eta T)$ is expanded as a polynomial as in Eq. (1-142), the quasichemical model and the polynomial model of Sec. 1.6.2 become identical as $(\omega - \eta T)$ approaches zero. That is, the polynomial model is a limiting case of the quasichemical model when the assumption of ideal configurational entropy is made.

When $(\omega - \eta T)$ is positive, (1–1) and (2–2) pairs predominate. The quasichemical model can thus also treat such clustering, which accompanies positive deviations from ideality.

Recent work (Pelton et al., 2000; Pelton and Chartrand, 2000) has rendered the model more flexible by permitting the Z_i to vary with composition and by expanding the $(\omega - \eta T)$ as polynomials in the bond fractions X_{ij} rather than the overall component fractions. A merger of the quasichemical and sublattice models has also been completed (Chartrand and Pelton, 2000), permitting nearest-neighbor and second-nearest neighbor short-range-ordering to be treated simultaneously in molten salt solutions.

1.10.5 Long-Range Ordering

In solid solutions, long-range ordering can occur as well as short-range ordering. In Fig. 1-15 for the Ag–Mg system, a transformation from an α' to an α phase is shown occurring at approximately 665 K at the composition Ag_3Mg. This is an *order–disorder* transformation. Below the transformation temperature, *long-range ordering* (superlattice formation) is observed. An *order parameter* may be defined which decreases to zero at the transformation temperature. This type of phase transformation is not a first-order transformation like those considered so far in this chapter. Unlike first-order transformations which involve a change of state (solid, liquid, gas) and also involve diffusion over distances large compared with atomic dimensions, order–disorder transformations, at least at the stoichiometric composition (Ag_3Mg in this example), occur by atomic rearrangement over distances of the order of atomic dimensions. The slope of the curve of Gibbs energy versus T is not discontinuous at the transformation temperature. Ordering and order–disorder transformations are discussed in Chapter 8 (Inden, 2001).

A type of order–disorder transformation of importance in ferrous metallurgy is the magnetic transformation. Below its *Curie temperature* of 769 °C, Fe is ferromagnetic.

Above this temperature it is not. The transformation involves a change in ordering of the atomic spins and is not first order. Additions of alloying elements will change the temperature of transformation. Magnetic transformations are treated in Chapter 4 (Binder, 2001). See also Miodownik (1982) and Inden (1982).

1.11 Calculation of Ternary Phase Diagrams From Binary Data

Among 70 metallic elements 70!/3!67! = 54 740 ternary systems and 916 895 quaternary systems are formed. In view of the amount of work involved in measuring even one isothermal section of a relatively simple ternary phase diagram, it is very important to have a means of estimating ternary and higher-order phase diagrams.

The most fruitful approach to such predictions is via thermodynamic methods. In recent years, great advances have been made in this area by the international Calphad group. Many key papers have been published in the *Calphad Journal*.

As a first step in the thermodynamic approach, we critically analyze the experimental phase diagrams and thermodynamic data for the three binary subsystems of the ternary system in order to obtain a set of mathematical expressions for the Gibbs energies of the binary phases, as was discussed in Sec. 1.6. Next, interpolation procedures based on solution models are used to estimate the Gibbs energies of the ternary phases from the Gibbs energies of the binary phases. Finally, the ternary phase diagram is calculated by computer from these estimated ternary Gibbs energies by means of common tangent plane or total Gibbs energy minimization algorithms.

As an example of such an estimation of a ternary phase diagram, the experimental

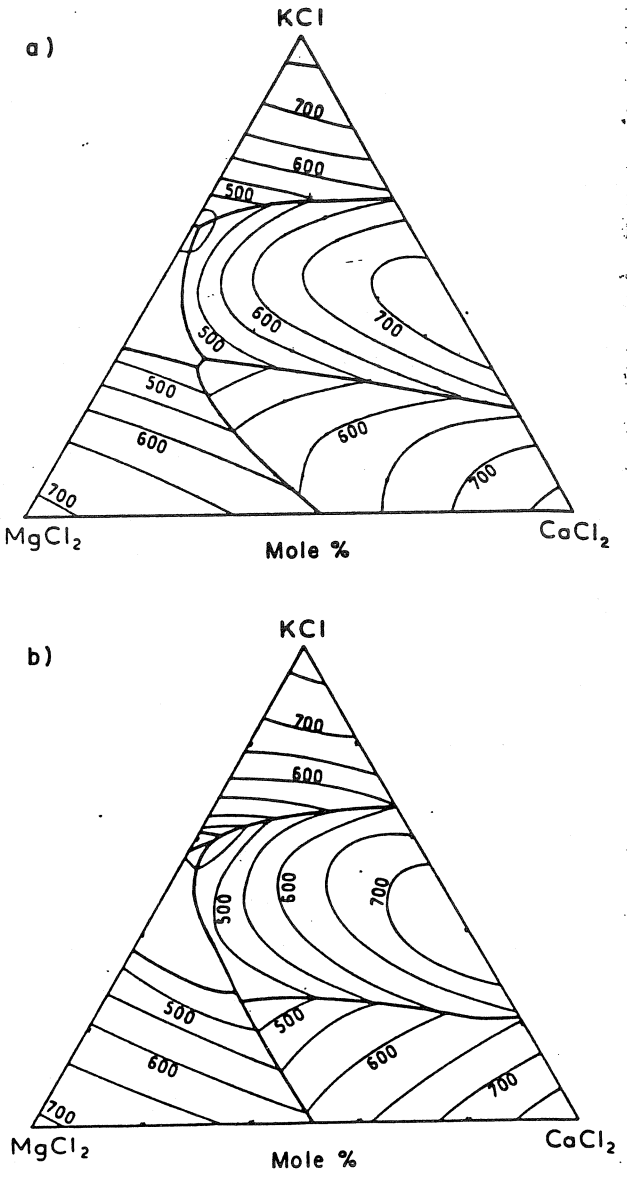

Figure 1-48. Projection of the liquidus surface of the $KCl-MgCl_2-CaCl_2$ system.
a) Calculated from optimized binary thermodynamic parameters (Lin et al., 1979).
b) As reported by Ivanov (1953).

(Ivanov, 1953) and estimated (Lin et al., 1979) liquidus projections of the $KCl-MgCl_2-CaCl_2$ system are shown in Fig. 1-48. The estimated phase diagram was calculated from the thermodynamic properties of the three binary subsystems with the Gibbs energy of the ternary liquid approximated via the equation suggested by

Kohler (1960):

$$g^E = (1 - X_A)^2 g^E_{B/C} + (1 - X_B)^2 g^E_{C/A} + (1 - X_C)^2 g^E_{A/B} \quad (1\text{-}143)$$

In this equation, g^E is the excess molar Gibbs energy at a composition point in the ternary liquid phase and $g^E_{B/C}$, $g^E_{C/A}$ and $g^E_{A/B}$ are the excess Gibbs energies in the three binary systems at the same ratios X_B/X_C, X_C/X_A and X_A/X_B as at the ternary point. If the ternary liquid phase as well as the three binary liquid phases are all regular solutions, then Eq. (1-143) is exact. In the general case, a physical interpretation of Eq. (1-143) is that the contribution to g^E from, say, pair interactions between A and B particles is constant at a constant ratio X_A/X_B apart from the dilutive effect of the C particles, which is accounted for by the term $(1-X_C)^2$ taken from regular solution theory.

Ternary phase diagrams estimated in this way are quite acceptable for many purposes. The agreement between the experimental and calculated diagrams can be greatly improved by the inclusion of one or two "ternary terms" with adjustable coefficients in the interpolation equations for g^E. For example, the ternary term $aX_{KCl}X_{MgCl_2}X_{CaCl_2}$, which is zero in all three binaries, could be added to Eq. (1-143) and the value of the parameter a which gives the "best" fit to the measured ternary liquidus could be determined. This, of course, requires that ternary measurements be made, but only a very few (even one or two in this example) experimental liquidus points will usually suffice rather than the larger number of measurements required for a fully experimental determination. In this way, the coupling of the thermodynamic approach with a few well chosen experimental measurements holds promise of greatly reducing the experimental effort involved in determining multicomponent phase diagrams.

Reviews of various interpolation procedures and computer techniques for estimating and calculating ternary and higher-order phase diagrams are given by Ansara (1979), Spencer and Barin (1979) and Pelton (1997).

Other equations, similar to the Kohler Eq. (1-143) in that they are based on extension of regular solution theory, are used to estimate the thermodynamic properties of ternary solutions from the properties of the binary subsystems. For a discussion and references, see Hillert (1980). However, for structurally more complex solutions involving more than one sublattice or with significant structural ordering, other estimation techniques must be used. For a review, see Pelton (1997).

An example, the calculation of the phase diagram of the NaCl–KCl–NaF–KF system in Fig. 1-31, has already been presented in Sec. 1.10.1.2.

The quasichemical model for systems with short-range ordering was discussed for the case of binary systems in Sec. 1.10.4. The model has been extended to permit the estimation of ternary and multicomponent phase diagrams (Pelton and Blander, 1986; Blander and Pelton, 1987; Pelton and Chartrand, 2000). Very good results have been obtained in the case of silicate systems. The liquidus surface of the SiO_2–MgO–MnO system, estimated from optimized binary data with the quasichemical model for the liquid and under the assumption of ideal mixing for the solid $MgSiO_3$–$MnSiO_3$ and Mg_2SiO_4–Mn_2SiO_4 solutions, is shown in Fig. 1-49. Agreement with the measured phase diagram (Glasser and Osborn, 1960) is within experimental error limits.

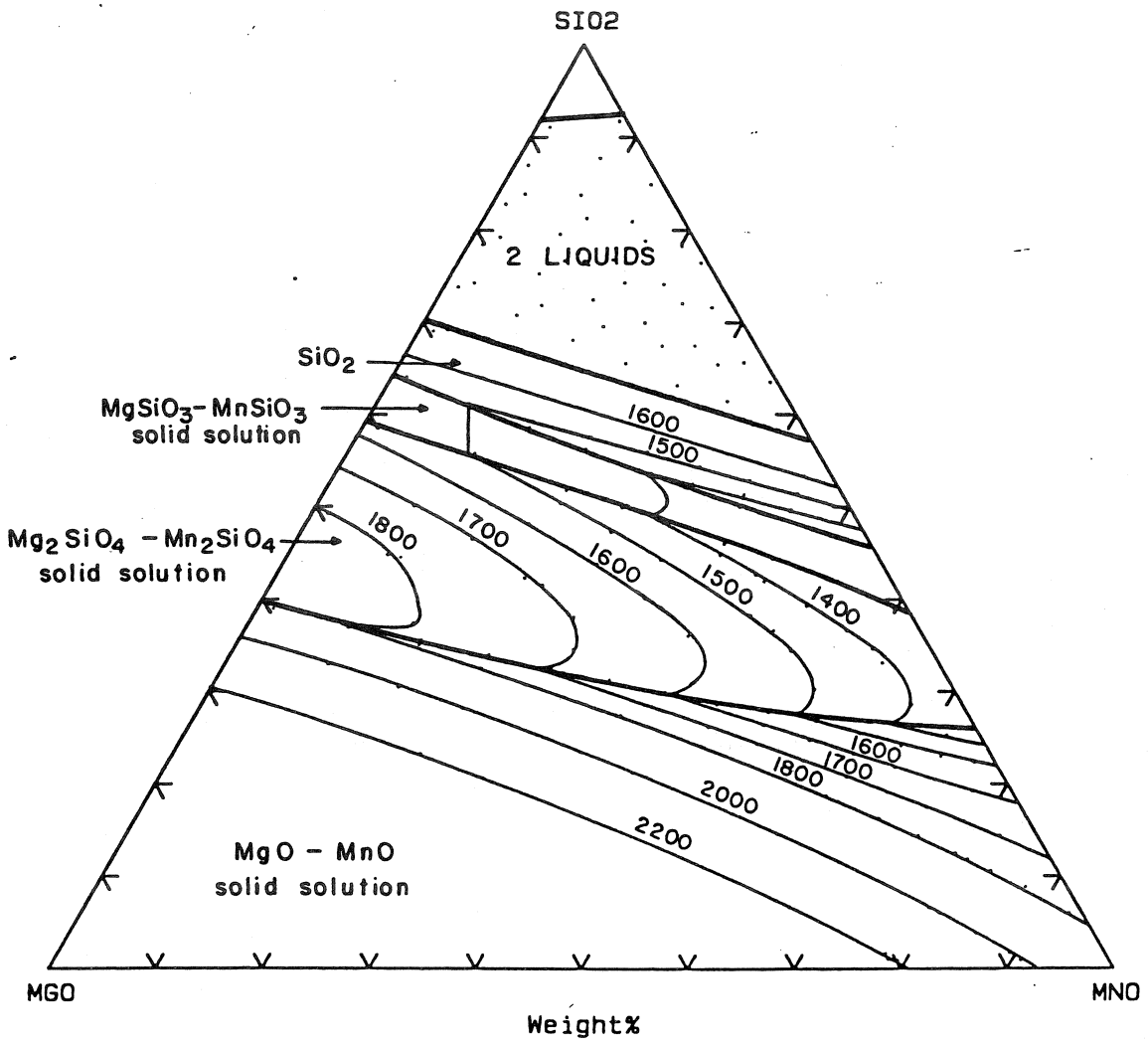

Figure 1-49. Projection of liquidus surface of the SiO_2–MgO–MnO system calculated from optimized binary parameters with the quasichemical model for the liquid phase.

1.12 Minimization of Gibbs Energy

Throughout this chapter it has been shown that phase equilibria are calculated by Gibbs energy minimization. Computer software has been developed in recent years to perform such calculations in systems of any number of components, phases and species.

Consider a system in which several stoichiometric solid or liquid compounds A, B, C, ... could be present at equilibrium along with a number of gaseous, liquid or solid solution phases α, β, γ, ... The total Gibbs energy of the system may be written as:

$$G = (n_A g_A^0 + n_B g_B^0 + \ldots) + (n_\alpha g_\alpha + n_\beta g_\beta + \ldots) \qquad (1\text{-}144)$$

where n_A, n_B, etc. are the number of moles of the pure solid or liquidus; g_A^0, g_B^0, etc. are the molar Gibbs energies of the pure solids or liquids (which are functions of T and P); n_α, n_β, etc. are the total number of moles of the solution phases; g_α, g_β, etc. are the molar Gibbs energies of the solution phases (which are function of T, P and composition). For a given set of constraints

(such as fixed T, P and overall composition), the free energy minimization algorithms find the set of mole numbers n_A, n_B, etc., n_α, n_β, etc. (some may be zero) as well as the compositions of all solution phases which globally minimize G. This is the equilibrium phase assemblage. Other constraints such as constant volume or a fixed chemical potential (such as constant p_{O_2}) may be applied.

A discussion of the strategies of such algorithms is beyond the scope of the present chapter. One of the best known general Gibbs energy minimization programs is Solgasmix written by Eriksson (1975) and constantly updated.

When coupled to a large thermodynamic database, general Gibbs energy minimization programs provide a powerful tool for the calculation of phase equilibria. Several such expert database systems have been developed. They have been reviewed by Bale and Eriksson (1990).

An example of a calculation performed by the F * A * C * T (Facility for the Analysis of Chemical Thermodynamics) expert system, which the author has helped to develop, is shown in Table 1-2. The program has been asked to calculate the equilibrium state when 1 mol of SiI_4 is held at 1400 K in a volume of 10^4 l. The thermodynamic properties of the possible product species have been automatically retrieved from the database and the total Gibbs energy has been minimized by the Solgasmix algorithm. At equilibrium there will be 2.9254 mol of gas of the composition shown and 0.11182 mol of solid Si will precipitate. The total pressure will be 0.0336 bar.

Although the calculation was performed by minimization of the total Gibbs energy, substitution of the results into the equilibrium constants of Eqs. (1-10) to (1-12) will show that these equilibrium constants are satisfied.

Another example is shown in Table 1-3 (Pelton et al., 1990). Here the program has been asked to calculate the equilibrium

Table 1-2. Calculation of equilibrium state when 1 mole SiI_4 is held at 1400 K in a volume of 10^4 l. Calculations performed by minimization of the total Gibbs energy.

SiI_4 =		
2.9254	(0.67156	I
	+0.28415	SiI_2
	+0.24835E-01	I_2
	+0.19446E-01	SiI_4
	+0.59083E-05	SiI
	+0.23039E-07	Si
	+0.15226E-10	Si_2
	+0.21462EE-11	Si_3)
	(1400.0,0.336E-01,G)	
	+0.11182	Si
	(1400.0,0.336E-01,S1, 1.0000)	

Table 1-3. Calculation of equilibrium state when reactants shown (masses in g) are held at 1873 K at a pressure of 1 atm. Calculations performed by minimization of the total Gibbs energy.

100. Fe+0.08 O+0.4 Fe+0.4 Mn+0.3 Si+0.08 Ar=		
0.30793 litre	(99.943	vol% Ar
	+0.24987E-01	vol% Mn
	+0.24069E-01	vol% SiO
	+0.82057E-02	vol% Fe
	+0.79044E-07	vol% O
	+0.60192E-08	vol% Si
	+0.11200E-08	vol% O_2
	+0.35385E-15	vol% Si_2)
	(1873.0, 1.00	,G)
+ 0.18501 gram	(49.948	wt.% SiO_2
	+42.104	wt.% MnO
	+7.9478	wt.% FeO)
	(1873.0, 1.00	,SOLN 2)
+ 100.99 gram	(99.400	wt.% Fe
	+ 0.33630	wt.% Mu
	+ 0.25426	wt.% Si
	+ 0.98375E-02	wt.% O_2)
	(1873.0, 1.00	,SOLN 3)

state when 100 g Fe, 0.08 g oxygen, 0.4 g Fe, 0.4 g Mn, 0.3 g Si and 0.08 g Ar are brought together at 1873 K at a total pressure of 1 bar. The database contains data for a large number of solution phases as well as for pure compounds. These data have been automatically retrieved and the total Gibbs energy has been minimized. At equilibrium there are 0.30793 l of a gas phase, 0.18501 g of a molten slag, and 100.99 g of a molten steel of the compositions shown.

The Gibbs energies of the solution phases are represented as functions of composition by various solution models (Sec. 1.10). As discussed in Sec. 1.11, these models can be used to predict the thermodynamic properties of *N*-component solutions from evaluated parameters for binary (and possibly ternary) subsystems stored in the database. For example, in the calculation in Table 1-3, the Gibbs energy of the molten slag phase was estimated by the quasichemical model from optimized parameters for the binary oxide solutions.

1.12.1 Phase Diagram Calculation

Gibbs energy minimization is used to calculate general phase diagram sections thermodynamically using the zero phase fraction line concept (Sec. 1.9.1.1), with data retrieved from databases of model coefficients. For example, to calculate the diagram of Fig. 1-30, the program first scans the four edges of the diagram to find the ends of the ZPF lines. Each line is then followed from beginning to end, using Gibbs energy minimization to determine the point at which a phase is just on the verge of being present. When ZPF lines for all phases have been drawn, then the diagram is complete. Because, as shown in Sec. 1.9, all true phase diagram sections obey the same geometrical rules, one algorithm suffices to calculate all types of phase diagrams with any properly chosen variables as axes or constants.

1.13 Bibliography

1.13.1 Phase Diagram Compilations

The classic compilation in the field of binary alloy phase diagrams is that of Hansen (1958). This work was continued by Elliott (1965) and Shunk (1969). These compilations contain critical commentaries. A non-critical compilation of binary alloy phase diagrams is supplied in looseleaf form with a continual up-dating service by W.G. Moffatt of the General Electric Co., Schenectady, N.Y. An extensive non-critical compilation of binary and ternary phase diagrams of metallic systems has been edited by Ageev (1959–1978). An index to all compilations of binary alloy phase diagrams up to 1979 was prepared by Moffatt (1979). A critical compilation of binary phase diagrams involving Fe has been published by Kubaschewski (1982). Ternary alloy phase diagrams were compiled by Ageev (1959–1978).

From 1979 to the early 1990s, the American Society for Metals undertook a project to evaluate critically all binary and ternary alloy phase diagrams. All available literature on phase equilibria, crystal structures, and often thermodynamic properties were critically evaluated in detail by international experts. Many evaluations have appeared in the *Journal of Phase Equilibria* (formerly *Bulletin of Alloy Phase Diagrams*), (ASM Int'l., Materials Park, OH), which continues to publish phase diagram evaluations. Condensed critical evaluations of 4700 binary alloy phase diagrams have been published in three volumes (Massalski et al., 1990). The ternary phase

diagrams of 7380 alloy systems have also been published in a 10-volume compilation (Villars et al., 1995). Both binary and ternary compilations are available from ASM on CD-ROM. Many of the evaluations have also been published by ASM as monographs on phase diagrams involving a particular metal as a component.

Each year, MSI Services (http://www.msiwp.com) publishes *The Red Book*, which contains abstracts on alloy phase diagrams from all sources, notably from the extensive Russian literature. MSI also provides a CD-ROM with extensive alloy phase diagram compilations and reports.

Phase diagrams for over 9000 binary, ternary and multicomponent ceramic systems (including oxides, halides, carbonates, sulfates, etc.) have been compiled in the 12-volume series, *Phase Diagrams for Ceramists* (1964–96, Am. Ceramic Soc., Columbus, OH). Earlier volumes were non-critical compilations. However, recent volumes have included critical commentaries.

Phase diagrams of anhydrous salt systems have been compiled by Voskresenskaya (1970) and Robertson (1966).

An extensive bibliography of binary and multicomponent phase diagrams of all types of systems (metallic, ceramic, aqueous, organic, etc.) has been compiled by Wisniak (1981).

1.13.2 Thermodynamic Compilations

Several extensive compilations of thermodynamic data of pure substances of interest in materials science are available. These include the JANAF Tables (Chase et al., 1985) and the compilations of Barin et al. (1977), Barin (1989), Robie et al. (1978) and Mills (1974), as well as the series of compilations of the National Institute of Standards and Technology (Washington, D.C.).

Compilations of properties of solutions (activities, enthalpies of mixing, etc.) are much more difficult to find. Hultgren et al. (1973) present the properties of a number of binary alloy solutions. An extensive bibliography of solution properties of all types of solutions was prepared by Wisniak and Tamir (1978).

Thermodynamic/phase diagram optimization as discussed in Sec. 1.6.1 has been carried out for a large number of alloy, ceramic and other systems. Many of these evaluations have been published in the international *Calphad Journal*, published since 1977 by Pergamon Press. Several of the evaluations in the *Journal of Phase Equilibria* discussed above include thermodynamic/phase diagram optimizations, as do a number of the evaluations in Vol. 7 of *Phase Diagrams for Ceramists.*

Extensive computer databases of the thermodynamic properties of compounds and solutions (stored as coefficients of model equations) are available. These include F*A*C*T (http://www.crct.polymtl.ca), Thermocalc (http://www.met.kth.se), ChemSage (http://gttserv.lth.rwth-aachen.de), MTS-NPL (http://www.npl.co.uk), Thermodata (http://www.grenet.fr), HSC (http://www.outokumpu.fi), and MALT2 (http://www. kagaku.com). Gibbs energy minimization software permits the calculation of complex equilibria from the stored data as discussed in Sec. 1.12 as well as the thermodynamic calculation of phase diagram sections. A listing of these and other available databases is maintained at http://www.crct. polymtl.ca .

A bibliographic database known as Thermdoc, on thermodynamic properties and phase diagrams of systems of interest to materials scientists, with updates, is available through Thermodata (http://www.grenet.fr).

1.13.3 General Reading

The theory, measurement and applications of phase diagrams are discussed in a great many texts. Only a few can be listed here. A recent text by Hillert (1998) provides a complete thermodynamic treatment of phase equilibria as well as solution modeling and thermodynamic/phase diagram optimization.

A classical discussion of phase diagrams in metallurgy was given by Rhines (1956). Prince (1966) presents a detailed treatment of the geometry of multicomponent phase diagrams. A series of five volumes edited by Alper (1970–1978) discusses many aspects of phase diagrams in materials science. Bergeron and Risbud (1984) give an introduction of phase diagrams, with particular attention to applications in ceramic systems, see also Findlay (1951), Ricci (1964) and West (1965).

In the *Calphad Journal* and in the *Journal of Phase Equilibria* are to be found many articles on the relationships between thermodynamics and phase diagrams.

It has been beyond the scope of the present chapter to discuss experimental techniques of measuring thermodynamic properties and phase diagrams. For the measurement of thermodynamic properties, including properties of solutions, the reader is referred to Kubaschewski and Alcock (1979). For techniques of measuring phase diagrams, see Pelton (1996), Raynor (1970), MacChesney and Rosenberg (1970), Buckley (1970) and Hume-Rothery et al. (1952).

1.14 References

Ageev, N. V. (Ed.) (1959–1978), *Phase Diagrams of Metallic Systems*, Vols. 1–22. Moscow: Acad. Sci. USSR.

Alabyshev, A. F., Morachevskii, A. G. (1957), *Z. Neorg. Khim. 2*, 669.

Alper, A. M. (Ed.) (1970–1978), *Phase Diagrams – Materials Science and Technology*, Vols. 1–5. New York: Academic.

Ansara, I. (1979), *Internat. Met. Rev. 238*, No. 1, 20.

Bale, C. W. (1990), *Canad. Metall. Quart. 29*, 263.

Bale, C. W., Eriksson, N. G. (1990), *Canad. Metall. Quart. 29*, 105.

Bale, C. W., Pelton, A. D. (1983), *Metall. Trans. B14*, 77.

Bale, C. W., Toguri, J. (1996), private communication.

Bale, C. W., Pelton, A. D., Thompson W. T. (1986), *Canad. Metall. Quart. 25*, 107.

Barin, I. (1989), *Thermochemical Data of Pure Substances*. 2. Weinheim: VCH Verlagsgesellschaft.

Barin, I., Knacke, O., Kubaschewski, O. (1977), *Thermochemical Properties of Inorganic Substances*. Berlin: Springer Verlag.

Barry, T. I., Dinsdale, A. T., Gisby, J. A., Hallstedt, B., Hillert, M., Jansson, B., Jonsson, J., Sundman, B., Taylor, J. R. (1992), *J. Phase Equilib. 13*, 459.

Bartlett, H. E. Neethling, A. J., Crowther, P. (1970), *J. Chem. Thermo. 2*, 523.

Bergeron, C. J., Risbud, S. H. (1984), *Introduction to Phase Equilibria in Ceramics*. Columbus, Ohio: Amer. Ceramic Soc.

Binder, K. (2001), in: *Phase Transformations in Materials:* Kostorz, G. (Ed.). Weinheim: Wiley-VCH, Chap. 4.

Binder, K., Fratzl, P. (2001), in: *Phase Transformations in Materials:* Kostorz, G. (Ed.). Weinheim: Wiley-VCH, Chap. 6.

Blander, M. (1964), *Molten Salt Chemistry*. New York: Interscience, Chap. 3.

Blander, M., Pelton, A. D. (1987), *Geochim. et Cosmochim. Acta 51*, 85.

Bray, H. F., Bell, F. D., Harris, S. J. (1961–1962), *J. Inst. Metals 90*, 24.

Buckley, R. A. (1970), in: *Techniques of Metals Research*, Vol. IV, Part 1: Rapp, R. A. (Ed.). New York: Interscience.

Chartrand, P., Pelton, A. D. (2000), *Metall. Mater. Trans.*, in press.

Chase, M. W. (1983), *Bull. Alloy Phase Diag. 4*, 124.

Chase, M. W., Davies, C. A., Downey, J. R., Frurip, D. J., McDonald, R. A., Syverud, A. N. (1985), *JANAF Thermochemical Tables*, 3rd ed. New York: Amer. Inst. Physics.

Chu, W. F., Rahmel, A. (1979), *Rev. High-Temp. Mater. IV*, 139.

Degterov, S., Pelton, A. D. (1996), *J. Phase Equilib. 17*, 488.

Dessureault, Y., Pelton, A. D. (1991), *J. Chim. Phys. 88*, 1811.

Dessureault, Y., Sangster, J., Pelton, A. D. (1990), *J. Electrochem. Soc. 137*, 2941.

Doman, R. C., Barr, J. B., McNally, R. N., Alper, A. M. (1963), *J. Am. Ceram. Soc. 46*, 313.

Dörner, P., Henig, E.-Th., Krieg, H., Lucas, H. L., Petzow, G. (1980), *Calphad Journal 4*, 241.

Elliott, R. P. (1965), *Constitution of Binary Alloys.* First Supplement. New York: McGraw-Hill.
Eriksson, N. G. (1975), *Chemical Scripta 8*, 100.
Findlay, A. (1951), *The Phase Rule*, 9th edn., revised by Campbell, A. N., Smith, N. A. New York: Dover.
Flory, P. J. (1941), *J. Chem. Phys. 9*, 660.
Flory, P. J. (1942), *J. Chem. Phys. 10*, 5.
Fowler, R. H., Guggenheim, E. A. (1939), *Statistical Thermodynamics.* Cambridge: Cambridge Univ. Press, p. 350.
Garrels, R. M., Christ, C. L. (1965), *Solutions Minerals and Equilibria.* New York: Harper and Row.
Ginsberg, A. S. (1909), *Z. Anorg. Chem. 61*, 130.
Glasser, E. P., Osborn, E. F. (1960), *J. Amer. Ceram. Soc. 43*, 136.
Guggenheim, E. A. (1935), *Proc. Roy. Soc. A148*, 304.
Gulbransen, E. A., Jansson, S. A. (1970), *Proc. Symp. Electrochem. Soc. Fall meeting 1969.* New York: The Electrochem. Soc., p. 3.
Gupta, H., Morral, J. E., Nowotny, H. (1986), *Scripta Metall.* 20, 889.
Hansen, M. (1958), *Constitution of Binary Alloys*, 2nd edn. New York: McGraw-Hill.
Harshe, G., Venkatachalam, S. (1984), *J. Metals 36*, 34.
Hauffe, K. (1940), *Z. Elektrochem. 46*, 348.
Hensel, F. (1979), *Adv. Phys. 28*, 555.
Hillert, M. (1980), *Calphad Journal 4*, 1.
Hillert, M. (1985), *Int. Metall. Rev. 30*, 45.
Hillert, M. (1997), *J. Phase Equilib. 18*, 249.
Hillert, M. (1998), *Phase Equilibria, Phase Diagrams and Phase Transformations.* Cambridge: Cambridge University Press.
Hillert, M., Jansson, B., Sundman, B. (1988), *Z. Metallk. 79*, 81.
Holm, J. L. (1965), *Acta Chem. Scand. 19*, 638.
Hong, K. C., Kleppa, O. J. (1976), *J. Chem. Thermodyn. 8*, 31.
Huggins, M. L. (1942), *Ann. N. Y. Acad. Sci. 43*, 1.
Hultgren, R., Desai, P. D., Hawkins, D. T., Gleiser, M., Kelly, K. K., Wagman, D. D. (1973), *Selected Values of the Thermodynamic Properties of the Elements and Binary Alloys.* Metals Park, Ohio: Am. Soc. of Metals.
Hume-Rothery, W., Christian, J. W., Pearson, W. B. (1952), *Metallurgical Equilibrium Diagrams.* London: Inst. Phys.
Inden, G. (1982), *Bull. Alloy Phase Diag. 2*, 412.
Inden, G. (2001), in: *Phase Transformations in Materials:* G. Kostorz (Ed.). Weinheim: Wiley-VCH, Chap. 8.
Ingraham, T. R., Kellogg, H. H. (1963), *TMS-AIME 227*, 1419.
Ingraham, T. R., Kerby, R. (1967), *Canad. Metall. Quart. 6*, 89.
Ivanov, A. I. (1953), *Izv. Sekt. Fiz.-Khim. Anal. Inst. Obshchei Neorg. Khim. Akad. Nauk SSSR 23*, 197.
Katsura, T., Muan, A. (1964), *TMS-AIME 230*, 77.
Kellogg, H. H., Basu, S. K. (1960), *TMS-AIME 218*, 70.
Kleinstuber, T. (1961), Ph.D. Thesis, Univ. Munich, Germany.
Kohler, F. (1960), *Monatsh. Chemie 91*, 738.
Köster, W., Dullenkopf, W. (1936), *Z. Metallk. 28*, 309.
Kongoli, F., Dessureault, Y., Pelton, A. D. (1998), *Metall. and Mat. Trans. 29B*, 591.
Kubaschewski, O. (1982), *Iron-Binary Phase Diagrams.* New York: Springer Verlag.
Kubaschewski, O., Alcock, C. B., (1979), *Metallurgical Thermochemistry*, 5th ed. New York: Pergamon Press.
Kurnakow, N. S., Kusnetzow, A. N. (1907), *Z. Anorg. Chem. 52*, 173.
Kunz, M. (2001), in: *Phase Transformations in Materials:* G. Kostorz (Ed.). Weinheim: Wiley-VCH, Chap. 10.
Lantratov, M. F., Mikhailova, A. G. (1971), *Zh. Prikl. Khimii 44*, 1778.
Lee, B.-J., Lee, D. N. (1991), *Calphad 15*, 293.
Lee, B. J., Lee, D. N. (1992), *J. Phase Equilib. 13*, 349.
Levin, E. M., Robbins, C. R., McMurdie, H. F. (1964), and 11 supplements to (1996), *Phase Diagrams for Ceramists;* Columbus, Ohio: Am. Ceramic Soc.
Lewis, G. N., Randall, M. (1961), *Thermodynamics*, revised by Pitzer, K. S., Brewer, L. New York: McGraw-Hill.
Lin, P.-L., Pelton, A. D., Bale, C. W. (1979), *J. Am. Ceram. Soc. 62*, 414.
Lipson, H., Wilson, A. J. C. (1940), *J. Iron Steel Inst. 142*, 122.
Lukas, H. L., Henig, E.-Th., Zimmermann, B. (1977), *Calphad Journal 1*, 225.
MacChesney, J. B., Rosenberg, P. E. (1970), in *Phase Diagrams – Materials Science and Technology*, Vol. 1: Alper, A. M. (Ed.). New York: Academic, Ch. 3.
Maiorova, E. A., Morachevskii, A. G., Kovalenko, S. G. (1976), *Elektrokhimiya 12*, 313.
Massalski, T. B., Okamoto, H., Subramanian, P. R., Kacprzak, L. (1990), *Binary Alloy Phase Diagrams*, 2nd ed. Metals Park, OH: Am. Soc. Metals.
Mathewson, C. H. (1906), *Z. Ang. Chem. 50*, 180.
Mills, K. C. (1974), *Thermodynamic Data for Inorganic Sulphides, Selenides and Tellurides.* London: Butterworths.
Miodownik, A. P. (1982), *Bull. Alloy Phase Diag. 2*, 406.
Moffatt, W. B. (1979), *The Index to Binary Phase Collections*, Schenectady. N.Y.: General Electric Corp.
Muan, A., and Osborn, F. (1965), *Phase Equilibria Among Oxides in Steelmaking.* Reading, MA.: Addison Wesley.
Müller-Krumbhaar, H., Kurz, W., Brener, E. (2001), in: *Phase Transformations in Materials:* G. Kostorz (Ed.). Weinheim: Wiley-VCH, Chap. 2.

Palatnik, L. S., Landau, A. I. (1964), *Phase Equilibria in Multicomponent Systems*. NY: Holt, Rinehart and Winston.
Pehlke, R. D. (1973), *Unit Processes of Extractive Metallurgy*. New York: Elsevier.
Pei, B., Björkman, B., Sundman, B., Jansson, B. (1995), *Calphad 19*, 1.
Pelton, A. D. (1983), in: *Physical Metallurgy:* Cahn, R. W., Haasen, P. (Eds.). Amsterdam: Elsevier, Chap. 7.
Pelton, A. D. (1988a), *Bull. Alloy Phase Diag. 9*, 41.
Pelton, A. D. (1988b), *Calphad Journal 12*, 127.
Pelton, A. D. (1995), *J. Phase Equilib. 16*, 501.
Pelton, A. D. (1996), in: *Physical Metallurgy*: Cahn, R. W., Haasen, P. (Eds.). Amsterdam, North-Holland, Chap. 6.
Pelton, A. D. (1997), in: *Advanced Physical Chemistry for Process Metallurgy*: Sano, N., Lu, W.-K, Riboud P. (Eds.). New York, Academic, Chap. 3.
Pelton, A. D., Bale, C. W. (1986), *Metall. Trans. A 17*, 1057.
Pelton, A. D., Blander, M. (1984), *Proc. AIME Symp. on Molten Salts and Slags*. Warrendale, Pa.: The Metall. Soc. AIME, p. 281.
Pelton, A. D., Blander, M. (1986), *Metall. Trans. B 17*, 805.
Pelton, A. D., Chartrand, P. (2000), *Metall. Mater. Trans.*, in press.
Pelton, A. D., Degterov, S. A., Eriksson, G., Robelin, C., Dessureault, Y. (2000), *Metall. Mater. Trans., B 31*, 651.
Pelton, A. D., Schmalzried, H. (1973), *Metall. Trans. 4*, 1395.
Pelton, A. D., Schmalzried, H., Sticher, J. (1979), *J. Phys. Chem. Solids 40*, 1103.
Pelton, A. D., Thompson, W. T. (1975), *Prog. Solid State Chem. 10*, part 3, 119.
Pelton, A. D., Thompson, W. T., Bale, C. W., Erikson, N. G. (1990), *High Temp. Sci. 26*, 231.
Petric, A., Pelton, A. D., Saboungi, M.-L. (1988a), *J. Electrochem. Soc. 135*, 2754.
Petric, A., Pelton, A. D., Saboungi, M.-L. (1988b), *J. Chem. Phys. 85*, 5070.
Phillips, B., Muan, A. (1958), *J. Am. Ceram. Soc. 41*, 448.
Pilgrim, R. F., Ingraham, T. R. (1967), *Canad. Metall. Quart. 6*, 333.
Polyakov, V. D. (1940), *Izv. Sektora Fiz.-Khim Analiza Inst. Obshchei Neorg. Khim. Akad. Nauk SSSR 13*, 308.
Prince, A. (1963), *Metall. Rev. 8*, 213.
Prince, A. (1966), *Alloy Phase Equilibria*. Amsterdam: Elsevier.
Raynor, G. V. (1970), in: *Physical Metallurgy*, 2nd edn: Cahn, R. W. (Ed.). Amsterdam: North Holland, Chap. 7.
Rhines, F. N. (1956), *Phase Diagrams in Metallurgy*. New York: McGraw-Hill.
Ricci, J. E. (1964), in: *Molten Salt Chemistry:* Blander, M. (Ed.). New York: Interscience, Chap. 4.
Robertson, W. D. (Ed.) (1966), *Binary Phase Diagrams of Halide Salts*, U. S. At. En. Comm. Contract AT (30-1) 2723, Washington: Clearinghouse for Federal Scientific and Techn. Info.
Robie, R. A., Hemingway, B. S., Fisher, J. R. (1978), *Thermodynamic Properties of Minerals and Related Substances at 298.15 K and 1 Bar Pressure and at Higher Temperatures*. Washington: U.S. Government Printing Office.
Roos, G. D. (1916), *Z. Anorg. Chem. 94*, 329.
Saboungi, M.-L., Blander, M. (1974), *High Temp. Sci. 6, 37*.
Saboungi, M.-L., Blander, M. (1975), *J. Am. Ceram. Soc. 58*, 1.
Saboungi, M.-L., Herron, S. J., Kumar, R. (1985), *Ber. Bunsenges. Phys. Chem. 89*, 375.
Sangster, J., Pelton, A. D. (1987), *J. Phys. Chem. Ref. Data 16*, 509.
Schenk, H., Frohberg, M. G., Nunninghof, R. (1964), *Arch. Eisenhütten 35*, 269.
Schreinemakers, F. A. H. (1915), *Proc. K. Akad. Wetenschappen, Amsterdam (Section of Sciences) 18*, 116.
Shatynski, S. R. (1977), *Oxidn. Metals 11*, 307.
Shunk, F. A. (1969), *Constitution of Binary Alloys*. Second Supplement. New York: McGraw-Hill.
Spencer, P. J., Barin, I. (1979), *Mater. Eng. Appl. 1*, 167.
Stringer, J., Whittle, D. P. (1977), *Rev. Int. Htes. Temp. Réfract. 14*, 6.
Sundman, B., Ågren, J. (1981), *J. Phys. Chem. Solids 42*, 297.
Trusler, J. P. M. (1999), in: *Chemical Thermodynamics:* Letcher, T. (Ed.). Abingdon, Oxon, UK: Blackwell Science, Chap. 16.
Van Laar, J. J. (1908), *Z. Phys. Chem. 63*, 216; *64*, 257.
Villars, P., Prince, A., Okamoto, H. (1995), *Handbook of Ternary Alloy Phase Diagrams*. Metals Park, OH: Am. Soc. Metals.
Voskresenskaya, N. K. (Ed.) (1970), *Handbook of Solid-Liquid Equilibria in Systems of Anhydrous Inorganic Salts*, Vol. 1, TT69-55079/1, AEC-tr-69831/3, UC-4, Washington: U.S. At. En. Comm. and Nat'l. Sci. Foundation.
Weeks, J. R. Davies, H. A. (1964), AEC Report, Conf. 660712-1, BNL-10372.
West, D. R. F. (1965), *Ternary Equilibrium Diagrams*. New York: McMillan.
Wisniak, J. (1981), *Phase Diagrams: A Literature Source Book*, Vols. 1 and 2. New York: Elsevier.
Wisniak, J., Tamir, A. (1978), *Mixing and Excess Thermodynamic Properties: A Literature Source Book*. New York: Elsevier.
Wu, P. (1990), Ph. D. thesis, Ecole Polytechnique, Montreal.
Wu, P., Eriksson, G., Pelton, A. D. (1993), *J. Am. Ceram. Soc. 76*, 2065.
Yokokowa, H. (1999), *J. Phase Equilib. 20*, 258.